University of California
Santa Barbara

An Exploration in Optomechanics: from Trampoline Resonators to Multimode Mechanics

A dissertation submitted in partial satisfaction
of the requirements for the degree

Doctor of Philosophy
in
Physics

by

Matthew James Weaver

Committee in charge:

Professor Dirk Bouwmeester, Chair
Professor Ania Jayich
Professor Mark Srednicki

June 2018

The Dissertation of Matthew James Weaver is approved.

Professor Ania Jayich

Professor Mark Srednicki

Professor Dirk Bouwmeester, Committee Chair

June 2018

An Exploration in Optomechanics: from Trampoline Resonators to Multimode Mechanics

by

Matthew James Weaver

Acknowledgements

Working on my dissertation has been an exciting, challenging, and ultimately rewarding experience thanks in a large part to the people I worked with and spent time with along the way. I had many adventures with friends in Santa Barbara and travelling which helped me get through difficult times in grad school. Thank you to my family for being there for me throughout the process.

I would like to thank my adviser, Dirk Bouwmeester, for steadily pushing me along the way and providing a stimulating project and work environment. I would like to especially thank Fernando for always being there to discuss ideas and Brian for teaching me clean room fabrication techniques. Frank, Hedwig and Sven were invaluable teammates across the ocean who kept me motivated with their insights and results. Wolfgang, Kier and Harmen have all given me incredibly helpful advice and I was excited to work with Vitaly, Sameer and Yasmine, who I am confident will continue excellent work in optomechanics. I enjoyed working with David Newsom and John Terry, and many interesting and helpful discussions with my group members Eric, John and Joe. I would also like to thank the members of the quantum optics group in Leiden for taking me in for my long visits to the Netherlands and showing me around.

Curriculum Vitæ

Matthew James Weaver

Education

June 2018	Ph.D. in Physics (Expected), University of California, Santa Barbara.
May 2015	M.A. in Physics, University of California, Santa Barbara.
June 2012	B.S. in Physics, Massachusetts Institute of Technology

Experience

2012 - 2018	Graduate Student Researcher, Department of Physics, UCSB: Bouwmeester Group
	Graduate Teaching Assistant, Department of Physics, UCSB
2010 - 2012	Undergraduate Researcher, Research Laboratory for Electronics, MIT: Ram Group
2009	Undergraduate Researcher, Kavli Insititute for Astrophysics and Space Research, MIT: Advisor: John Belcher

Publications

M. J. Weaver, D. Newsom, F. Luna, W. Löffler, and D. Bouwmeester, Phonon Interferometry for Measuring Quantum Decoherence, *Physical Review A* (in print)

S. Sonar, V. Fedoseev, **M. Weaver**, F. Luna, E. Vlieg, H. van der Meer, D. Bouwmeester, and W. Löffler, Strong Thermo-mechanical Squeezing in a far detuned Membrane-in-the-middle System, *arXiv:1805.09897*

M. J. Weaver, F. M. Buters, F. Luna, H. J. Eerkens, K. Heeck, S. de Man and D. Bouwmeester, Coherent Optomechanical State Transfer between Disparate Mechanical Resonators, *Nature Communications*, Vol 8, 824, 2017

F. M. Buters, F. Luna, **M. J. Weaver**, H. J. Eerkens, K. Heeck, S. de Man, and D. Bouwmeester, Straightforward method to measure optomechanically induced transparency, *Optics Express*, Vol 25, Issue 11, 2017

F. M. Buters, K. Heeck, H. J. Eerkens, **M. J. Weaver**, F. Luna, S. de Man, and D. Bouwmeester, High Q nested resonator in an actively

stabilized optomechanical cavity, *Applied Physics Letters*, Vol 110, March 2017

F. M. Buters, **M. J. Weaver**, H. J. Eerkens, K. Heeck, S. de Man, and D. Bouwmeester, Optomechanics with a polarization nondegenerate cavity, *Physical Review A*, Vol 94, December 2016

M. J. Weaver, B. Pepper, F. Luna, F. M. Buters, H. J. Eerkens, G. Welker, B. Perock, K. Heeck, S. de Man and D. Bouwmeester, Nested trampoline resonators for optomechanics, *Applied Physics Letters*, Vol 108, January, 2016 [Cover photo]

F. M. Buters, H. J. Eerkens, K. Heeck, **M. J. Weaver**, B. Pepper, S. de Man, and D. Bouwmeester, Experimental exploration of the optomechanical attractor diagram and its dynamics, *Physical Review A*, Vol 92, July 2015

H. J. Eerkens, F. M. Buters, **M. J. Weaver**, B. Pepper, G. Welker, K. Heeck, P. Sonin, S. de Man, and D. Bouwmeester, Optical sideband cooling of a low frequency optomechanical system, *Optics Express*, Vol 23, Issue 6, 2015

J. S. Orcutt, B. Moss, C. Sun, J. Leu, M.Georgas, J. Shainline, E. Zgraggen, H.Li, J. Sun, **M. Weaver**, S. Urošević, M. Popović, R. J. Ram, and V.Stojanović, Open foundry platform for high-performance electronic-photonic integration, *Optics Express*, Vol 20, Issue 11, 2012

Abstract

An Exploration in Optomechanics: from Trampoline Resonators to Multimode Mechanics

by

Matthew James Weaver

The quantum to classical transition in large mechanical systems is still a mystery. An ideal tool for exploring this new regime of physics is cavity optomechanics. The field of optomechanics uses light in an optical cavity to finely control and detect mechanical motion. Remarkable progress has been made in recent years with the generation of non-classical states of motion. If such states can be extended into the macroscopic regime, new physics may emerge due to the unprecedented scale.

In this dissertation we work towards the goal of macroscopic quantum optomechanics by developing new mechanical devices, experimental techniques and experimental protocols. First we fabricate nested trampoline resonators, devices with high mechanical quality factor, excellent vibrational isolation from the mechanical environment and mirrors which can support high finesse cavities. With these devices we explore a new optomechanical interaction in which spatially separated, nondegenerate mechanical modes can exchange their state. Finally, we investigate theoretically how this interaction can generate a quantum entangled state between multiple mechanical modes, bypassing many experimental difficulties of previously proposed schemes. These developments help pave the way towards phonon interference experiments in macroscopic resonators.

Contents

List of Figures

List of Tables

Chapter 1

Introduction

In 1935 Schrödinger proposed his famous thought experiment in which a cat is placed into a quantum superposition state of alive and dead inside a box [1]. Since then, experiments have verified the counterintuitive behavior of quantum systems repeatedly in systems ranging from photons [2, 3] and atoms [4, 5] to large molecules like buckminsterfullerene [6]. Nevertheless, nothing remotely resembling the scale of a cat has been observed in a quantum superposition state. It is therefore natural to try and understand the limitations of quantum mechanics and to discover if there is some fundamental limit to the mass or size of a system with quantum behaviors.

In 2010, the first solid state mechanical system was cooled to its ground state and controlled at the single quantum level [7]. Since then a plethora of mechanical systems interacting with electromagnetic fields have been explored [8]. These systems hold the promise of extending the precise control demonstrated with photons, atoms and molecules to macroscopic systems. Ultimately, we will hopefully be able to answer the question of what happens to an object which you can see and touch when it is in a superposition state of two different locations.

We attempt to investigate this question by performing tests of quantum mechanics

on systems which can be seen by eye and are at the limits of current quantum technologies. In Chapter 2 we discuss some of the novel decoherence effects which we might observe and we review the capabilities of optomechanical devices. In the short term, we develop an optomechanical system and experimental techniques to help address some of these questions.

We need high quality optomechanical devices to perform these experiments. In Chapter 3 we develop micromirrors integrated onto mechanical oscillators which can support cavities with extremely slow optical loss rate. This is necessary both for a strong interaction and to avoid loss of quantum information. We then construct a “box" for our mechanical “cat", which isolates it from the outside mechanical vibrations in Chapter 4. In Chapter 5 we study the mechanical losses in our resonators which could cause unwanted decoherence. The trampoline resonators we develop have sufficient optical and mechanical quality for optical cooling and interesting experiments in the quantum regime.

Experiments to test decoherence in the quantum regime could be improved with the use of multiple mechanical resonators. In Chapter 6 we demonstrate a method to transfer excitations between two different types of trampoline resonators. This coupling could be used to transfer quantum states or produce entanglement between two mechanical resonators. We develop a scheme for generating an entangled superposition state between two mechanical resonators in Chapter 7 which makes use of this capability. In Chapter 8 we discuss some preliminary results on moving towards the quantum regime. Both the devices we fabricated and the techniques we have investigated could form the basis for future tests of quantum mechanics in macroscopic objects.

This research was performed as part of a collaboration between a research group at UC Santa Barbara and a research group at Leiden University. In Santa Barbara, we fabricated and characterized the trampoline resonators used in these studies. In Leiden,

we executed more complicated optics experiments including: optical cooling, optomechanically induced transparency and state swapping between resonators as well as experiments at cryogenic temperatures. The highly collaborative nature of the team led to 9 publications, some of which are included in this work.

Chapter 2

Macroscopic Optomechanics and Decoherence

We do not see quantum behavior of the macroscopic objects which surround us in everyday life. This most likely means that some sort of decoherence prevents large scale quantum objects from exhibiting quantum effects. In this chapter we will discuss a number of proposed decoherence mechanisms which might impact massive objects. Optomechanical systems are an ideal testbed for such effects, and we will discuss two cavity optomechanical geometries which could be useful for studying the quantum mechanics of large objects. Finally, we will briefly discuss the ways in which optomechanics can be used to generate superposition states and probe decoherence.

2.1 Novel Decoherence Mechanisms

There are many counterintuitive features of quantum theory, including the fact that an object can be in a superposition state in which it effectively occupies multiple locations at once. The breakdown of such interesting states can be described by decoher-

ence of the system. There are a number of theories which have had success in explaining the decoherence of systems interacting with a thermal environment [9]. However, the subject is quite complex, and we still do not have a complete picture of the quantum to classical transition, particularly in macroscopic systems. In this section we will describe a number of theoretical ideas for decoherence mechanisms which could affect this transition.

Environmentally induced decoherence is a model for decoherence in which a system couples to a bath of many harmonic oscillators in equilibrium at a certain temperature. The oscillator we are studying gradually becomes entangled with the oscillators of the bath. However, we only directly observe our oscillator, so if we perform a measurement on the oscillator this corresponds to tracing out all the other oscillators [9, 10]. The net result is an apparent decoherence of the oscillator with a timescale given by [11]:

$$\tau_{EID} \approx \frac{\hbar^2}{D\Delta x^2} \tag{2.1.1}$$

$D = 2m\gamma k_B T$ is the diffusion term which depends on the damping rate, γ, the mass, m and the temperature T. Δx is the spatial separation of the superposition state of the oscillator. While this mechanism is expected to dominate for many of the current mechanical resonators which have been brought into spatial superposition states, it has never been directly measured and characterized.

There are several other decoherence channels predicted by standard quantum theory. The oscillator can decohere in a similar fashion from interactions with two level systems in the environment [12, 13, 14]. Decoherence from interactions with gas molecules in the vacuum has been theoretically modeled [15, 16, 17] and experimentally observed with matter wave interferometry [18], but not yet with solid mechanical resonators. Finally localization from blackbody radiation is possible, but it would likely be very slow at

cryogenic temperatures [11]. An experiment which could distinguish these decoherence mechanisms in a macroscopic object would already be important and interesting.

If these conventional decoherence processes are sufficiently slow, it might be possible to observe more exotic forms of decoherence. One of these forms is gravitationally induced decoherence, a theoretical possibility suggested by Diósi [19] and Penrose [20]. These proposals posit that because of one of the fundamental incompatibilities between quantum mechanics and general relativity massive quantum systems must decohere according to their gravitational self-energy [21]:

$$\tau_{GID} \approx \frac{\hbar}{\Delta E_G} \tag{2.1.2}$$

$$\Delta E_G = 4\pi G \int\int \frac{\left(\rho_1(\vec{x}) - \rho_2(\vec{x})\right)\left(\rho_1(\vec{y}) - \rho_2(\vec{y})\right)}{\left|\vec{x} - \vec{y}\right|} d^3x d^3y \tag{2.1.3}$$

ΔE_G is the gravitational self-energy calculated using the spatial mass distribution ρ in each of the two components of the superposition. There is considerable theoretical debate about which mass distribution to use. However, the decoherence scales up with mass, and for some distributions the decoherence could be faster than conventional decoherence mechanisms [21].

Gravitationally induced decoherence is just one example of a more generalized class of spontaneous collapse models [22]. One such framework is known as continuous spontaneous localization [23, 24]. In this framework the Schrödinger Equation is modified to include a localization length and extra terms with unknown prefactors [22]. Other spontaneous collapse models include the GRW model [25, 26], the QMUPL model [19, 27] and quantum gravity effects [28, 29, 30]. For many of these mechanisms smaller mass systems with large position uncertainties are expected to be the most likely to exhibit anomalously fast decoherence [31, 22]. However, for some models a massive system in a superposition state might be able to discern the novel decoherence [21]. There is a great deal of theoretical uncertainty about the parameters for spontaneous local-

ization models, so experiments with massive systems could probe interesting regions of parameter space. It is therefore important for fundamental physics to develop quantum manipulation and observation tools for massive systems.

2.2 Cavity Optomechanics

Optomechanical systems enable the precise readout and control of mechanical motion, all the way down to the quantum level [8, 32]. In an optomechanical system an electromagnetic field inside a cavity interacts with the mechanical motion of a resonator, in our case through the radiation pressure force. A number of key milestones have already been reached on the road to macroscopic superposition states: near ground state cooling [7, 33, 34, 35, 36], exchange of a single quantum between electromagnetic and mechanical resonators [7, 37], and projection into single phonon Fock states [38, 39]. We will examine how these tools can play a part in studies with large mass devices.

Optomechanical systems can be described by the Hamiltonian [40, 8]:

$$H = \hbar\omega_c(x)a^\dagger a + \hbar\omega_m b^\dagger b \tag{2.2.1}$$

$$= \hbar\omega_c a^\dagger a + \hbar\omega_m b^\dagger b + \hbar g_0 a^\dagger a\left(b^\dagger + b\right) + \hbar g_2 a^\dagger a\left(b^\dagger + b\right)^2 + \ldots \tag{2.2.2}$$

ω_c and ω_m are the frequencies of the optical cavity and the mechanical resonator. The second line comes from a Taylor Expansion of $\omega_c(x)$. a and b are the lowering operators for the optical cavity and the mechanical resonator. g_0 is the single photon optomechanical coupling rate, often modified to be $g = g_0 a^\dagger a = g_0\sqrt{n_c}$. g_2 is the second order single photon optomechanical coupling rate, which for most of this dissertation is either zero or negligible. This simple equation generates an extensive range of interactions between optics and mechanics.

If we send a laser beam into the cavity which is detuned from resonance, the effective temperature of the mechanical resonator changes [8]. If the beam is lower in frequency than the cavity resonance, or red detuned, the mechanical resonator is cooled and if the beam is blue detuned the mechanical resonator is heated. If the detuning, Δ is equal to the mechanical frequency, we can use the rotating wave approximation and rewrite the interaction Hamiltonian as the beam splitter Hamiltonian [8]:

$$H_I = \hbar g_0 \sqrt{n_c} \left(a^\dagger b + a b^\dagger \right) \tag{2.2.3}$$

This interaction swaps photons from the optical cavity with phonons from the mechanical resonator. This allows cooling of the mechanical resonator if the light is constantly removed from the cavity, as is almost always the case since the cavity decay rate, κ is much greater than the mechanical decay rate, γ [41, 42]. For the rotating wave approximation to be valid, $\kappa \ll \omega_m$. When this condition is met, it is possible to cool very close to the mechanical ground state of the resonator [41, 42]. Another possibility is to perform optomechanically induced transparency [43, 44, 45] or to transfer the state of an optical field to the mechanical resonator [46]. This is a means of precisely controlling the quantum state of the resonator [47]. For a more detailed introduction to cavity optomechanics see the reviews in Refs [8, 32] and the theses in Refs [48, 49, 50].

2.3 Generating a Spatial Superposition State

Now that we have introduced a means for precisely controlling a mechanical resonator, we would like to find a method for testing the novel decoherence mechanisms. The most direct test of these mechanisms is to build a superposition state between two different positions and to measure the decoherence of this state [22]. One possibility is sending a superposition state of 0 and 1 photons into an optical cavity; this state

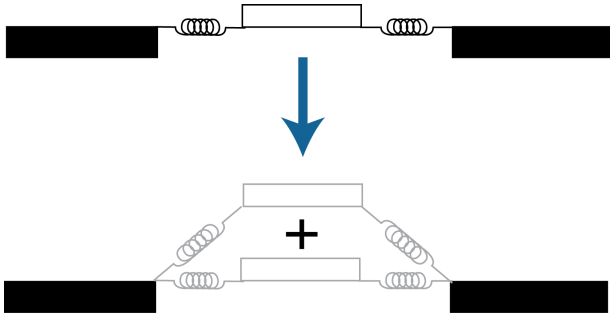

Figure 2.1: **Generation of a spatial superposition state.** We propose to take a mechanical resonator in its ground state (top) and put it into a spatial superposition state of moving and not moving in order to generate a spatial superposition.

would transfer to the mechanics via the radiation pressure force. This idea is at the core of the proposal by Marshall et al. [51]. A single photon is sent to a beam splitter, which leads to two cavities: one with a mechanical resonator and one without. If the interaction is strong enough the mechanical resonator is put into a superposition state: $1/\sqrt{2}(|0\rangle_m + |1\rangle_m)$. We can direct the single photon which leaks out of the two cavities back onto the beam splitter. If decoherence occurred it should destroy the ability of the photon to interfere with itself, giving a direct measurement of the decoherence time of the system.

There are a number of technical challenges required by the Marshall scheme: $\kappa < \omega_m$, $\omega_m < g_0$ and $\kappa < g_0$ [51]. The first requirement is feasible, but the second requirement is quite difficult and has only recently been achieved [52]. The final requirement has not yet been realized in an optomechanical system. There have been a number of schemes which extend the Marshall scheme and avoid some of these technical requirements. These include the use of postselection [53] and optical displacement of the photonic state [54, 55]. Both of these schemes dramatically reduce the requirements on g_0, but require long delay lines for storing the optical state during decoherence. In Chapter 7, we discuss a means of avoiding this issue by performing an interference experiment with two mechanical resonators.

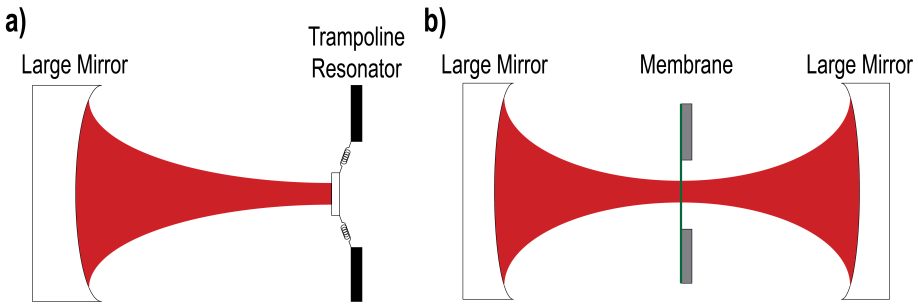

Figure 2.2: **Two Optomechanical Cavity Configurations. a)** A micromirror on a mechanical resonator is paired with a large mirror. **b)** A membrane is placed in the middle of a high finesse optical cavity.

Before attempting to generate a superposition state, the mechanical resonator must be brought close to its ground state using sideband cooling [56, 21]. As discussed in the last section, this also requires that the system be well sideband resolved. In addition, the coupling to the environment, γ must be small. In particular, we must meet the condition:

$$\gamma < \frac{\hbar\omega_m^2}{k_B T} \tag{2.3.1}$$

Ground state cooling can be made easier by precooling the bath temperature of the resonator, T to cryogenic temperatures. However, the mechanical quality factor of the devices, $Q = \omega_m/\gamma$ must also be high enough, which will be discussed in Chapters 4 and 5. Finally, in order to observe novel decoherence, the environmentally induced decoherence time (Equation 2.1.1) must be long, as discussed in Section 2.1. Fortunately, maximizing the decoherence time requires the same adjustments used for improving sideband cooling.

2.4 Macroscopic Cavity Optomechanics Implementations

Now that we have discussed some of the requirements for a system which might observe new physics, we will discuss two implementations, both with mm scale mechanical resonators with effective masses between 10 ng and 1 μg. The first is an optical cavity between a fixed external mirror and a mirror integrated into a mechanical device, as shown in Figure 2.2a. These cavities were first conceived and investigated in relation to gravitational wave detectors [57, 58, 59], which use macroscopic mirrors as test masses. Although LIGO's geometry is a little different (two moving mirrors instead of one), and the scale is many orders of magnitude larger, many of the engineering features can be applied to our system [60].

We choose to integrate a micromirror into a mechanical resonator. There are a number of implementations of this style of optomechanical cavity, including mirrors on silicon [61, 62], quartz [63], and silicon nitride [64, 65]. We will focus on and extend work on silicon nitride trampoline resonators [65]. In a single sided optomechanical cavity the optomechanical coupling rate and optical loss are:

$$g_0 = \frac{\omega_c}{L}\sqrt{\frac{\hbar}{2m\omega_m}} \tag{2.4.1}$$

$$\kappa = \frac{\pi c}{FL} \tag{2.4.2}$$

m is the effective mass, L is the length of the cavity and F is the finesse of the cavity. The characteristics of trampoline resonators are chosen as a compromise. The cavity length is 5 cm to match the achievable radius of curvature on superpolished substrates. This limits the optomechanical coupling rate to a few hertz, well below $\omega_m/2\pi$ = 300 kHz. The coupling rate is limited because the frequency must remain high enough for sideband resolution and cooling to the ground state. m is 150 ng, a compromise between

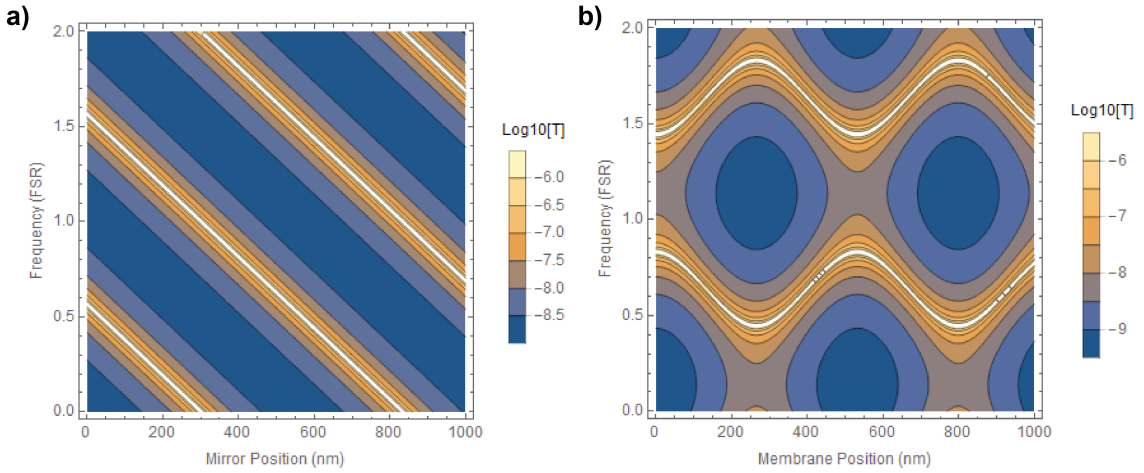

Figure 2.3: **Dispersion relationship for the two types of cavities.** We numerically simulate the transmission fraction through the cavity, T using the transfer matrix method. **a)** The dispersion relationship for a Fabry-Pérot cavity is linear, and the optomechanical coupling rate is constant. **b)** The peak transmission gives the dispersion relationship, which depends on the membrane position. The first and second derivative of this curve determine the first and second order optomechanical coupling rates, respectively. We can see that the dispersion relationship is the sum of two oppositely sloped cavities with half the length and an avoided crossing.

high mass for decoherence experiments and large optomechanical coupling rate. While the system is 5 orders of magnitude away from single photon strong optomechanical coupling, this optomechanical coupling is strong enough to potentially achieve strong multiphoton coupling. We investigate this type of cavity in Chapters 3,4 and 5.

Another optomechanical geometry is a high finesse cavity with two fixed mirrors and a movable membrane in the middle as shown in Figure 2.2b. The membrane changes the dispersion relationship inside the cavity and generates an optomechanical coupling rate to both the position (g_0) and the position squared (g_2) of the membrane [66]. As shown in Figure 2.3b, the optomechanical coupling rates, which are the first and second derivative of the dispersion, vary greatly depending on the position of the membrane. This can be useful for tuning optomechanical coupling rates. Such membrane in the middle systems have been studied extensively, with a range of sizes and thicknesses [66, 67, 68, 69]. Most fall in the parameter ranges of m = 1-40 ng, $\omega_m/2\pi$ = 200 kHz - 2 MHz

and L = 1 - 100 mm. A more comprehensive discussion can be found in the theses in Refs. [70, 71].

Because of the similarities between the parameters of the optomechanical systems, many of the investigations in this thesis apply to both systems. Membrane systems typically have higher mechanical quality factors than DBR based systems because junctions between materials are lossy [69, 72, 65]. The higher mechanical frequency also makes it easier to cool to the ground state, and a number of membrane systems have been cooled close to the ground state [35, 36, 73]. In contrast DBR trampoline resonators have lower frequency, and have a larger, more concentrated mass. This means they are less susceptible to air damping and decoherence due to gas particles in the vacuum. This might make it easier to study novel decoherence mechanisms. For this reason we focus on DBR trampoline resonators for the first several chapters. In Chapter 6, we will discuss hybrid devices that use a membrane in the middle of an optomechanical cavity.

2.5 Conclusion

Optomechanical cavities with mm-scale mechanical resonators are a promising platform for investigating quantum behavior in massive systems. There are a number of theoretical schemes for the creation of spatial superposition states using the optomechanical toolbox. With such states it may be possible to characterize the quantum to classical transition in macroscopic systems, and maybe even find novel decoherence mechanisms. In the chapters that follow we will study and construct optomechanical systems and techniques that address the unique challenges discussed in this chapter.

Chapter 3

High Finesse Optical Cavities

One half of an effective optomechanical system is an optimized optical cavity. We need a system which is well sideband resolved for many of the interactions discussed in chapter 2, such as optical sideband cooling and optomechanical state transfer. A simple geometry for creating an optomechanical interaction is a mirror integrated into a mechanical resonator. In this chapter we explore the possibilities for building a high finesse optical cavity between a large external mirror and a microfabricated integrated mirror in an optomechanical system. We test the limits of high finesse cavities with a large difference in mirror size and find that despite the challenging geometry we can achieve cavities which fully realize the capabilities of state of the art deposited mirrors. Furthermore, we find that the microfabrication process of the mirrors produces a curvature which can be used for ultrashort cavities and polarization non-degenerate cavities. We discuss techniques for verifying and testing the limits of a high finesse optical cavity.

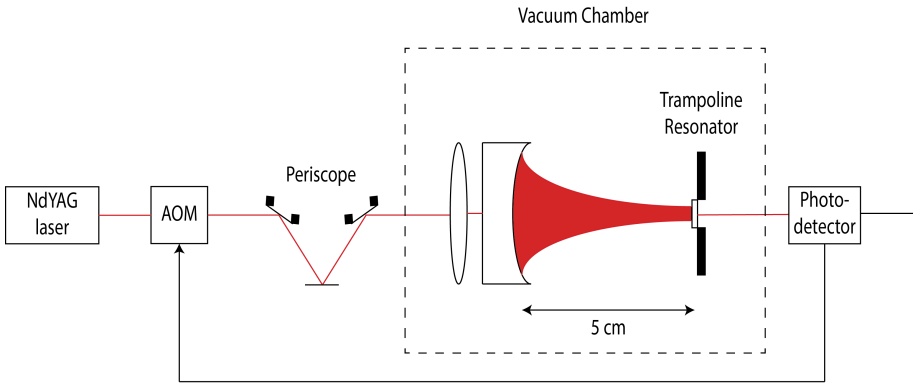

Figure 3.1: **Experimental setup for measuring finesse.** This is the experimental setup used to measure finesse. An acousto-optic modulator is triggered with an avalanche photodiode to take ringdown measurements in transmission.

3.1 Limitations to Finesse

We build an optomechanical cavity by placing a 'large' 1/2 in. or 5/8 in. mirror 5 cm away from a trampoline resonator. See Figure 3.1 for a schematic. The trampoline resonator consists of four high stress (LPCVD) Si_3N_4 arms for springs and a 'small' mirror 60 - 130 μm in diameter [65]. The mirrors are distributed bragg reflectors (DBR) made of alternating layers of SiO_2 and Ta_2O_5. The trampoline resonator has a mechanical resonance frequency around 300 kHz, which is lower than most optomechanical resonators, and is just below the lowest frequency mechanical resonators that have been cooled to the ground state to date [35, 73]. Because the mechanical frequency is so low, a high quality cavity is necessary to have a linewidth lower than the mechanical frequency (sideband resolution). We choose to optimize the finesse of the cavity, because the Q and linewidth depend heavily on the length.

There are four main processes which can limit the finesse of an optical cavity: transmission through the mirrors, scattering off the mirrors, absorption in the mirrors and mode leakage around the sides of the mirrors. The finesse of an optical cavity is given by the equation:

$$F = \frac{\pi (R_1 R_2)^{1/4}}{1-\sqrt{R_1 R_2}} \tag{3.1.1}$$

$$R_i = 1 - T_i - S_i - A_i - e^{-2w_i^2/D_i^2} \tag{3.1.2}$$

R_i is the reflection and T_i, S_i and A_i are transmission, scattering and absorption losses for the i_{th} mirror, all given as a fraction of the power. w_i is the beam waist at the mirror and D_i is the diameter of the mirror.

The transmission is determined by the number of layers in the DBR stack, and is a parameter of the coatings we buy from coating companies. The ideal cavity is only limited in finesse by transmission, because all of the light lost from the cavity passes into useful channels which can be sent to detectors. Fabrication errors and diffraction losses can also act to lower the finesse. Absorption is a material property of the constituents of the DBR stack: SiO_2 and Ta_2O_5. These materials are a standard choice for DBR mirrors because they typically have low optical absorption in the near infrared on the order of 1-2 ppm [74, 75, 76]. Finally, based upon previous investigations [77, 48], we use superpolished substrates with $\sim$ Å surface roughness. This ensures that the scattering losses are also kept below 3 ppm [48]. These constraints are all consistent with a finesse dominated by transmission losses.

In order to understand the diffraction loss, we examine the Gaussian beam properties of the cavity mode. The mode must match the curvature of the large mirror and be focused to a small point at the small mirror, leading to the following conditions on w_1 and w_2:

$$C = L\left(1 + \frac{\pi^2 w_1^4}{\lambda^2 L^2}\right) \tag{3.1.3}$$

$$w_2 = w_1\sqrt{1 + \frac{\lambda^2 L^2}{\pi^2 w_1^4}} \tag{3.1.4}$$

C is the curvature of the large mirror, which is fixed at 50 mm, and L is the length of the cavity. Because of the large size difference between the mirrors, the only way to focus the light down enough is to have $L = C - \delta L$, where δL is a small displacement. With this assumption and the approximation that L is far greater than w_1, we can simplify Equations 3.1.3 and 3.1.4:

$$\delta L \approx \frac{\pi^2 w_1^4}{\lambda^2 C} \tag{3.1.5}$$

$$w_2 \approx \frac{\lambda C}{\pi w_1} \tag{3.1.6}$$

The beam waist depends critically on the length of the cavity in this regime, because our cavity operates in the near hemispherical regime. In contrast systems with two large mirrors in a confocal configuration are more stable and less limited by the size of the mirrors. Furthermore, if we make w smaller for one mirror, it will necessarily be bigger for the other mirror. Ideally, however, we can find a beam waist where the loss on both mirrors is small.

We measure finesse by observing the ringdown time of light leaking out of the cavity. The setup is shown in Figure 3.1. We use two equivalent techniques: scanning the laser frequency and scanning the length of the cavity with a ring piezo. When the laser is resonant with the cavity we cut the beam off with an acousto-optic modulator (AOM). We then measure the transmitted light on an avalanche photodetector (APD), and fit an exponential to the ringdown signal. This only works for ringdowns significantly longer than the response time of the AOM (several nanoseconds), so we measure low finesses by scanning the cavity or laser frequency and fitting the linewidth of the Lorentzian profile of the transmitted light directly.

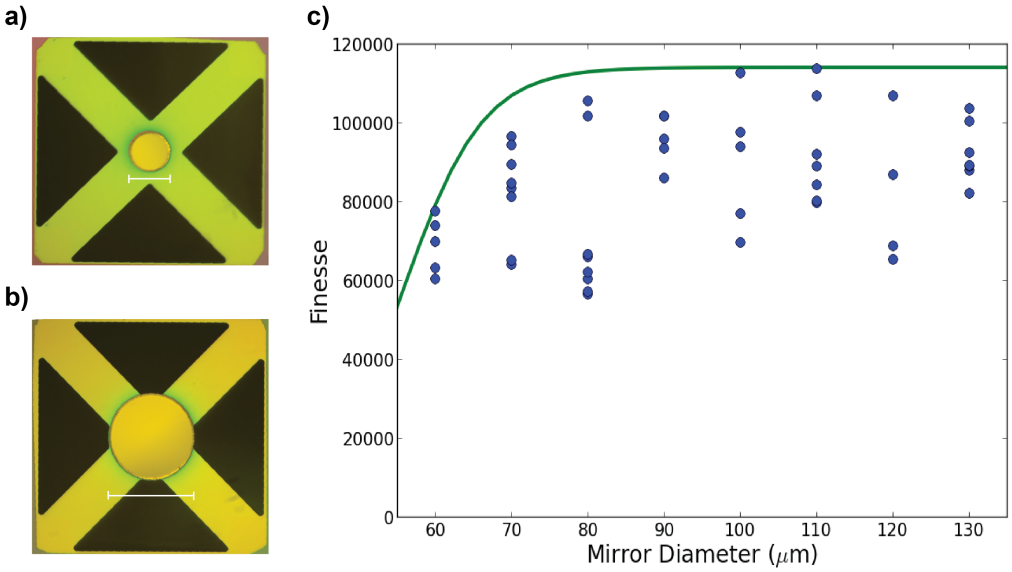

Figure 3.2: **Finesse vs small mirror size.** Optical microscope images of trampoline resonators with mirror diameters of **a)** 60 μm and **b)** 120 μm, indicated by the scale bars. **c)** shows the finesse for trampoline resonators fabricated with different sized DBR mirrors. The spread in the blue points is caused by fabrication imperfections, but the best devices can be used to determine the overall trends. The green fit gives a theoretical estimate of the parameters of the system with D = 6.4 mm for the large mirror and $T + S + A = 27.5$ ppm for the two DBR mirrors.

3.2 Finesse vs Mirror Size

We begin our study of finesse with a systematic study of the size of mirrors necessary to generate a high finesse cavity. For the short term, smaller mirrors are ideal, because the devices have a higher resonance frequency, and are easier to optically cool. To investigate the diffraction and scattering losses in real fabricated devices, we fabricate a series of trampoline resonators with mirror diameter ranging from 60 μm to 130 μm. The results are shown in Figure 3.2. Because any imperfection in the fabrication process will cause scattering, there is a large variation in finesse for each mirror size. However, if we take the best device for each mirror diameter, finesse increases with mirror size for small mirror sizes, but plateaus for larger mirror sizes. From this we estimate that we need a mirror diameter of at least 80 μm to avoid diffraction losses.

It is also interesting to compare to a theoretical limit based on diffraction losses. If we assume the diameters of the small mirrors and optimize the beam waist to maximize the finesse we get the green curve in Figure 3.2. From this we determine the diameter of the large mirror, D = 6.4 mm, which is significantly smaller than the actual diameter of 15.9 mm. Most likely, there is either long scale roughness or dirt on the large mirror which limits its usable size. Because of the large size of the mirror it is quite vulnerable to dust from the environment. The coating losses, $T + S + A$ = 27.5 ppm, and plateau finesse match the specifications of the coatings. Based on our estimates of S and A, we can see that T is approximately 22 ppm. We have therefore demonstrated that for a sufficiently large small mirror, we can achieve the ideal regime where the transmission losses dominate the finesse.

3.3 Alignment and Maximal Finesse

Once we have a device with a good finesse, it is important to understand how alignment changes the finesse. Because the cavity is almost diffraction limited, the range of cavity lengths that support a high finesse cavity mode is small. As we showed in the previous section, mirrors larger than 80 μm in diameter have excess space, and they can support a larger beam waist. We also find that the cavities with larger mirrors can support a number of higher order modes up to approximately the (5,5) mode. There are a number of optomechanical schemes which could use multiple of these optical modes [78, 79]. However, for most experiments we only wish to use the fundamental mode.

Ultimately the goal is to cool these optical cavities down, so that the mechanics can reach the quantum regime. The 5 cm long optical cavity is expected to shrink by several hundred microns. It is therefore necessary to build in some flexibility in the length of the cavity and the position of the beam on the mirror. We perform an experiment in

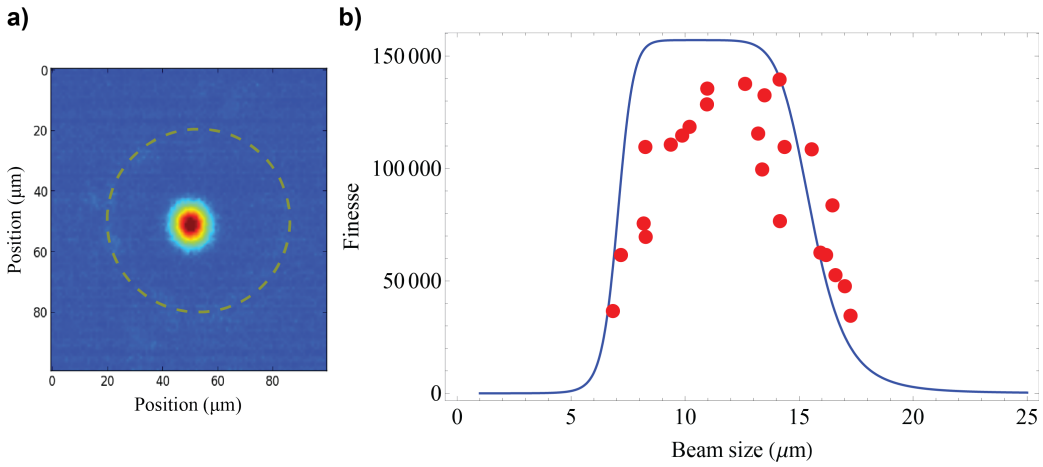

Figure 3.3: **Finesse vs mode size for a 70 μm mirror. a)** The Gaussian beam profile on the small mirror (outlined in a yellow dashed line.) **b)** We measure finesse as we change the length of the cavity such that the beam waist on the small mirror changes. There are three regions visible. From left to right, the finesse is limited by: losses due to the finite large mirror size, transmission through the coating and diffraction losses around the small mirror. Because the middle region is very small, we can deduce that a 70 μm mirror is about the smallest we can make a mirror and maintain a high finesse.

which we vary the length of the cavity and measure the beam waist and finesse. Figure 3.3a shows a cross sectional image of the gaussian mode, which we used to extract the beam waist at the mirror. Figure 3.3b shows the finesse as a function of mode size. In this figure you can see three regions with different limits for the finesse. At small beam waist, the finesse is limited by diffraction losses on the big mirror. At large beam waist, the finesse is limited by diffraction around the edges of the small mirror. In the middle the finesse is limited by the quality of the optical coatings. The agreement with the theory curve indicates that unlike in the previous section we can use almost the entire surface area of both mirrors. This means the large mirror used in this section has less long scale roughness and dirt. The relatively small intermediate region indicates that a 70 μm mirror is at the limit of devices which can achieve maximal finesse, which agrees with the results of the previous section.

A number of different coatings have been used. These are discussed in detail in ap-

pendix ???. With the best coating combination we obtained a finesse of 181,000 ± 1,000. The data for this are shown in the next chapter.

3.4 Curved Mirrors and Polarization Non-degenerate Cavities

The discussion in this section is based upon a publication with permission from the authors [80].

So far we have treated the small trampoline mirrors as completely flat uniform objects, but in reality this is not the case. There are a number of stresses in the material layers of the trampoline resonator which cause the mirror to curve. The SiO_2 and Ta_2O_5 layers of the DBR mirror all have compressive stress, causing an outward radial force while the Si_3N_4 layer at the bottom has tensile stress causing an inward radial force. The net result is the buckling of the mirror into a convex shape. We characterize the mirror profiles using confocal microscopy. The results for one such mirror are shown in Figure 3.4a and b. We find that the curvature depends on the size of the mirror and the stress of the nitride, and we find mirrors with radius of curvature ranging from 1.4 mm to almost flat. Mirrors with a broken trampoline arm have a much greater curvature, indicating that larger curvature is possible through changing the geometry of the trampoline. Simulations in COMSOL verify that this curvature can be explained by the stress in the layers.

Curved mirrors at the micron scale have recently been used to make short high finesse cavities which are tens to hundreds of microns long [81, 82]. These short cavities have a small mode volume, and hence have a large Purcell enhancement, which is useful for cavity QED experiments. The short length also increases the single photon

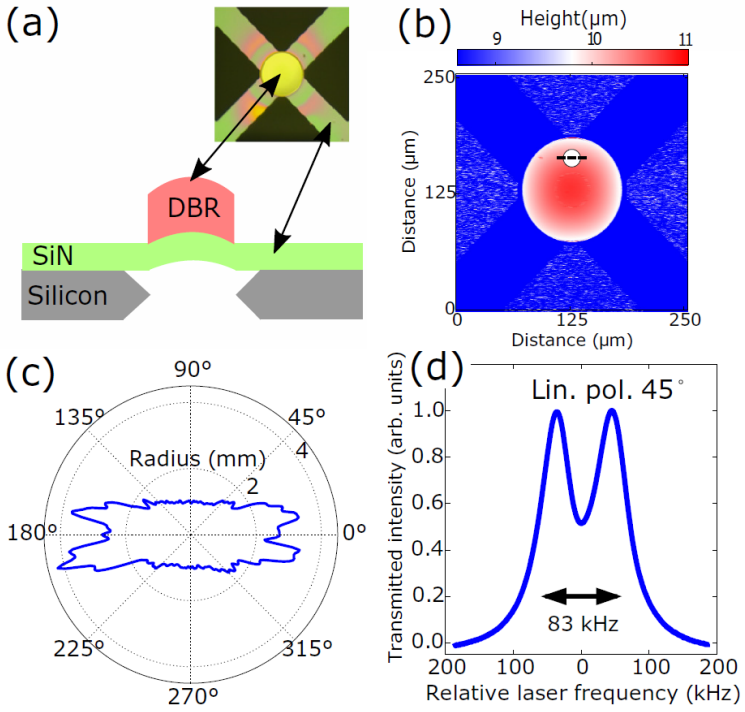

Figure 3.4: **Polarization splitting in an optomechanical cavity. a)** Differences in stress between the layers of the mirror structure cause the mirror to bend into a convex shape. The inset shows an optical microscope image of the device used in these studies. **b)** A confocal microscopy image of the device in **a)** shows the height profile of the mirror. **c)** From the height profile data we can extract the curvature at a certain point (the white circle in **b)**). We take a line cut (also shown) and rotate to find the radius of curvature at each angle. The net result of the polarization nondegeneracy in **c)** is a polarization splitting of the fundamental cavity mode. **d)** shows the two split optical modes which are both addressed by light at a 45° angle. Figure courtesy of Frank Buters.

optomechanical coupling strength, g_0 which is proportional to 1/L. Although the cavity linewidth, κ also increases as 1/L, the single photon cooperativity, $4g_0^2/\kappa\gamma$ improves for short cavities as 1/L. Even with the high finesses we achieve here, a cavity with a length of several hundred microns would not be sideband resolved. However, cooling a mechanical resonator very close to its grounds state has recently been demonstrated using feedback cooling in a non-sideband resolved cavity [83]. Our curved mirrors, which are already integrated into a mechanical system, are a natural choice for exploring optomechanics in the short cavity regime.

In addition to enabling short cavities, the curvature of our mirrors also has polarization effects. Towards the center of the mirror, the cross sectional profiles of the mirrors fit quite nicely to parabolas which are isotropic in different directions. This means that the mirror can be used for a radially symmetric optical cavity. However, towards the edges of the mirror the presence or absence of supporting Si_3N_4 legs lifts the degeneracy between different directions. The resulting difference in radius of curvature along orthogonal directions is shown in Figure 3.4c, and it leads to a polarization splitting in the frequency of the horizontal and vertical cavity modes (Figure 3.4d.)

We investigate the effects of the polarization splitting on the optomechanical properties of the cavities. Two effects of a detuned laser in an optomechanical system are shifting the resonance frequency via the optomechanical spring effect and damping (or driving) the resonator because of sideband cooling (or heating.) If we send in linearly polarized light at 45° to the vertical axis it should be possible to address both polarization modes at the same time, and hence interact with the optomechanical cavity at two different detunings with a single laser beam. In Figure 3.5 we perform a detuning sweep of a laser at 45°. We see that the frequency shift and mechanical damping match perfectly with theoretical predictions based on the sum of the effects of the two cavity modes (dashed green lines.) We observe a polarization splitting of 83 kHz, which

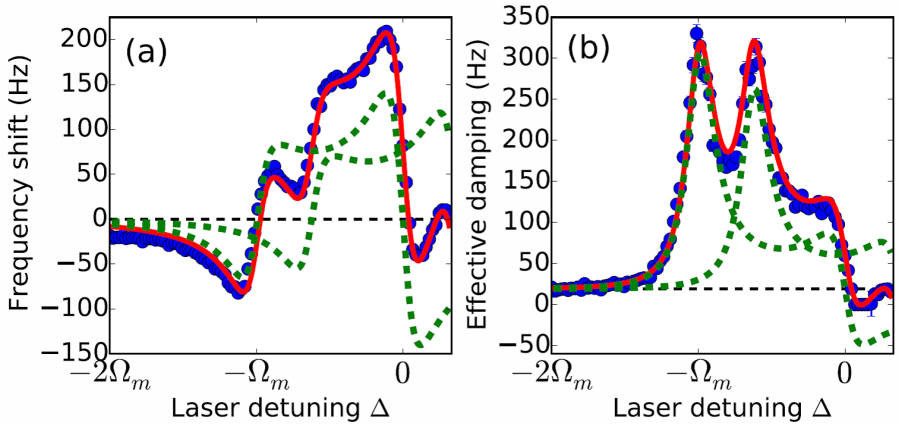

Figure 3.5: **Polarization nondegenerate detuning sweep.** We inject a single laser beam polarized at 45° with respect to the cavity modes, so that it addresses both modes equally. If we adjust the detuning of the laser beam, we can recover the frequency response **a)** and damping response **b)** of the two modes at detunings spaced by the polarization splitting. Δ is the detuning of the lower frequency mode from the cavity resonance. The red curve is a fit to theory, and the two green dashed curves are the theoretical curves for each single mode optomechanical system. Figure courtesy of Frank Buters.

is larger than the cavity linewidth, 52 kHz. The splitting is consistent with calculations based upon the two radii of curvature [84].

This polarization splitting could enable a number of new optomechanics experiments, because we can access two frequency detunings with a single laser beam. In particular, if the polarization splitting were tuned to two times the mechanical frequency, we could address both the red and blue optomechanical sidebands at the same time. First, if light were sent in at 45° it would be possible to measure the relative size of the Stokes and anti-Stokes sidebands, and hence deduce the temperature based on the polarization angle exiting the cavity [80]. Second, access to the red and blue sidebands could be used to generate and optomechanical superposition state. This has been suggested with multiple laser beams as a means of state orthogonalization [85], but here it can be done with a single laser beam and a polarizer. If the mechanical resonator is prepared in a single phonon Fock state using postselection [86, 38], this would gen-

erate a superposition state of the second excited state and the ground state [80]. The polarization splitting we demonstrate here is smaller than the mechanical frequency, but by tweaking the geometry of the arms of the trampoline or by shortening the cavity it should be possible to carry out these experiments.

3.5 Conclusion

We optimized a 5 cm long optical cavity with a micrometer scale end mirror for high finesse, reaching the regime where finesse is only limited by the coatings and most light lost from the cavity is transmitted into useful channels. The characterization techniques for determining the limits of finesse are useful for maintaining an optomechanical system with high finesse. Furthermore, we have demonstrated control over the polarization and curvature of the mirrors, such that we could create very short cavities or cavities with a large polarization splitting. The trampoline resonators fabricated in this section were the basis for the more complex devices discussed in the rest of this thesis. Furthermore, they were used for a number of optomechanical studies, including a study of optical sideband cooling [87] and an exploration of the optomechanical attractor diagram [88].

Chapter 4

Nested Trampoline Resonators

Two major challenges in the development of optomechanical devices are achieving a low mechanical loss rate and vibration isolation from the environment. We design and fabricate a DBR trampoline resonator embedded within a lower frequency mechanical resonator, with 80 dB of mechanical isolation from the mounting surface at the inner resonator frequency. We also develop an electrical feedback system for stabilizing the vibrations of the outer resonator. The consistency and high mechanical quality factor provided are crucial for succesful optomechanics experiments, both in the classical and quantum regime.[1]

4.1 Introduction

In this chapter we focus on our efforts to produce a large mass mechanical resonator with both high mechanical and optical quality factor, which can realistically be cooled to its ground state. There are several requirements for the devices to achieve this. The system must be sideband resolved for optical sideband cooling to the ground state [41, 42].

[1] The contents of this chapter are based on the work by Weaver et al. [89], and are used with permission from the authors.

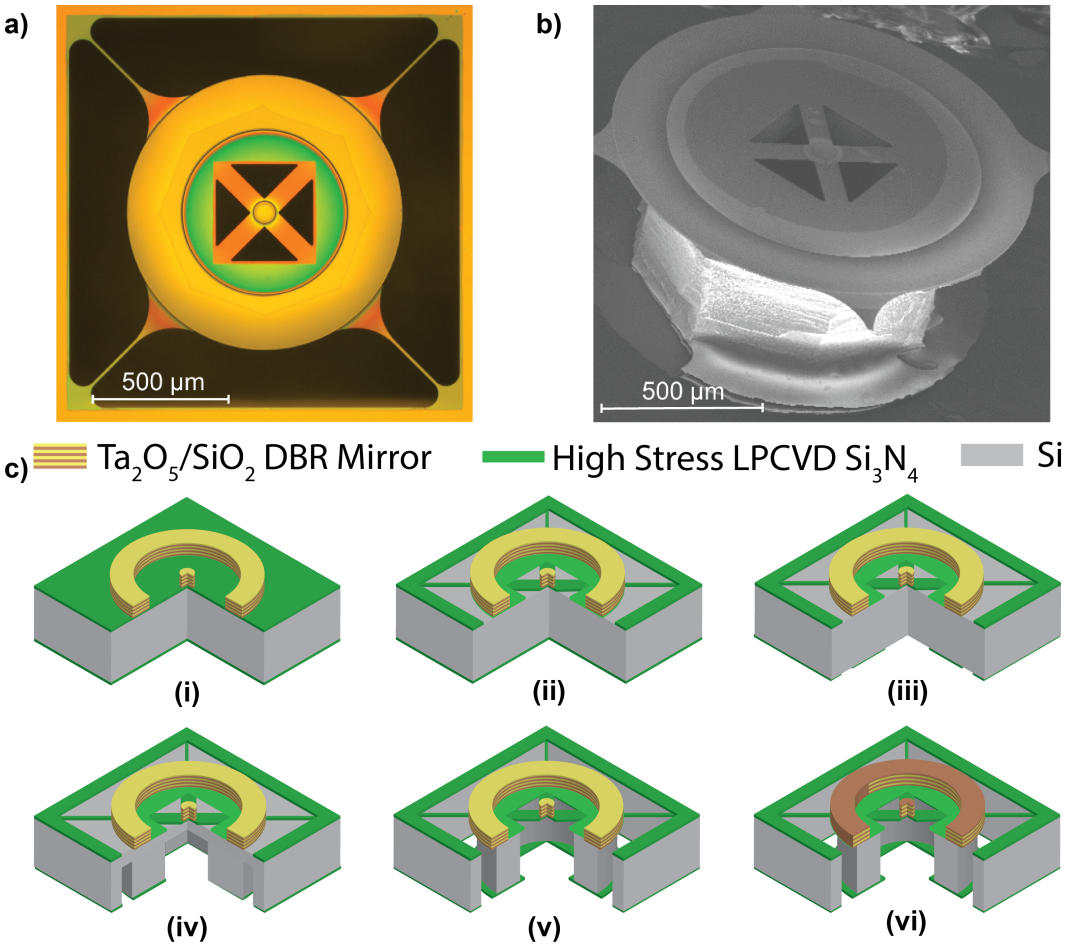

Figure 4.1: **Nested trampoline resonator fabrication.** Optical **(a)** and SEM **(b)** images of a nested trampoline resonator. The device was broken out of the chip to make the structure visible for **(b)**. Note the thin 10 µm wide, 500 nm thick arms supporting the large 500 µm thick silicon mass. A properly sized mirror layer was necessary to protect the nitride layer from sharp edges in the silicon and safely connect to the thin arms of the outer resonator. **(c)** A schematic overview of the fabrication process (not to scale). **(i)** The SiO_2/Ta_2O_5 DBR stack is etched via CHF_3 ICP etch. The front **(ii)** and back **(iii)** Si_3N_4 is etched by CF_4 plasma etch. **(iv)** Most of the Si is etched from the bottom using the Bosch process. **(v)** The remainder of the Si is etched via TMAH. **(vi)** A buffered HF dip cleans the devices and removes a protective SiO_2 layer. Only 6 layers of the SiO_2/Ta_2O_5 DBR stack are shown, and the shape of the outer resonator mass is approximated as a hollow cylinder for simplicity.

A high mechanical quality factor is also necessary to generate a higher cooperativity and a lower mechanical mode temperature for the same cooling laser power. Furthermore, in the quantum regime, the quality factor sets the timescale of environmentally induced decoherence [9], which is crucial for proposed future experiments. Therefore, it is important to eliminate mechanical and optical loss sources.

One major source of loss in mechanical systems is clamping loss, which is coupling to external mechanical modes [90, 91, 69]. As we will show, this is a critical source of loss for Si_3N_4 trampoline resonators. Several methods of mechanically isolating a device from clamping loss have been demonstrated including phononic crystals [92, 93] and low frequency mechanical resonators [94, 62, 95, 96, 97]. Due to the large size of phononic crystals at the frequency of our devices (about 250 kHz), we have selected to surround our devices with a low frequency outer resonator. We significantly improve on the design of similar devices using silicon optomechanical resonators [98] by using a lower frequency outer resonator and silicon nitride with weaker spring constant. Weaker spring constants lead to higher optomechanical coupling, a requirement for our future experiments. The outer resonator acts as a mechanical second order low pass filter with the following mechanical transfer function [99]:

$$T(\omega) = \frac{\omega_o^4}{(\omega_o^2 - \omega^2)^2 + \gamma_o^2 \omega^2} \tag{4.1.1}$$

ω is the frequency of vibration, ω_o is the frequency of the outer resonator and γ_o is the mechanical loss rate of the outer resonator. Choosing an outer resonator frequency of 2.5 kHz and an inner resonator frequency of 250 kHz leads to approximately 80 dB of isolation of the inner resonator. This isolation is independent of γ_o (If $\omega >> \omega_o$, the transfer function is well approximated as $T(\omega) = \omega_o^4/\omega^4$, which falls off at 40 dB per decade and is independent of the outer resonator quality factor.) The nested trampoline resonator

scheme promises both a high mechanical quality factor independent of mounting and mechanical isolation from the environment.

Our optomechanical system is a 5 cm long Fabry-Pérot cavity consisting of a large distributed bragg reflector (DBR) mirror deposited on a SiO_2 curved surface and a nested trampoline resonator device. The nested trampoline resonator has a small DBR mirror (80 μm in diameter) mounted on four Si_3N_4 arms, surrounded by a large silicon mass held in place by four more Si_3N_4 arms (See Figure 4.1). Previously, we have fabricated single resonator devices with plasma enhanced chemical vapor deposition (PECVD) low stress nitride [65]. In this letter, we use high stress low pressure chemical vapor deposition (LPCVD) Si_3N_4, because it generally has higher frequency and lower intrinsic loss [100]. The stress is typically around 1 GPa for LPCVD Si_3N_4 [101], but comparisons between Finite Element Analysis models and the observed frequencies of fabricated devices indicate that the stress is probably closer to 850 MPa in this case.

4.2 Fabrication

Devices are fabricated starting with a superpolished 500 micron thick silicon wafer. Either 300 or 500 nm of high stress LPCVD Si_3N_4 is deposited on both sides of the wafer, and a commercially procured SiO_2/Ta_2O_5 DBR is deposited on top. The DBR is etched into a small mirror on the inner resonator and a protective mirror layer on the outer resonator using a CHF_3 inductively coupled plasma (ICP) etch. Next, the Si_3N_4 arms of the devices are patterned with a CF_4 etch. A window is also opened on the back side Si_3N_4 with a CF_4 etch. Approximately 400 microns of silicon under the Si_3N_4 arms are removed from the back using the Bosch deep reactive ion etch process. A large silicon mass is left in place between the inner and outer arms of the device. The devices are then released with a tetramethylammonium hydroxide (TMAH) etch. Finally a buffered HF

etch removes the top protective buffer layer of SiO_2 without damaging the underlying Ta_2O_5 layer. Figure 4.1 shows a schematic summary of the fabrication process.

Devices are characterized using a 1064 nm NdYAG laser. To measure mechanical motion, the Fabry-Pérot cavity is first intentionally misaligned to a finesse of around 100 to avoid any optomechanical effects. The cavity is then locked to the laser frequency at the inflection point of a Fabry-Pérot fringe using a piezoelectric actuator moving the position of the large mirror. Quality factors are taken from Lorentzian fits to the power spectral density of the Brownian motion of the devices. Finesse is measured by optical ringdown [65].

4.3 Results

4.3.1 Single Resonators

As an initial step, a series of single trampoline resonators with 60 μm diameter mirrors and varying geometries were fabricated and the mechanical quality factors measured [88, 87]. Three of the devices are pictured in Figure 4.2. We observed no significant geometric trends in quality factor. However, we found that remounting the same sample can change the quality factor of the devices by more than a factor of 10. Table 4.1 shows the quality factors for the devices on one chip mounted three separate times. It is clear that mounting drastically affects the quality factor; we attribute this to a change in the clamping loss, because we observe mechanical modes in the system around the resonance frequency that change in number, frequency and power with mounting. Clamping loss can be modeled as a coupling to these external mechanical modes [102, 90].

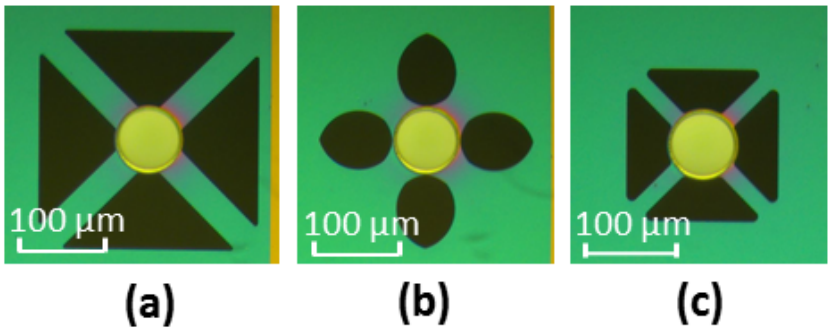

Figure 4.2: **Optical microscope images of three single resonator devices.** A number of different geometries were fabricated with different arm length, arm width and fillet size.

Mounting	Device a	Device b	Device c
1	425,000 ± 32,000	80,000 ± 4,000	33,000 ± 2,000
2	38,000 ± 2,000	5,000 ± 1,000	40,000 ± 2,000
3	264,000 ± 21,000	16,000 ± 1,000	113,000 ± 8,000

Table 4.1: **Single resonator quality factor variance with mounting.**This table shows the quality factors for the three devices pictured in Figure 4.2 with three different mountings. The importance of clamping loss is evident from the changes in quality factor of more than a factor of ten based on the mounting.

4.3.2 Double Resonators

We now turn to the nested trampoline resonators (see Figure 4.1.) The outer resonator acts as a low pass filter, providing 40 dB of isolation for every decade of frequency difference between the inner and the outer resonator (see Equation 4.1.1.) To test the mechanical isolation we performed a vibration transmission experiment. We attached a ring piezo to the sample mount with springs and applied a sinusoidal signal of varying frequency to the piezo. We measured the motion of the chip using a Michelson interferometer and the motion of the inner mirror using a low finesse Fabry-Pérot cavity as described above. The ratio of these two signals is the mechanical transmission from the chip mounting to the inner mirror.

This challenging experiment required eight orders of magnitude to be measured in

the same frequency scan. Because of insufficient laser scanning range, the Michelson interferometer was uncalibrated and the DC response was used for calibration. Due to the requirement for a single scan, measurement averaging time was limited by drift in the interferometer. The mechanical response of the piezo also dropped off significantly after 100 kHz, so it was not possible to measure the mechanical transmission at the frequency of the inner resonator. Figure 4.3 shows the transmission for both a single and a nested resonator. The data are binned for clarity, with the error bars reflecting variations within each bin. The experimental data follow the trend predicted by Equation 4.1.1 quite well. The theory curve is not a fit; ω_o and γ_o were determined through independent measurements. The deviations at high frequency are likely due to insufficient signal to noise ratio. The results clearly indicate that the outer resonator provides approximately 40 dB per decade of mechanical isolation. We can only measure a maximum of 45 dB of isolation, but we would expect 80 dB of isolation if we continued the measurement up to the inner resonator frequency.

We also tested the mounting dependence of the quality factor. The results of remounting a single nested resonator five times are shown in Table 4.2. The quality factor of the outer resonator changes drastically between the mountings, indicating that the mechanical clamping loss is changing. However, the inner resonator only demonstrates changes in quality factor on the order of 10%. The relatively small variation in quality factor of the inner resonator and the absense of extra mechanical peaks around the resonance frequency indicate that the clamping loss of the device has largely been eliminated. Indeed, all nested resonators fabricated without any obvious physical defects had quality factors between 300,000 and 500,000. The highest quality factor achieved was 481,000 $\pm$ 12,000, an order of magnitude larger than for comparable silicon devices at room temperature [98]. Typical quality factor measurements for an inner and outer resonator are shown in Figure 4.4.

Mounting	Inner Resonator Q	Outer Resonator Q
1	418,000 ± 11,000	700,000 ± 100,000
2	427,000 ± 10,000	690,000 ± 100,000
3	481,000 ± 12,000	70,000 ± 20,000
4	462,000 ± 14,000	240,000 ± 40,000
5	457,000 ± 13,000	220,000 ± 40,000

Table 4.2: **Nested resonator quality factor variance with mounting.** This table shows the quality factors of a nested trampoline resonator remounted five different times. The outer resonator quality factor (measured via ringdown) has large variation between the mountings while the inner resonator quality factor (measured via a fit to thermal motion) has only small variation between the mountings.

One concern for experiments with this system is the thermal motion of the outer resonator (10-100 pm rms at room temperature). Because of the narrow linewidth of the cavity, the optical response to such a large motion is nonlinear. However, the frequency of the outer resonator is low enough that a PID controller can lock a laser to the cavity, tracking the motion and removing any nonlinear effects. In addition, if the laser is locked with a slight negative detuning from the cavity resonance, the outer resonator can be optomechanically cooled, even without being sideband resolved [8]. Thus, the motion of the outer resonator does not prevent experiments using the inner resonator.

4.3.3 Optical Finesse

Another concern is maintaining the high quality of the DBR mirror layer through the fabrication process. Reducing the optical loss rate is critical to developing a system that allows quantum optical manipulation of mechanical motion. One way to reduce the optical loss rate is through superpolishing the wafer surfaces before deposition of the DBR, to reduce scattering. The addition of this step, as well as the selection of very highly reflective DBR coatings enable us to achieve a Fabry-Pérot cavity with finesse 181,000 ± 1,000, (optical linewidth 17 kHz) the highest finesse reported in an optomechanical Fabry-Pérot system. The ringdown measurement is shown in Figure 4.4. All of the nested

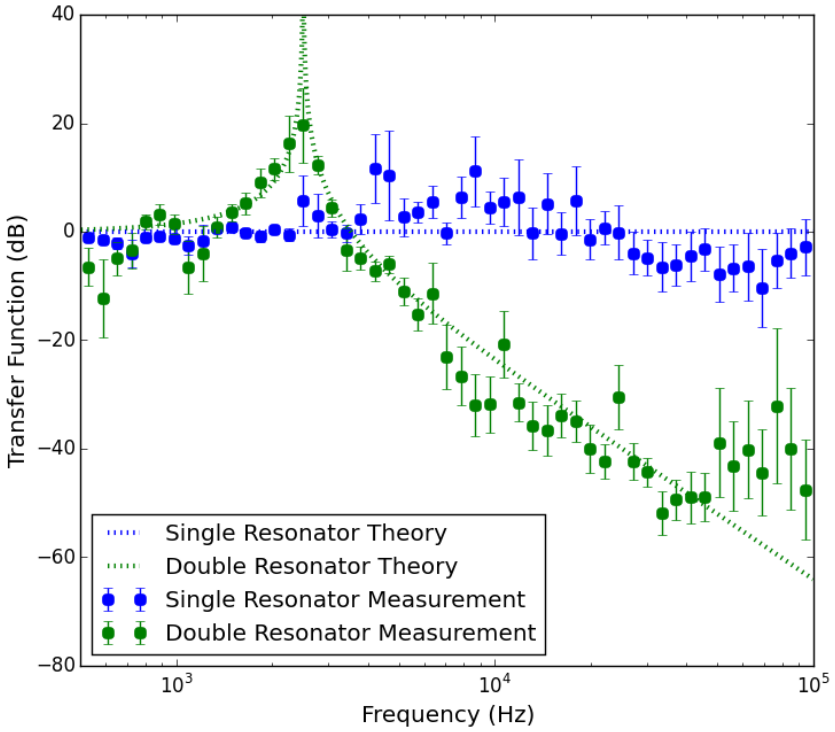

Figure 4.3: **Transfer function of a single and nested resonator.** A sample mount with a single (blue) and nested (green) resonator was mechanically driven at a range of frequencies. The motion of the outer chip and the inner mirror were measured to get the mechanical transfer function. The height at DC frequencies is adjusted to zero. This plot demonstrates that the nested resonator scheme provides mechanical isolation as predicted by Equation 4.1.1.

resonators measured have finesse greater than 160,000, indicating that the nested trampoline fabrication process is completely compatible with maintaining highly reflective mirror surfaces.

4.4 Discussion

Improvements in finesse and mechanics will enable new experiments with trampoline resonators. Our system (using the device in Figure 4.4) is fourteen times sideband resolved, which is more than sufficient for experiments such as quantum nondemolition measurements [103]. The elimination of the clamping loss will enable another systematic study of the geometry like the one attempted with single resonators. Many mechanical devices using Si_3N_4 without a DBR have much higher quality factor [104, 93, 94]. Varying the design of the inner resonator could allow reduction of mirror-nitride loss and fabrication of devices with even higher quality factors.

The improvements in mechanical isolation should also enable optomechanical cooling to the ground state. The devices are shielded from environmental mechanical noise, which previously could obscure motion at the quantum level. The fQ product of $1.1\text{x}10^{11}$ Hz (for the device from Table II) is also high enough for cooling to the ground state from 4 K, potentially alleviating the need for a dilution refrigerator. Our sideband resolution yields a theoretical minimum of $3 \text{ x } 10^{-4}$ phonons from optical cooling if there is no heating of the system [41].One concern is the thermal conductivity of our design, because at 4 K the thermal conductivity of Si_3N_4 drops to about 10^{-2} W/mK [105, 106]. The heat conduction is limited by the arms of the outer resonator, which are five to fifteen times narrower than the arms of the inner resonator. We have previously thermalized single resonators to 100 mK temperature, so thermalizing a double resonator sample to 4K, even with the narrower arms, should not be a problem.

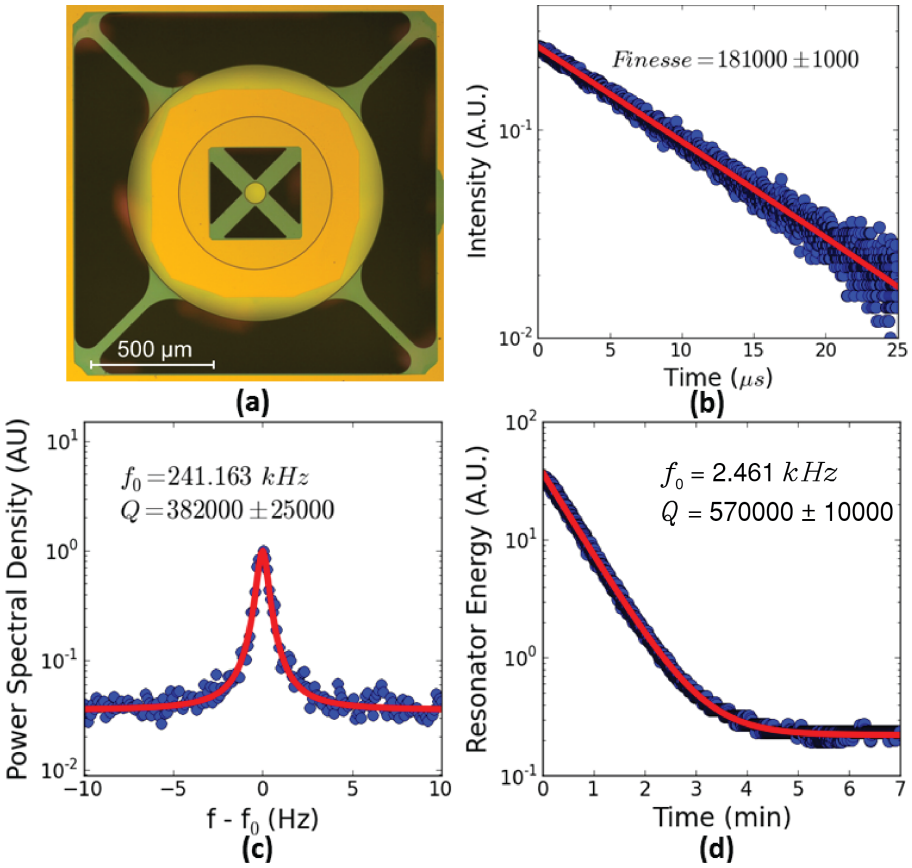

Figure 4.4: **Measurements of a nested trampoline resonator** (the same device as for Figure 4.3.) (a) Optical microscope image. (b) Optical ringdown to measure the cavity finesse. (c) Lorentzian fit to thermal motion of the inner resonator to measure quality factor. (d) Mechanical ringdown of the outer resonator to measure quality factor taken using a lock-in amplifier.

4.5 Electrical Feedback and Active Stabilization

We have shown that passive filtering using an outer resonator effectively isolates a mechanical resonator from the surrounding substrate. However, the price paid for this is an increase in the transfer of external mechanical noise around the frequency of the outer resonator, as can be seen in Figure 4.3. The reason for the large increase in noise is the large Q of the outer resonator, but the isolation is independent of mechanical quality factor (see Equation 4.1.1 in the limit where $\omega \gg \omega_0$.) Therefore, the ideal isolation system is critically damped (Q=1), so that there is very little added noise at the outer resonator frequency. This turns out to be crucial in cooling experiments, because our cryostat has many vibrations in the low kHz regime, which make locking the optical cavity with a high Q oscillator impossible.

We use electromechanical feedback on the outer resonator, because this can easily be integrated into a separate feedback circuit without affecting optomechanics experiments at the inner resonator frequency. We implement two geometries: a capacitor plate and an electric needle. The capacitor is formed between the bottom surface of the outer resonator, which is coated with aluminum, and an external chip which has an Al plate recessed by 20 μm. The alignment between two chips and the bonding of wires to inside facing surfaces are challenging. However, we can actuate motion of the mechanical resonator using this technique, and control the motion of the outer resonator [50]. This plate to plate geometry could be useful for measurements of the Casimir force between superconductors with the large force sensitivity of optomechanics.

Because of its simpler design, placing a ring shaped metal needle behind the sample is an easier way to integrate electrical feedback into our existing optomechanical setup [107]. We can build in a damping feedback circuit on the outer resonator which measures the outer resonator position with an interferometer and feeds back a voltage which

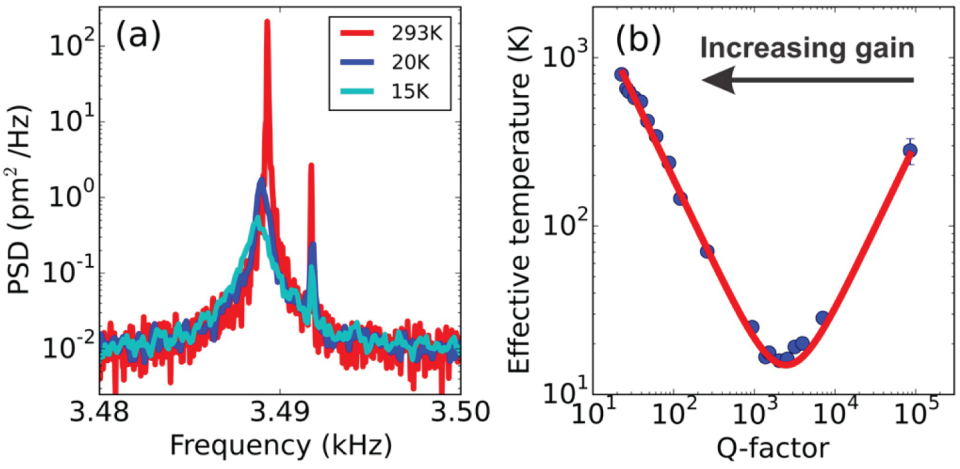

Figure 4.5: **Electrical feedback cooling of the outer resonator. a)** Power spectral density curves for three different electrical gain factors. The area under the curve is proportional to the effective temperature of the device. **b)** For increasing gain the quality factor can be continuosly reduced, but the temperature increases for large gain. Figure courtesy of Frank Buters.

induces a force on the dielectric material of the resonator. This can be run completely independently from the optomechanical cavity experiment, and is a useful experimental technique for the experiments in Chapter 6. See [49] for a more complete discussion of the operation of outer resonator vibration damping.[2]

We can now test the effectiveness of electrical feedback on damping the resonator. Figure 4.5 shows effective temperature and Q measurements for varied gain in the electrical circuit. The effective temperature lowers for increasing gain, but then increases again as noise from the interferometer is fed back into the mechanical system. The quality factor can be reduced by more than three orders of magnitude, which is sufficient to avoid large vibrations around the outer resonator frequency. This form of stabilization is sufficient for locking a laser to a high finesse cavity in a dilution refrigerator with a noisy mechanical environment [49].

[2]The electrical feedback results are based on the work by Buters et al. [107], and are used with permission from the authors.

4.6 Conclusion

We have demonstrated that we can consistently fabricate nested trampoline devices with both high quality factor and high finesse. We design the devices to have 80 dB of mechanical isolation from the environment at the inner resonator frequnecy, and we observe greater than 45 dB of mechanical isolation at lower frequencies and the elimination of clampling losses. With our mechanical isolation we can investigate the internal losses of trampoline resonators (Chapter 5) and perform stronger optomechanical cooling, particularly at cryogenic temperatures (Chapter 8). These devices were also used for an investigation of optomechanically induced transparency (OMIT) [108].

Chapter 5

Internal Mechanical Quality Factor

In the previous chapter we developed a method for isolating mechanical modes from their substrate. However, mechanical energy and hence quantum information can still be lost within the mechanical resonator itself to a number of dissipation mechanisms. In this chapter we investigate three possible sources of intrinsic material dissipation in trampoline resonators, and we develop new device geometries which mitigate these loss sources.

5.1 Mechanical Dissipation in the Materials

The mechanical loss mechanisms within Si_3N_4 have been studied extensively [100, 109, 110, 69]. Within a one dimensional Si_3N_4 resonator the quality factor is given by [110]:

$$Q = \frac{W_{tension}}{W_{bend}} Q_0 \tag{5.1.1}$$

$$W_{tension} = \frac{1}{2}\sigma A \int \left(\frac{\partial u(x)}{\partial x}\right)^2 dx \tag{5.1.2}$$

$$W_{bend} = \frac{1}{2} E I_z \int \left(\frac{\partial^2 u(x)}{\partial x^2}\right)^2 dx \tag{5.1.3}$$

$u(x)$ is the displacement, Q_0 is the intrinsic quality factor unenhanced by the stress, σ is the stress and E is the Young's modulus. A is the cross-section area and I_z is the moment of inertia. $W_{tension}$ is the energy stored in the nitride including the stress and W_{bend} is the energy of bending in the nitride. These equations have also been generalized to two dimensions [69]. However, because the arms of trampoline resonators stretch almost entirely along the length, and the motion is uniform across the width, it is sufficient to consider the one dimensional equations above. All calculations in COMSOL are performed with the full two dimensional energies. In general $W_{tension}$ is larger than W_{bend} leading to an enhancement proportional to $\sqrt{\sigma/E}$. It is has been observed that tension and bending dominate over any surface dissipation effects [100, 109, 110, 69]. This means that there are three ways to increase the Q of Si_3N_4 devices: increasing the stress, decreasing the bending energy of the devices, and increasing Q_0.

The stress in the Si_3N_4 is determined by the low pressure chemical vapor deposition (LPCVD) process. Typically, this is limited to around a GPa, and for our fabrication process we start with wafers with Si_3N_4 stress in the range of 800 MPa to 1 GPa. The stress in Si_3N_4 nanostrings and trampolines can be increased by geometric stress engineering [111, 112]. However, applying these techniques to trampolines carrying a DBR load would dramatically lower their frequency, because we would require narrower trampoline arms. Therefore, increasing stress is a challenging way forward for improving the quality factor of our devices.

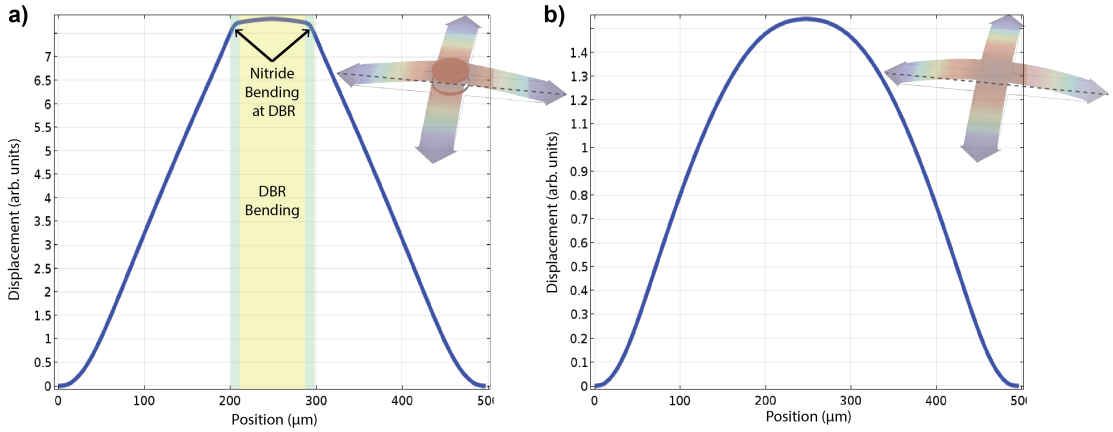

Figure 5.1: **Linecuts of trampoline resonator motion.** COMSOL simulations of the motion of trampoline resonators with **a)** and without **b)** a DBR mirror. The insets show the full mode, and the main figures show a line cut along the dotted line. There are two main regions where the DBR causes a difference in behavior: the green region where the silicon nitride bends much more sharply and the yellow region where the DBR mirror bends. Both types of resonators exhibit bending at the clamping point to the Si substrate.

Next we consider bending losses in Si_3N_4 trampolines. We can break the resonators into four regions: bulk Si_3N_4, the DBR mirror, the clamping point for the mirror and the clamping point to the Si substrate, as illustrated in Figure 5.1a. In contrast (Figure 5.1b), devices constructed solely from Si_3N_4 only contain two regions: bulk Si_3N_4 and clamping to the Si substrate. In bare Si_3N_4 devices, the losses tend to be dominated by the clamping points on the edges, because this is where the devices experience the most bending ($\partial^2 u/\partial x^2$ is large) [69, 110]. The easiest way to reduce bending losses is by using a thinner layer of nitride, such that there is less volume bending [111]. Because pure Si_3N_4 devices carry no load in addition to their own mass, the spring constant and effective mass decrease together and the frequency does not decrease. Recently these losses have been avoided with soft clamping of the devices with a phononic crystal made of Si_3N_4 [113]. In Section 5.3 we will describe our efforts to reduce the clamping losses to the Si and to the DBR by changing the geometry, and in Section 5.4 we will compare

the losses in trampoline resonators with and without a DBR mirror.

The final method to increase the Q factor of Si_3N_4 devices is to reduce the intrinsic losses. The exact mechanism for the losses in Si_3N_4 is still uncertain, but there is evidence to suggest it relates to coupling to two level systems [114, 115]. These systems gradually get frozen out at low temperatures leading to a reduction in the losses of the system [116, 117]. Most Si_3N_4 systems see an increase in the quality factor between room temperature and 4K [104, 118, 114, 119]. Recently, it has been shown that there is a second dramatic increase in the quality factor between 4K and 100 mK [120, 121]. Fortunately, low temperatures are advantageous for quantum optomechanics, so our devices could likely take advantage of this boost to the Q at low temperatures.

Our devices could also suffer from mechanical losses in the DBR mirror. As is shown in Figure 5.1a, there is some mechanical motion within the mirror itself, and COMSOL simulations determine that this accounts for 24% of the bending energy. Mechanical losses within SiO_2/Ta_2O_5 mirror coatings have been studied extensively in the last 20 years, because gravitational wave observatories use the same materials for their mirrors [60, 122, 123, 124, 125, 126]. Mechanical losses lead to thermal Brownian motion of the coatings, and these vibrations are a major contribution to the noise floor in the band between 50 and 500 Hz [124, 60]. The loss angle $\phi = 1/Q$ is typically between 0.5 and 3 x 10^{-4} for SiO_2 and between 2 and 6 x 10^{-4} for Ta_2O_5 [122, 123, 76, 126]. These loss angles are measured between 10 Hz and 10 kHz, but there is evidence to suggest that the loss angle has only weak dependence on frequency [126].

We can modify Equation 5.1.1 to include the bending losses of the DBR [126]:

$$Q = \frac{W_{tension}}{W_{SiN}/Q_0 + W_{DBR}\phi} \tag{5.1.4}$$

W_{SiN} is the nitride bending energy and W_{DBR} is the DBR bending energy, which can be

calculated using Equations 5.1.2 and 5.1.3. Note that even though the tension is only in the nitride layer, it still enhances the Q of the device, regardless of whether bending losses occur in the nitride or the DBR. We can estimate the limits to the quality factor by simulating the bending energies in COMSOL. If we assume no loss in the nitride and an average loss angle of 4 x 10^{-4} in the DBR stack we find a Q of 500,000. In Section 5.5 we develop trampoline resonators with reduced DBR bending in an attempt to surpass this limit to the Q.

5.2 Measuring Mechanical Q

There are two methods we use to measure mechanical Q: thermal noise spectra and ringdowns. We can measure the mechanical position continuously by locking to the side of a Fabry-Pérot resonance feature, where the transmitted intensity varies linearly with position. For any Q measurement, we must eliminate any optomechanical effects, which might increase or decrease the damping rate. Therefore, we use a cavity with low finesse in the range of 100-300. In Santa Barbara we shorten the cavity such that excess light diffracts around the small mirror. In Leiden we use a laser at about 980 nm where the coatings are less reflective. As a test to ensure optomechanical effects are absent we take thermal spectra or ringdowns with the laser locked to opposite side of the Fabry-Pérot resonance and verify that the Q is the same.

When a mechanical resonator is in equilibrium with its thermal environment, it moves according to the imaginary part of its susceptibility [8]:

$$S_{xx}(\omega) = \frac{2k_BT}{\omega}\mathrm{Im}\left[\chi(\omega)\right] = \frac{2k_BT}{\omega}\mathrm{Im}\left[\frac{1}{im_{eff}\omega\gamma + m_{eff}(\omega_m^2-\omega^2)}\right] \quad (5.2.1)$$

$$\approx \frac{k_BT\gamma}{2m_{eff}\omega_m^2\left(\gamma^2/4+(\omega_m-\omega)^2\right)} \quad (5.2.2)$$

This equation simplifies to a Lorentzian expression near the mechanical resonance ($\omega = \omega_m$) with a linewidth of γ. We can therefore measure the linewidth and Q by measuring the noise power spectral density $S_{xx}(\omega)$ and fitting a Lorentzian. Besides the simplicity of this method, another advantage is that if our measurement is calibrated, we can also extract the temperature of the mechanical resonator.

The thermal motion method works well when the system does not drift in frequency. However, when the frequency drifts it will make the linewidth appear artificially larger, and we take a ringdown measurement instead. We drive the system at the mechanical resonance frequency, using either the dielectric force from a metal tip (as discussed in Chapter 4) or the sinusoidal amplitude modulation of a laser beam. We then isolate the amplitude of motion with a lock-in amplifier at the mechanical resonance frequency, and measure the ringdown of this quadrature. This method is helpful for resonances with low frequency, high Q, or low temperature.

5.3 Changing Clamping Conditions

As a first attempt at improving the mechanical quality factor of these systems, we change the geometry of the Si_3N_4 arms, and in particular their direction of motion relative to the mirror. The trampoline resonators from Chapter 3 and 4 clamped perpendicularly to the Si and DBR mirror. We fabricate several geometries in which the clamping is parallel to the motion in an attempt to minimize bending.

The three geometries we compare are shown in Figure A.7. The best Q factors obtained for each geometry are shown in Table 5.1, and parameter fits for device geometry **a)** are shown in Figure 5.3. Despite the large changes to the geometry, there is not a significant impact on the Q of the devices, and we do not see a noticeable increase for the perpendicularly clamped geometries. We conclude that we will need a more compli-

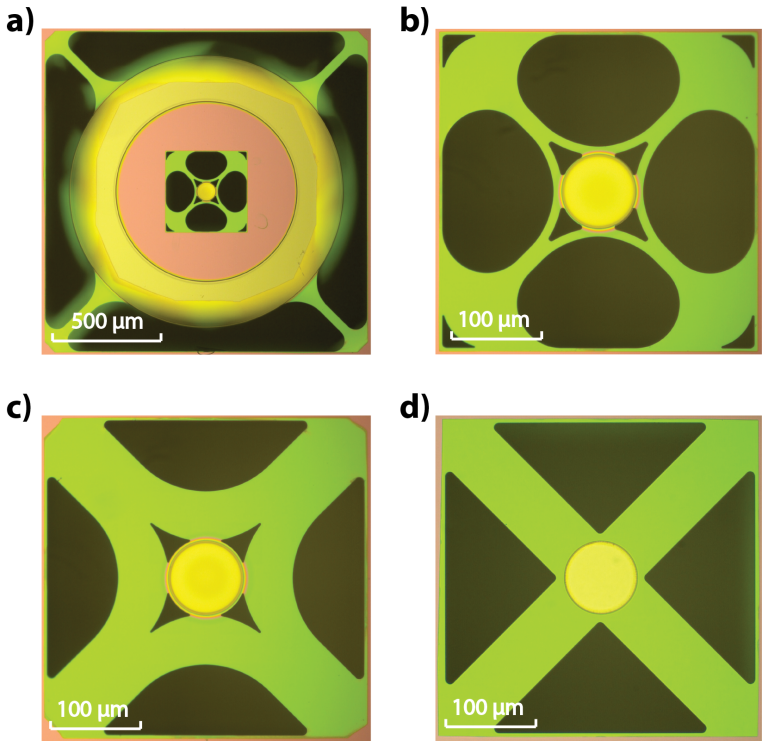

Figure 5.2: **Devices with different clamping geometries. a)** Optical microscope images of a full device including the outer resonator and **b)-d)** only the inner resonator with different clamping configurations. All devices were fabricated using the same process.

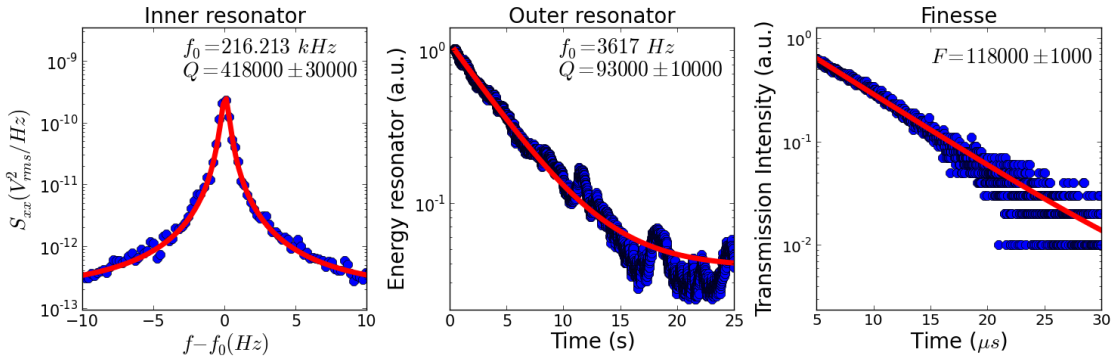

Figure 5.3: **Measurement of a clamping geometry. a)** A Lorentzian fit to the thermal motion determines inner resonator Q for the device shown in Figure A.7a,b. **b)** A ringdown measures the Q of the outer resonator, because of its low frequency. **c)** Finesse is measured via cavity ringdown. All devices in Table 5.1 were measured in this way.

Table 5.1: **Q for different clamping geometries**

Geometry	Frequency (kHz)	Q
b	216	418,000 ± 30,000
c	307	347,000 ± 18,000
d	293	419,000 ± 30,000

cated solution to increase the Q of these devices.

5.4 Comparison to Bare Trampolines

It is important to compare our results for trampolines with DBR mirrors to trampolines without to ensure that the presence of the DBR mirror and not some fabrication problem is responsible for the limited Q. We could fabricate devices with the same fabrication method explained in Chapter 4, starting from a chip without DBR layers and skipping the processing steps for those layers. However, the back of the chips we use has a layer of Si_3N_4 which matches the device layer on the front of the chips. In this section we fabricate an additional trampoline resonator on the back of the device, so that we can do a controlled comparison between front and back devices or DBR vs bare trampolines all in one integrated structure.

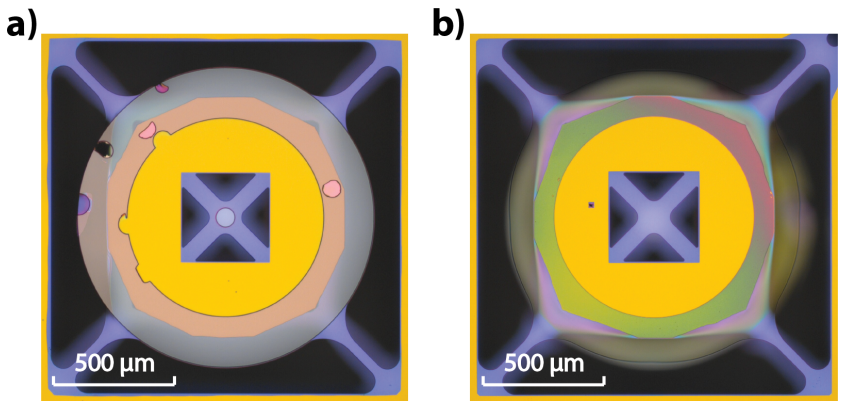

Figure 5.4: **A double sided trampoline resonator device. a)** The front side is a trampoline with a DBR mirror. The defects in the mirror ring do not affect the mechanical (or optical) properties of the device. **b)** The back side is a bare trampoline resonator. The purple haze surrounding each resonator is the defocused image of the resonator on the other side.

The fabrication for these structures is quite similar to those of the previous chapters. However, we begin the process by depositing about 1 µm of PECVD SiO_2 followed by about 300 nm of PECVD SiN on the back of the chip. This serves the same function as the protective mirror ring from Chapter 4, and adds to the validity of this as a control process. We first etch the DBR stack with an inductively coupled plasma (ICP) etch, followed by a CF_4 etch of the Si_3N_4 trampoline. We then flip the chip, and use IR contact lithography to align the back of the device to the front with approximately 10-20 µm accuracy. We etch the back with an ICP etch, followed by a CF_4 etch of the Si_3N_4 trampoline. At this point we etch approximately 400 µm down into the silicon wafer with a deep reactive ion etch (DRIE). We release both devices at once using a TMAH etch. Finally, without moving out of liquid, a thin protective layer of SiO_2 is removed from the devices with an HF dip, and the devices are transferred to ethanol, where they are dried on a hot plate. A device made with this process is shown in Figure 5.4.

We start by comparing the Q factors of the two devices. We take ringdown measurements, because the frequency of the bare membrane devices were observed to shift

down in frequency over time. The highest Q obtained for the bare membrane device is 1,310,000 ± 110,000 compared to 476,000 ± 67,000 for the DBR device. (The fQ product is about six times higher.) The bare membrane Q is still a little lower than is typical for membrane systems [67, 69], likely due to the fact that our devices are 450 nm thick instead of 50 nm thick. We would therefore like to test devices with thinner Si_3N_4 layers.

We thin out the devices using a directional CF_4 etch at the end of the fabrication process. This is also important for raising the finesse of the cavity with these devices, because a thick membrane can cause optical losses, as will be discussed in the next chapter. We observe a large increase of the quality factor of the bare nitride trampolines to a maximum of 2,800,000 ± 200,000 for a membrane thickness of 56 nm. We thinned the front device down to 170 nm, and the DBR trampoline Q only increased to 450,000 ± 30,000, which did not improve on the maximal Q. We can simulate the bending losses in the Si_3N_4 only devices and plug our results into Equation 5.1.1. With this analysis we determine that Q_0 is about 20,000, which is consistent with other results for stoichiometric Si_3N_4 [110]. If we apply Equation 5.1.1 to the DBR trampolines, and only assume losses in the nitride, we determine a limit to the quality factor of 800,000. This is strong evidence that Si_3N_4 intrinsic losses and the fabrication process are not limiting quality factor for devices with a DBR mirror.

Other groups have observed an increase in quality factor at cryogenic temperatures, and we would like to measure the effect of cooling on our trampoline resonators. In order to measure Q at cryogenic temperatures without the need to align an optical cavity we use an interferometric setup, shown in Figure 5.5. A fiber and an electrode with a narrow (~ 100 μm) tip are placed approximately 500 μm behind the device facing the bare trampoline side. The electrode can be used to drive the two resonators as described in Chapter 4. We send 1550 nm light into the fiber and use the interference between reflections from the device and the end of the fiber to measure the position of the device.

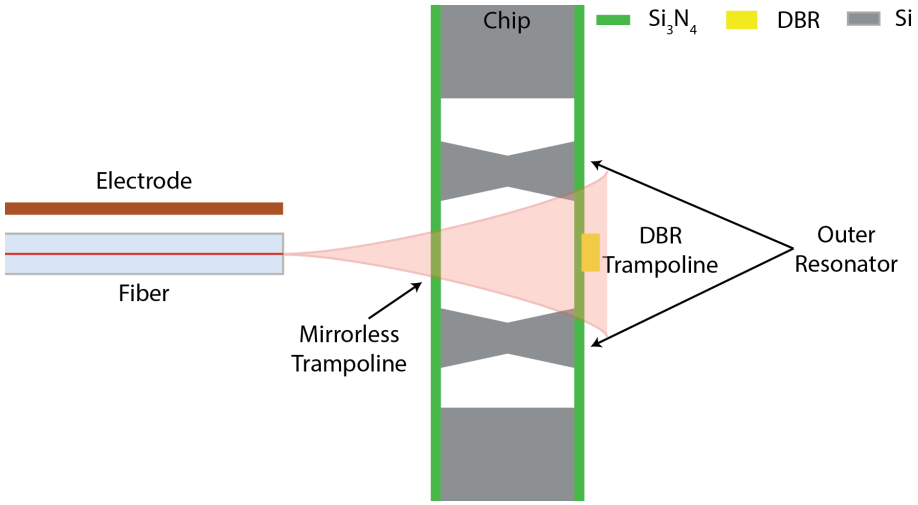

Figure 5.5: **The interferometer setup.** We can measure two resonators simultaneously by aligning a fiber parallel to both devices. We drive the two resonators by applying a voltage at the mechanical frequency to the electrode. We measure mechanical motion by looking at the fluctuations in the interference between the fiber face and the surface of the two resonators.

Table 5.2: **Q dependence on Temperature**

Temperature(K)	DBR Resonator Q	Bare Resonator Q
300	400,000 ± 50,000	2,700,000 ± 100,000
5	430,000 ± 30,000	5,700,000 ± 100,000
<0.5	380,000 ± 50,000	8,700,000 ± 200,000

We can measure both the bare trampoline and the DBR in this way, but it is only possible to measure Q via ringdown, because the sensitivity is insufficient to measure thermal motion at low temperatures.

The mechanical Q factors at three temperatures are shown in Table 5.2. At room temperature and 5K, the system is well thermalized to its surroundings. Figure 5.6 shows ringdowns for both types of resonators at 5K. However, when we cool the setup down to 50 mK, heating of the devices by the laser becomes significant. Interestingly, there is a strong dependence of the Q on the laser power used in the measurement. We attempt to use as little power as possible to perform the measurement, but we are limited by the sensitivity at low powers. It is unclear whether the heating is due to optical heating in the

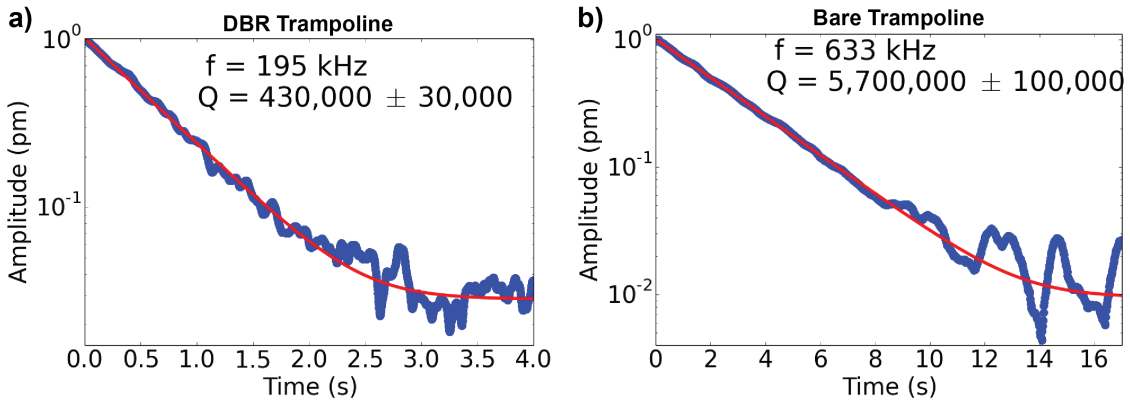

Figure 5.6: **Mechanical ringdowns of two trampoline resonators. a)** A ringdown with a DBR mirror and b) without a DBR mirror. The measurements are performed with an interferometer at a temperature of 5K.

Si_3N_4 layer or in the Si frame of the outer resonator. A more advanced setup might yield even higher Q's at mK temperatures. The Q of the DBR trampoline resonators remains relatively unaffected by the temperature, while the Q of the bare trampoline increases dramatically. At the lowest temperature, the fQ product of the bare membranes is approximately 40 times that of the DBR resonators.

In general, we see that the devices made purely of Si_3N_4 follow the same trends that have been observed in other Si_3N_4 optomechanical devices. The Q increases both for thinning the layer and for lowering the temperature. The Q factors we achieve fall into the range of what is typically observed for large square membranes [104, 67]. This is to be expected, because we did not optimize the geometry of the trampolines for a system with no load. Future steps could include making Si_3N_4 devices utilizing stress enhancement [111, 112] and/or soft clamping [113]. However, for devices with a DBR we can conclude that the intrinsic quality factor of the Si_3N_4 is not limiting. Furthermore, if the system were dominated by bending losses we would also expect the Q to go up at cryogenic temperatures, because Q_0 in Equation 5.1.1 has increased. This suggests that the DBR mirror trampolines are limited in Q by bending losses in the mirror layers.

5.5 A DBR Mirror on a Pedestal

Most evidence suggests that we must eliminate bending in the DBR mirror to raise the mechanical Q of our devices. We investigate different mirror geometries in COMSOL to find a solution. One possibility is extending the mirror to add flaps which counterbalance the mirror motion [98]. The downside of this approach is that it will tremendously increase the mode mass of the devices, making ground state cooling difficult. Alternatively, we can construct the “flaps" out of the mirror layer by undercutting the bottom layer. In this way, at a particular frequency of oscillation, the motion of the middle of the mirror is balanced by the free-floating mirror. COMSOL simulations predict that it should be possible to reduce the bending energy by at least a factor of 10 this way. The undercut geometry is shown schematically in Figure 5.7a.

We modify the fabrication process to produce DBR mirrors which are undercut or mounted on a pedestal. We start with the same layers as in previous chapters. When we etch away the DBR layer to make the mirror, we stop at the top of the bottom SiO_2 layer, which is a half-wave layer (366 nm). We proceed with patterning the front and back of the chip, as it was performed in previous chapters. Before the release, we coat the chip with a 200 nm layer of Cr to protect the other layers of the DBR from being etched. We found that this was not enough, however, so we also add a layer of resist. After removing the Cr from the regions surrounding the DBR we undercut the mirror by placing the sample in buffered HF for about 90 minutes. The radius of the pedestal depends on the etch time. We remove the resist and Cr and release the devices.

We measured thermal spectra for each resonator to determine the Q. We found that the Q factor for the pedestal devices was between 4000 and 15000, far lower than the Q of other devices, even broken ones. This must be caused by changes to the surface chemistry of the devices in either the HF etch or the Cr deposition or removal. Degradation of

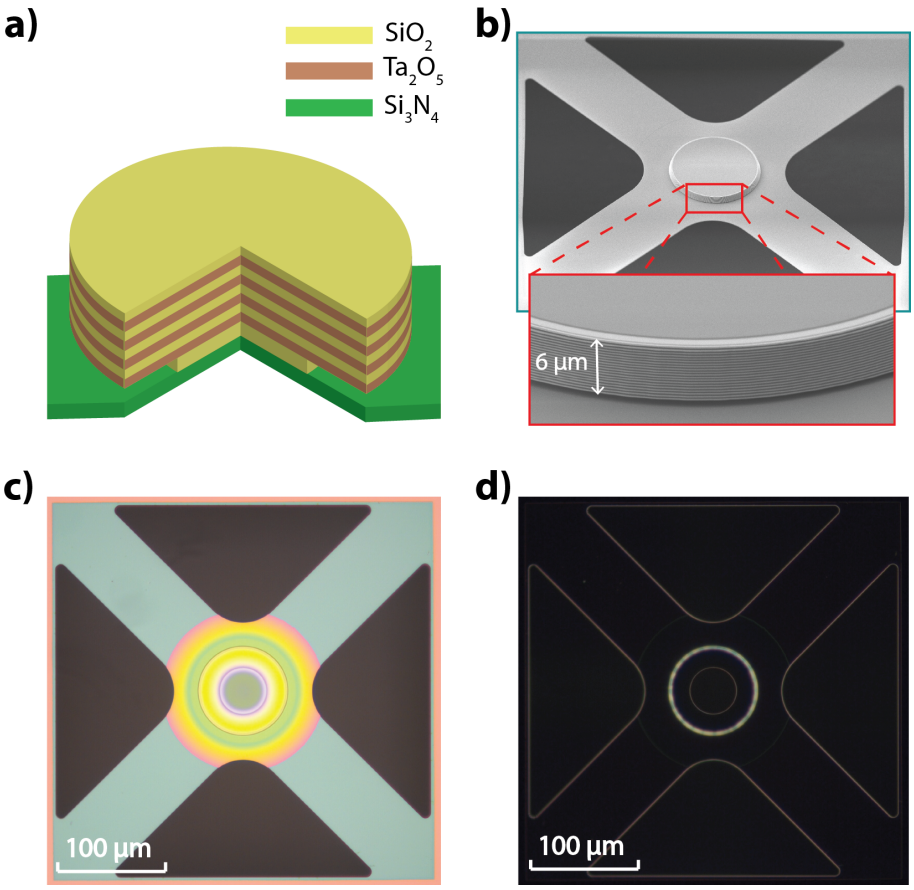

Figure 5.7: **Undercutting the DBR mirror. a)** A schematic of the undercut mirror with 9 layers instead of 40 for clarity. **b)** An SEM image of a trampoline resonator with an undercut DBR mirror. The inset shows the mirror layers which are perfectly intact and the gap at the bottom of the mirror. **c)** Optical bright field image. The pedestal is purple, and the rainbow colors are due to etching of the Si_3N_4 layer. **d)** Dark field image. The lines show edges, and the outline of the pedestal is visible in the center.

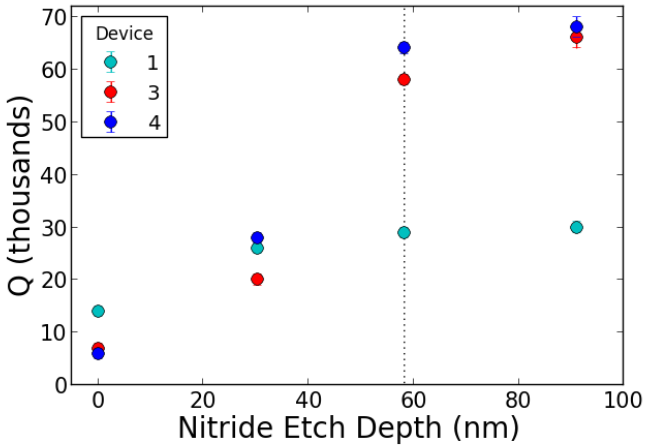

Figure 5.8: **Etching the Si_3N_4 of the pedestal resonator.** We etch away the top of the Si_3N_4 layer with a CF_4 etch to remove contamination from HF. The layer was 450 nm thick before the HF etch and 385 nm thick after (corresponding to 0 on the x axis.) The dashed vertical line is an estimate for the depth of contamination.

the Q in other stoichiometric Si_3N_4 systems has been observed during HF etching [127]. This is posited to be caused by surface contamination from the HF into the Si_3N_4. Our HF etch was long, so this is a likely explanation.

If hydrogen or fluorine diffusion is the problem in our system, the quality factor should improve if the surface layers are removed, particularly past the mean depth of diffusion. We test this by etching away the top surface of the device with a CF_4 etch, as was described in the last section. The results are shown in Figure 5.8. We can improve the quality factor by more than a factor of 10 using this method, but it does not return to the value of devices with no pedestal. This could be due to the fact that we cannot remove the HF contamination from under the mirror with the CF_4 etch. We attempted an H_3PO_4 etch to remove the contaminated Si_3N_4 layer under the mirror, but this did not improve the Q, possibly because it also has many hydrogen ions present. As of this writing, we do not have a solution for making pedestals using HF undercutting which does not damage stoichiometric Si_3N_4.

There are a few possibilities for eliminating bending losses in the DBR which could

be tried in the future. The first is to extend the mirror and create flaps, which counterbalance, and prevent motion of the mirror [98]. This will lower the frequency of the devices, but might increase their quality factor. Another solution is to change the composition of the DBR layer stack. There have been promising results with Ti doped Ta_2O_5, which reduce both the optical absorption and the mechanical loss angle, but this is a small difference [75]. A more drastic change would be to switch to GaAs/AlGaAs DBR mirror which have a loss angle of 2.5 x 10^{-5}, a significant improvement, but these coatings suffer from high optical absorption of 12.5 ppm [128].

5.6 Conclusion

We have examined in detail the many different loss contributions to trampoline resonators. Interestingly, we found that there are two loss mechanisms which are of the same order of magnitude: bending losses in the Si_3N_4 and DBR bending. Unfortunately, to improve nitride bending, it is beneficial to have a smoother transition between the nitride and the DBR, so that the mechanical impedance mismatch does not cause a sharp corner in the mode. Conversely, to improve DBR bending, it is better to have a weak clamping between the mirror and the nitride, so that there is a large mechanical impedance mismatch. These conflicting design goals make the prospects for improvements of DBR mirrors on Si_3N_4 membranes difficult.

Despite challenges in raising the Q, we have fabricated a series of devices which are already useful for experiments with macroscopic optomechanics. The double sided device geometry developed in this chapter is a useful prototype for future experiments involving state swapping and entanglement between different types of resonators. These results will be discussed in the next two chapters. Our devices are well in the sideband resolved regime, so that efficient optical cooling towards the quantum regime is possible

as we will discuss in Chapter 8. Finally, the high finesse cavities we built could also be used for efficient state transfer between mechanical resonators.

Chapter 6

State Transfer between Disparate Resonators

Systems of coupled mechanical resonators are useful for quantum information processing and fundamental tests of physics. Direct coupling is only possible with resonators of very similar frequency, but by using an intermediary optical mode, nondegenerate modes can interact and be independently controlled in a single optical cavity. In this chapter we demonstrate coherent optomechanical state swapping between two spatially and frequency separated resonators with a mass ratio of 4. We find that, by using two laser beams far detuned from an optical cavity resonance, efficient state transfer is possible. Although the demonstration is classical, the same technique can be used to generate entanglement between oscillators in the quantum regime. [1]

[1] The contents of this chapter are based on the work by Weaver et al. [129], and are used with permission from the authors.

6.1 Introduction

Hybrid quantum systems have been developed with various mechanical, optical and microwave harmonic oscillators [47, 130, 7, 131, 8, 78]. The coupling produces a rich library of interactions including two mode squeezing [132, 133, 134, 135], swapping interactions [47, 7, 46, 136], back-action evasion [137, 138] and thermal control [139, 140, 141]. In a multimode mechanical system, coupling resonators of different scales (both in frequency and mass) leverages the advantages of each resonance. For example: a high frequency, easily manipulated resonator could be entangled with a low frequency massive object for tests of gravitational decoherence [20, 19, 51]. Through a process similar to STIRAP (Stimulated Raman Adiabatic Passage) [142] in atomic physics it is possible to couple two very different mechanical resonators with an effective beam splitter interaction. We investigate this interaction, and demonstrate efficient and coherent state transfer between two frequency separated mechanical resonators in the same cavity.

Efforts are under way to control systems with several mechanical modes at the quantum level [130, 73, 143]. Hybridization and coherent swapping have been observed in optomechanical [136, 143, 144] and electromechanical [145, 146, 147] systems with nearly degenerate modes. Because the interaction between two coupled resonators decreases dramatically with frequency separation, either precise fabrication or frequency tuning is required to ensure degenerate mechanical modes. In many of these systems a separate optical cavity is necessary to control the motion of each mechanical resonator, which leads to complicated systems.[136, 147] Dynamically coupling non-degenerate resonances together in a single cavity avoids these technical difficulties, while still allowing for individual control of each resonance. In an optomechanical system where mechanical resonances are spaced further apart than the optical cavity linewidth, each

resonance can be addressed independently with a laser detuned to that mechanical resonance frequency.

Here we investigate the real time dynamics of a coupled mode system and show coherent optomechanical state swapping between two mechanical modes. High swapping efficiency is possible in a region with large beam detuning from the cavity resonance. We discuss implementation of this method in the quantum regime and some capabilities of interacting quantum systems with large frequency separation.

6.2 Results

6.2.1 Optomechanical System

Our optomechanical system consists of a room temperature Fabry-Pérot cavity with one fixed end mirror, one moving end mirror on a trampoline (resonator 1) and one trampoline membrane (resonator 2)[112, 111, 66] inside the cavity as shown in Figure 6.1. The radiation pressure force on the resonators from photons in the cavity and the position dependent cavity phase shift mediate an interaction between the two resonators and the optical cavity [8]. The resonator frequencies are $\omega_1/2\pi$ = 297 kHz for the end mirror and $\omega_2/2\pi$ = 659 kHz for the membrane and the optical decay rate of the cavity is $\kappa/2\pi$ = 200 kHz, so the system is in the resolved sideband regime.

6.2.2 Optomechanical Swapping

We couple the two nondegenerate modes by modulating the inter-resonator coupling coefficient between resonators 1 and 2 at their difference frequency. Buchmann and Stamper-Kurn [148] found that an equivalent effect is produced by injecting two laser beams separated by the mechanical difference frequency into an optomechanical

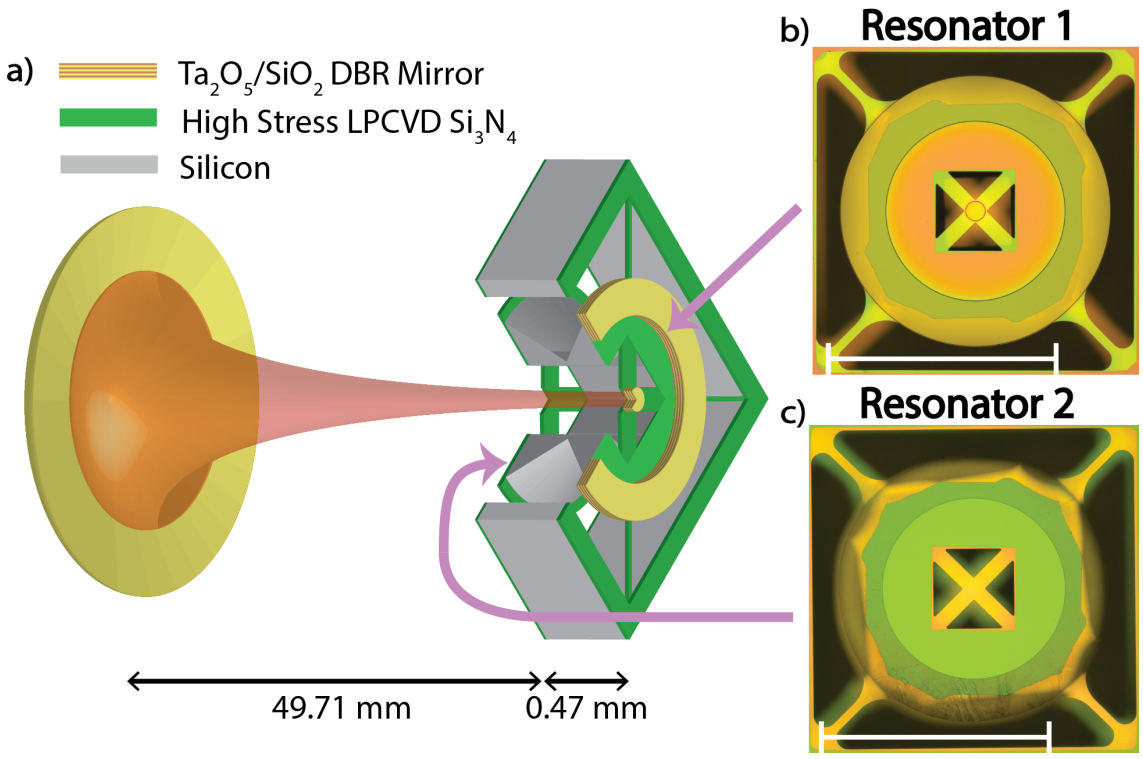

Figure 6.1: **Optomechanical setup with two resonators in an optical cavity. a)** A schematic diagram of the optical cavity with two mechanical trampoline resonators. The resonators are constructed from Low Pressure Chemical Vapour Deposition (LPCVD) Silicon Nitride. One resonator has a distributed bragg reflector (DBR) mirror (**b**) and one resonator is a bare membrane (**c**). **b)** and **c)** are optical microscope images of the two resonators, with 1 mm scale bars. The resonators are suspended from a shared outer resonator to provide mechanical isolation from the environment. This figure is not to scale.

cavity. In the microwave regime it has been shown that driving with two tones leads to an avoided crossing of the mechanical energy levels of two resonators with different frequencies [73, 149]. Here, a single laser beam detuned from cavity resonance by the mechanical frequency of one resonator swaps excitations between that resonator mode and the optical cavity mode [150]. A second laser beam detuned by the other mechanical frequency will concurrently swap excitations of the other resonator with the optical mode, resulting in a net swapping between the two mechanical modes. A schematic diagram of the exchange operation and the effective Λ-type system produced is shown in Figure 6.2. This interaction can be described by the beam splitter Hamiltonian [148]:

$$H_{int} = \frac{J}{2}\left(b_1^\dagger b_2 + b_1 b_2^\dagger\right) \tag{6.2.1}$$

J is the optomechanical swapping rate, and b_j is the annihilation operator for the jth mechanical mode.

To investigate this interaction we prepare one resonator in an excited state and then observe the swapping dynamics of the coupled system. We excite resonator 2 into a large coherent state by applying a voltage at its resonance frequency to an electrode behind the sample and then turn on the two laser beams. Figure 6.3 shows the measured amplitude of motion of the two resonators. We observe in real time as the mechanical excitation is swapped back and forth between the two resonators in a repeatable fashion. Figure 6.3b shows the response to a single optical swapping interaction. The operation can be modelled as an underdamped exchange between two coupled harmonic oscillators, and the fits indicate that our system operates in this regime (see Section 6.4.4.) The motion dips down to the thermal fluctuation level every time the state is exchanged, indicating complete state swapping. We now investigate the efficiency of the system and its coupling to different loss baths.

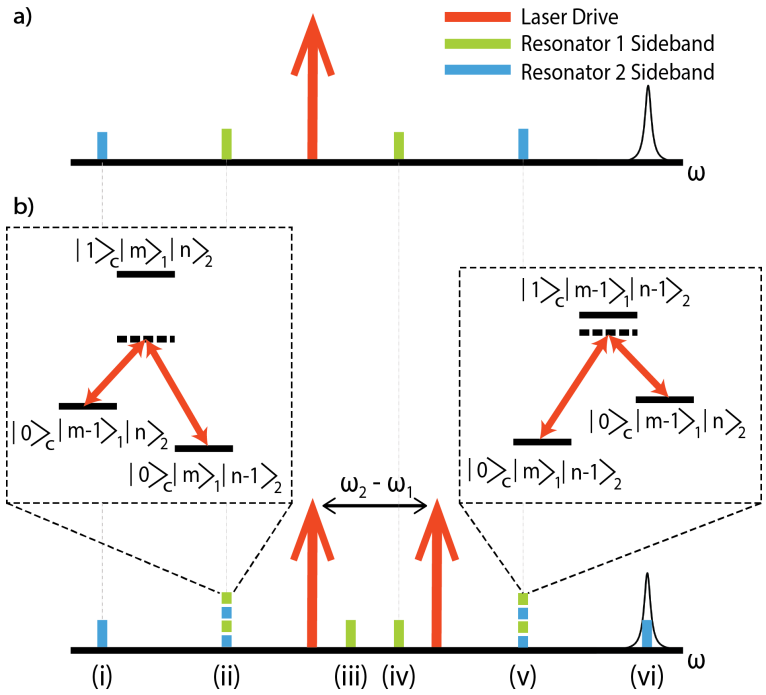

Figure 6.2: **Generating coupling between two resonators with two laser drives. a)** A single laser drive (red arrow) sent into the cavity produces four sidebands, two for each resonator. The laser is detuned from a cavity resonance on the right. **b)** A second laser can be added to generate optical swapping. (ii) and (v) are overlapping sidebands of the two resonators. The insets indicate the analogy to state transfer in an atomic Λ-type system. The quantum number states are the photon occupation of the cavity, phonon occupation of resonator 1 and phonon occupation of resonator 2. Detuning from the intermediary state avoids losses due to light leaking out of the cavity. (iii) and (iv) are the unmatched sidebands of resonator 1 and (i) and (vi) are the unmatched sidebands of resonator 2. By adjusting the laser detuning, the sidebands (i-vi) can be separately aligned with the cavity resonance to interact with one resonator at a time or both at once. In the case shown here, the state of resonator 2 is swapped with the cavity, because sideband (vi) is aligned to the cavity. This figure is not to scale.

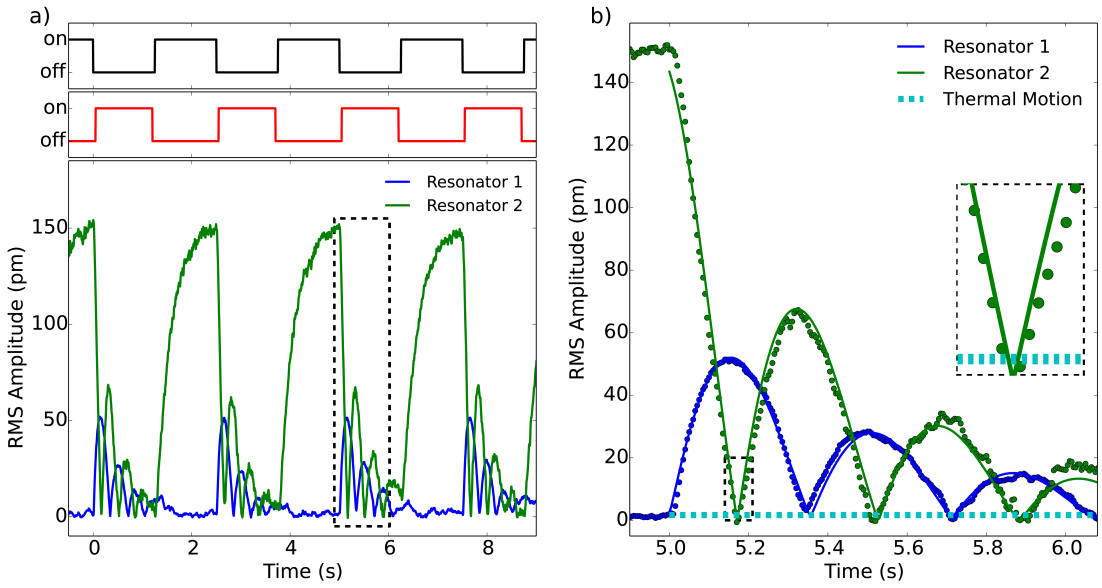

Figure 6.3: **Optomechanical swapping between mechanical resonators. a)** We alternate turning on a mechanical drive (black) and an optical swapping field (red), while continuously measuring the root mean square (RMS) amplitude of motion of the two resonators. This single shot measurement shows the repeatable dynamics of the system. **b)** A single swapping interaction (the dashed box in **a**) shows phonon Rabi oscillations. Solid lines are fits to the measured data points, and the dotted line indicates the thermal motion of the two resonators. Because the motion dips down to the thermal noise level every period, there is complete state swapping. The inset shows one such dip after a single complete state transfer.

6.2.3 Power and Detuning Dependence of Swapping Parameters

If the transfer rate, J, is much slower than the mechanical frequencies, the classical amplitudes of the modes b_1 and b_2 evolve slowly. Under this approximation the transfer rate, J, and total loss rate Γ are given by:

$$J = 2g_1 g_2 \sqrt{n_1 n_2}\left(\frac{\bar{\omega}-\bar{\Delta}}{\kappa^2/4+(\bar{\omega}-\bar{\Delta})^2}-\frac{\bar{\omega}+\bar{\Delta}}{\kappa^2/4+(\bar{\omega}+\bar{\Delta})^2}\right) \tag{6.2.2}$$

$$\Gamma = \sum_{i,j=1,2}\frac{n_i g_j^2 \kappa}{\kappa^2/4+(\Delta_i-\omega_j)^2}-\frac{n_i g_j^2 \kappa}{\kappa^2/4+(\Delta_i+\omega_j)^2}+\frac{\gamma_j}{2} \tag{6.2.3}$$

$$n_i = \frac{P_{in}}{2\hbar\omega_{Li}}\frac{\kappa_{ex}}{\kappa^2/4+\Delta_i^2} \tag{6.2.4}$$

g_j, ω_j and γ_j are the single photon optomechanical coupling rate, mechanical frequency and mechanical damping rate of the jth mode. Δ_i and n_i are the detuning to the red side and cavity photon number of the ith cavity mode. $\bar{\Delta}$ and $\bar{\omega}$ are the mean detuning and mean frequency of the two modes. ω_{Li} is the laser frequency of the ith beam, κ_{ex} is the input coupling rate and P_{in} is the input optical power. The swapping rate, J, is the sum of two Fano-like resonances from each set of matched sidebands. These exchange the mechanical state through a virtual state near the optical cavity resonance as pictured in the two insets in Figure 6.2b. The Lorentzian resonances in the expression of the loss rate, Γ, are the optically induced loss or gain of the jth mode due to the ith laser beam. There is one term for each of the eight sidebands (Figure 6.2a and b). The complete model is given in the Section 6.4.4.

Both optomechanical gain and loss should be avoided, as gain can introduce noise into the system. Because Γ decreases more quickly than J with increasing $\bar{\Delta}$, the ideal detuning is on the red side of the cavity, far from all resonances, in a region with negligible optomechanical amplification. Figure 6.4 shows an exploration of state swapping in a region with large detuning. The range is limited to regions of coherent swapping,

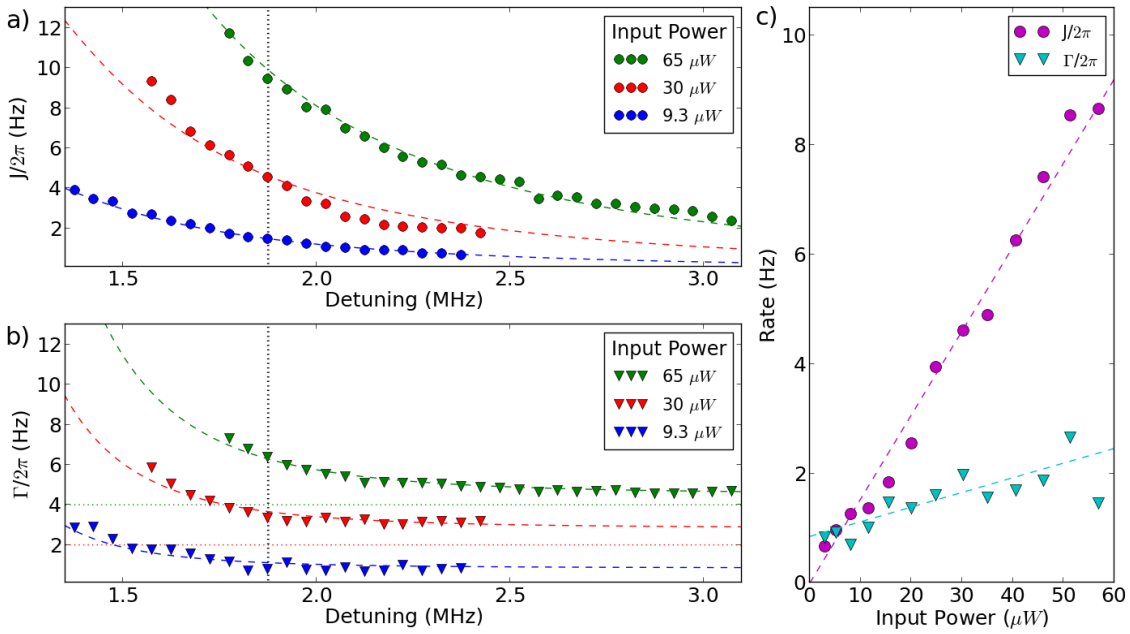

Figure 6.4: **Parameter dependence of optomechanical swapping rate and total loss rate.** Optomechanical swapping rate, J (**a**), and total loss rate, Γ (**b**), are measured as a function of detuning ($\bar{\Delta}/2\pi$). The dashed lines are two parameter fits based on Equations 6.2.2 and 6.2.3. For clarity the higher power measurements of Γ are vertically offset by 2 and 4 Hz as indicated by the dotted lines. **c)** J and Γ are measured as a function of input power at a detuning of 1.87 MHz (indicated by black dotted line in **a)** and **b)**.) The dashed lines are two parameter fits based on Equations 6.2.2 and 6.2.3. The ratio between the measured optical power and the input power P_{in} and the mean bare mechanical dissipation rate $(\gamma_1+\gamma_2)/2$ are the fitting parameters (see Section 6.4.3.) Statistical uncertainties are smaller than the point size.

where J>Γ. We observe the expected dependencies on detuning and input power for the coupling and loss rates. For smaller detunings the dominant loss is residual optical cooling of resonator 2, a by-product of its unmatched red sideband. For large detunings mechanical leakage to the environment dominates, and the peak efficiency is in the middle at $\bar{\Delta}/2\pi$ = 2.3 MHz.

6.3 Discussion

Two useful operations in a quantum network of oscillators are a complete state transfer (π-pulse) and a partial state transfer ($\pi/2$-pulse) to generate an entangled state. If we terminate the swapping after one of these pulses, 58% of the phonon occupation is conserved in a π-pulse and 77% of the occupation is conserved in a $\pi/2$-pulse (see Section 6.4.4.) The swapping rate demonstrated here at room temperature is not sufficient to overcome the large thermal decoherence rate ($n_{th}\gamma$) from the environment even at millikelvin temperatures. However, both the efficiency of transfer and the swapping rate could be improved significantly by decreasing the cavity loss. The finesse of our cavity is currently limited by absorption in the membrane trampoline, and we estimate that using a thinner membrane would improve the finesse by at least a factor of four. Most of the detunings close to the cavity resonance are in the overdamped regime, where energy transfer is only possible with large losses. With an increased finesse, a point close to the cavity resonance appears where the positive and negative components of Γ cancel, leading to nearly lossless classical state transfer (>99% efficiency). In the quantum regime, the negative component of Γ introduces extra decoherence, so the quantum state transfer is more limited (56% efficiency). However, the effects of coherent swapping should still be visible (see Section 6.4.4.)

Although we have focused on swapping states between the fundamental modes of two resonators, the technique is general and can also be applied to higher order modes of the same resonator. We apply the exact same scheme to swap energy between the fundamental ($\omega_1/2\pi$ = 659 kHz) and the first excited ($\omega_2/2\pi$ = 1199 kHz) mode of the membrane trampoline as shown in Figure 6.5. Sequential swapping pulses between many mechanical modes in a cavity could generate a large network of coupled modes. Each mode is individually addressable because of its frequency separation from the other

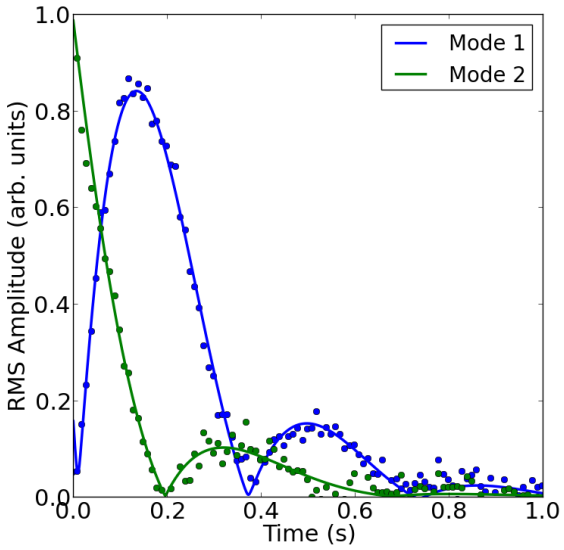

Figure 6.5: **Coherent optomechanical swapping between two membrane modes.** The same experimental procedure from the main text is repeated with two mechanical modes of the resonator without the mirror. The system parameters for this plot are: $\omega_1/2\pi$ = 660 kHz, $\omega_2/2\pi$ = 1199 kHz and $\Delta/2\pi$ = 2.7 MHz. The solid lines are fits to the measured data points for each mode. Full coherent optomechanical swapping is also possible using only a membrane in the middle setup.

modes. Low frequency resonators with long mechanical lifetimes could serve as storage for quantum information generated with a high frequency resonator.

This technique can also be used to study quantum mechanics in a high-mass system. Larger systems tend to suffer from small optomechanical coupling rates and slow interactions. We can instead prepare a quantum superposition state in a high frequency resonator with large optomechanical coupling and transfer it into the high-mass resonator. After letting the system evolve for an extended period, then transferring the motion back to the high frequency resonator, we can determine if the state decohered. Finally, this work could be extended to provide directional adiabatic transfer of states with STIRAP by using separate time-varying intensity pulses for the two input laser beams [142].

6.4 Methods

6.4.1 Optomechanical System

The optomechanical system is an extension of previous systems [87]. We use a Fabry-PÃľrot cavity with one fixed end mirror with a nominal radius of curvature of 50 mm. The other side of the cavity is formed by two trampolines fabricated on opposite sides of a tethered silicon block (see Figure 6.1.) The block acts as a mechanical low pass filter and provides greater than 65 dB of vibration isolation from the environment [89]. The cavity alignment uses the same technique used for single trampoline resonators [87]. Four piezo motors adjust the cavity in-coupling and three motors align the cavity itself. The DBR mirror on the trampoline is only 75 μm in diameter, so we align the beam waist of the cavity mode close to the DBR to avoid clipping losses. Mode calculations indicate that the beam radius should be approximately 16 μm at both the DBR and bare membrane trampoline. Based on the free spectral range of the cavity we estimate an exact length of 50.18 mm. The cavity is slightly longer than 50 mm because the mismatch in stress between the silicon nitride and the DBR mirror leads a slight inward curvature with a radius of approximately 1.5 mm [80]. Because the two resonators are fabricated on the same chip, no extra alignment is needed for the additional membrane trampoline in the middle. This technique could be extended to even more resonators by attaching multiple chips together.

The system behaves as the sum of its two constituent parts: a traditional optomechanical cavity with a single moving end mirror and a membrane in the middle system [66]. A membrane in the middle system has a finesse which depends on the position of the membrane with respect to the nodes of the cavity [72, 67]. Supplementary Figure 6.6a shows a periodic finesse response as we vary the node position by changing wavelength. The optical cavity loss is dominated by absorption in the membrane trampoline.

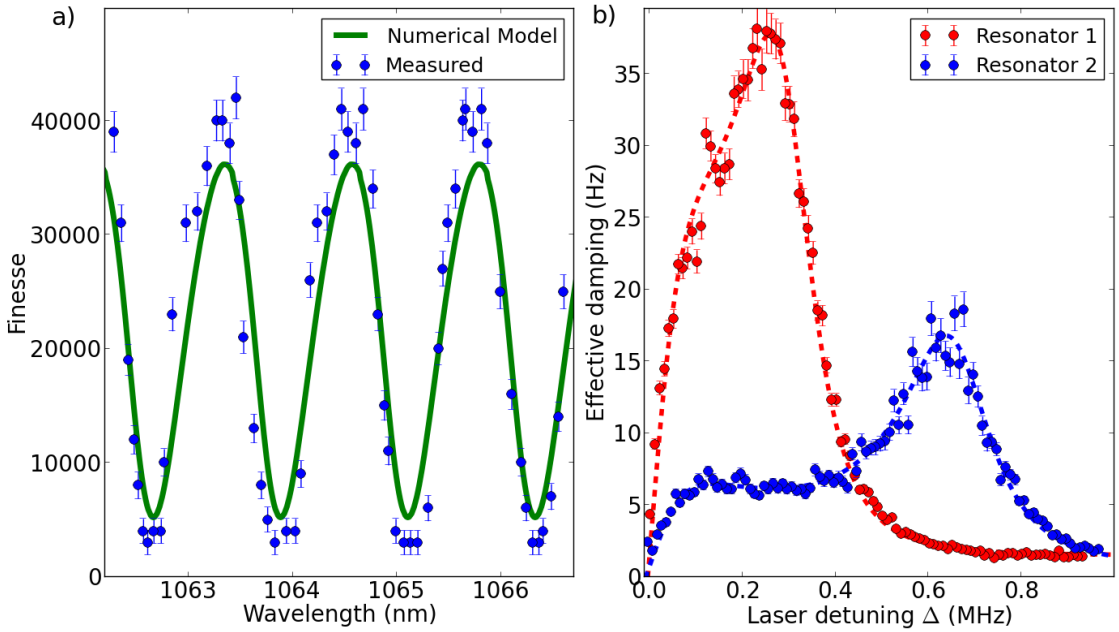

Figure 6.6: **Characterization of the hybrid membrane and moving end mirror cavity. a)** Finesse is measured as a function of laser wavelength. Periodic variations in finesse are expected of a membrane in the middle system. The solid line is a numerical model using the transfer matrix method and two adjustable parameters, the imaginary index of the nitride film, n_{im}, and the thickness of the chip, t. **b)** We change the detuning of a single laser beam and measure the optical damping of each resonator independently. The dotted lines are fits to the theory of a single resonator, indicating that the hybrid system behaves as the sum of two linear optomechanical systems. Note that the separation of the two peaks shows that each resonator can be controlled independently. Error bars in **a)** reflect the standard deviation of statistical fluctuations between ten measurements and in **b)** indicate the deviations from a fit for the linewidth of each resonator.

We numerically model the system with the transfer matrix method [70] and extract the imaginary refractive index (n_{im} = 3.2 x 10^{-5}) of the Si_3N_4 membrane and the chip thickness (470 μm.) Both values match expectations [72]. The nitride we use is about 10 times thicker than many other membrane in the middle setups [131, 112, 111, 66], so we can likely reduce optical losses with a thinner membrane. We have achieved finesses up to 180,000 in the same setup without the membrane present [89].

We also investigate the optomechanics of each individual mode. Supplementary Figure 6.6b shows the optical damping of each resonator as a function of detuning. The damping can be modelled perfectly using the linear optomechanical Hamiltonian for a single resonator,5 indicating that with a single laser beam the modes can be treated independently. From these measurements and others, we extract the optical decay rate, $\kappa/2\pi = 200 \pm 10$ kHz, the mechanical frequencies $\omega_1/2\pi = 297$ kHz and $\omega_2/2\pi = 659$ kHz, the mechanical damping rates $\gamma_1/2\pi = 1.5 \pm 0.1$ Hz and $\gamma_2/2\pi = 1.0 \pm 0.1$ Hz, and the single photon optomechanical coupling rates $g_1/2\pi = 0.9 \pm 0.1$ Hz and $g_2/2\pi = 1.3 \pm 0.1$ Hz. From finite element analysis simulations we determine that the effective masses are approximately m_1 = 150 ng and m_2 = 40 ng.

6.4.2 Fabrication

The fabrication process is a slight modification of the procedure for nested trampoline resonators [89]. We summarize here: 450 nm of LPCVD (Low Pressure Chemical Vapour Deposition) high stress silicon nitride is deposited on both sides of a silicon wafer, followed by a commercial SiO_2/Ta_2O_5 DBR mirror on the front and a SiO_2/SiN layer on the back. The mirror is etched with inductively coupled plasma (ICP) CHF_3 into disks for the cavity end mirror and a protective ring. The back SiO_2/SiN films are etched with CHF_3 ICP into a protective ring. The silicon nitride layers on both sides are

then etched with CF_4 to produce the front and back side trampolines. The silicon underneath the devices is removed with a deep reactive ion etch, followed by an etch in TMAH (Tetramethylammonium Hydroxide) solution. The devices are dipped in buffered HF to remove the top protective layer of SiO_2 from the mirror.

6.4.3 Experimental Procedure

We now turn to the generation of optomechanical state swapping. We use a two laser scheme as depicted in Supplementary Figure 6.7. One laser is locked to the cavity resonance with the Pound-Drever-Hall technique [151] using an avalanche photo diode as a detector, and the error signal is sent to two lock-in amplifiers, each of which monitors one mechanical frequency and extracts the amplitude of motion of the corresponding resonator. Before the swapping experiment shown in Figure 6.3 is performed, we calibrate the mechanical motion of the devices by measuring the thermal motion for approximately one minute. The optomechanical gain rate is less than 20% of the mechanical damping rate, and hence we do not expect or observe notable contributions to the noise from optomechanics. Another laser is passed through an acousto-optic modulator (AOM) with an RF drive that we modulate fully at half the mechanical difference frequency. The first order diffracted mode contains the two frequencies that we use to drive optomechanical swapping in the cavity. We have verified that the carrier frequency is completely suppressed and that higher harmonics are insignificant with cavity transmission measurements. We can't measure the optical input power directly, so we split off some power before the cavity to measure. Finally, a ring electrode behind the outer resonator is used to excite the motion of the trampoline resonators using the dielectric force from the gradient of the electric field [107].

We repeat this experiment for many powers and detunings, and extract the swap-

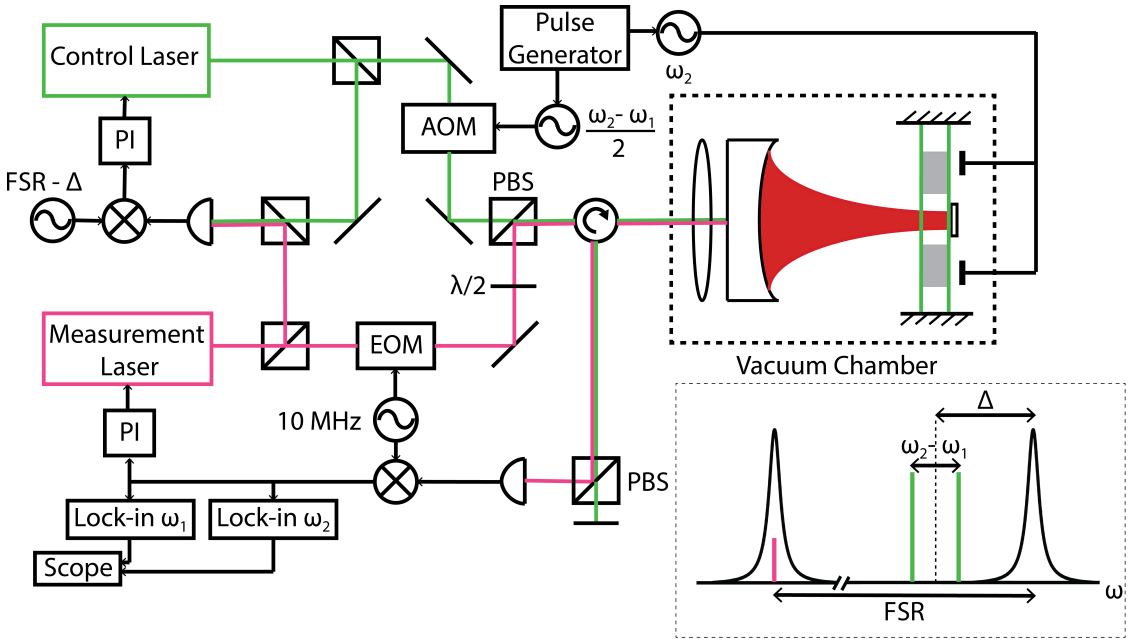

Figure 6.7: **Complete experimental setup.** One measurement laser is locked to the optomechanical cavity, and used to read out the motion of the two resonators. A second control laser is locked to the first laser approximately one free spectral range (FSR) away, and the frequency separation is tuned to control the detuning, Δ. An acousto-optic modulator (AOM) generates the two laser tones at the mechanical difference frequency (ω_2-ω_1.) A pulse generator controls two function generators connected to the AOM and a ring electrode, which drives resonator 2 using the dielectric force. Other abbreviations are: electro-optic modulator (EOM), proportion integral feedback controller (PI) and polarizing beam splitter (PBS). The inset (bottom right) shows the frequencies of the measurement laser beam (pink) and control laser beam (green) input to the cavity relative to its optical resonances.

ping rate and loss rate for each instance. The unmatched sidebands in Figure 6.2b produce loss, but they also shift the frequencies of the two mechanical resonances. Therefore, when performing the detuning and power sweeps shown in Figure 6.4 the spacing between the two laser beams must be continuously adjusted to match the mechanical difference frequency. The readout laser can optomechanically decrease or increase the bare mechanical linewidths of the resonators a small amount depending on the lock settings. We therefore fit the mean bare mechanical linewidth and the ratio between the measured optical power and the input power for every sweep shown in Figure 6.4. We also perform a swapping experiment using the two lowest order modes of the membrane trampoline to verify that the exact same scheme works for a single membrane in the middle. The swapping is shown in Figure 6.5.

6.4.4 Two-Tone Swapping Theory

Because the experiment performed here is entirely classical we limit ourselves to the classical optomechanical equations of motion following a similar path to Shkarin et. al [143] However, the results can be generalized to the quantum regime [148]. The linearized equations of motion for the cavity field fluctuations, a, and mechanical displacements, b_1 and b_2, are given by:

$$\begin{aligned} \dot{a} = &- \left(\frac{\kappa}{2} + i\omega_c\right) a + \sum_j i \frac{g_j a}{x_{zpm}} (b_j + b_j^*) \\ &+ \sqrt{\kappa_{ex}} \left(a_{in1} e^{-i(\omega_c+\Delta_1)t} + a_{in2} e^{-i(\omega_c+\Delta_2)t}\right) \end{aligned} \tag{6.4.1}$$

$$\dot{b}_j = - \left(\frac{\gamma}{2} + i\omega_j\right) b_j + i g_j a^* a \tag{6.4.2}$$

After some algebraic manipulation we arrive at the following equations for the adiabatic time evolution of the amplitude of the two resonators:

$$\dot{b}_1 = \left(-\frac{\gamma_{1tot}}{2} + i\delta\omega_1\right) b_1 + \left(-\frac{\gamma_{12}}{2} + i\frac{\tilde{J}}{2}\right) b_2 \tag{6.4.3}$$

$$\dot{b}_2 = \left(-\frac{\gamma_{2tot}}{2} + i\delta\omega_2\right) b_2 + \left(-\frac{\gamma_{12}}{2} + i\frac{\tilde{J}}{2}\right) b_1 \tag{6.4.4}$$

$$\gamma_{jtot} = \gamma_j + \sum_{i=1,2} \frac{2n_i g_j^2 \kappa}{\kappa^2/4 + (\delta_i - \omega_j)^2} - \frac{2n_i g_j^2 \kappa}{\kappa^2/4 + (\delta_i + \omega_j)^2} \tag{6.4.5}$$

$$\delta\omega_j = \sum_{i=1,2} \frac{n_i g_j^2 (\Delta_i - \omega_j)}{\kappa^2/4 + (\Delta_i - \omega_j)^2} - \frac{n_i g_j^2 (\Delta_i + \omega_j)}{\kappa^2/4 + (\Delta_i + \omega_j)^2} \tag{6.4.6}$$

$$\tilde{J} = 2g_1 g_2 \sqrt{n_1 n_2} \left(\frac{\bar{\omega} - \bar{\Delta}}{\kappa^2/4 + (\bar{\omega} - \bar{\Delta})^2} - \frac{\bar{\omega} + \bar{\Delta}}{\kappa^2/4 + (\bar{\omega} + \bar{\Delta})^2} \right) \tag{6.4.7}$$

$$\gamma_{12} = g_1 g_2 \sqrt{n_1 n_2} \left(\frac{\kappa}{\kappa^2/4 + (\bar{\omega} - \bar{\Delta})^2} - \frac{\kappa}{\kappa^2/4 + (\bar{\omega} + \bar{\Delta})^2} \right) \tag{6.4.8}$$

Although these equations look complex, they can be matched up term for term with the effects of each sideband. γ_{jtot} and $\delta\omega_j$ are the optical damping and optically induced frequency shift on the jth resonator due to the ith beam in the cavity. There are eight of these terms total, one for both sidebands on both lasers from both resonators. $\tilde{J}$ and γ_{12} are the bare optomechanical transfer rate and the loss induced decrease in the transfer rate. The first term in $\tilde{J}$ is produced as the net effect of two optomechanical swapping interactions with the cavity as depicted in the right inset of Figure 6.2b. The second term in $\tilde{J}$ is produced by two optomechanical two-mode squeezing interactions with the cavity (left inset of Figure 6.2b.) If we absorb the frequency shifts into b_1 and b_2, the solutions are of the following form:

$$b_1(t) = c_1 e^{-\Gamma t/2} \left| \sin\left(\frac{Jt}{2}\right) \right| \tag{6.4.9}$$

$$b_2(t) = c_2 e^{-\Gamma t/2} \left| \cos\left(\frac{Jt}{2}\right) \right| \tag{6.4.10}$$

$$J = \sqrt{\tilde{J}^2 - \frac{\gamma_{12}^2 + \left(\gamma_{1tot} - \gamma_{2tot}\right)^2}{2}} \tag{6.4.11}$$

$$\Gamma = \frac{\gamma_{1tot}}{2} + \frac{\gamma_{2tot}}{2} \tag{6.4.12}$$

c_1 and c_2 are constants dependent on the initial conditions of the system. When we apply the swapping pulses to the optical cavity we see decaying oscillations which can be fitted precisely with the above equations. For large detunings where $J>\Gamma$, J is approximately $\tilde{J}$, so we treat them interchangeably in the main text.

We define the classical efficiency of an exchange pulse as the total number of phonons in the system after the pulse divided by the initial number of phonons in resonator 2. The efficiency of a π-pulse is $\exp(-\pi\Gamma/J)$ and the efficiency of a $\pi/2$-pulse is $\exp(-\pi\Gamma/2J)$. The efficiency of a π-pulse both theoretically and experimentally is plotted in Figure 6.8 as a function of detuning. A number of regions are inaccessible, because the optical damping is too large, and J becomes imaginary. In these overdamped regions, energy can still be transferred, but there is no coherent state transfer. If the optical cavity losses are reduced by a factor of four, more regions of small detuning would become accessible.

Thus far we have focused on the losses in the system, or the positive contributions to Γ. However, Γ has some contributions which are negative and correspond to parametric driving of the system. Parametric driving leads to an exponential increase in the motion of the resonators and is therefore equally as unsuited to efficient state transfer as configurations with large loss. However, it is possible to find detunings for which the heating and cooling contributions cancel, and Γ goes to zero. For these detunings classical state transfer is lossless, and the efficiency of state transfer goes to 1. In the current system such cancelation points only exist on the blue side of the cavity where the system is inherently unstable. However, if the cavity losses were reduced, a cancelation point appears on the red side, indicated by the star in Figure 6.8b. At this point the driving due to one laser beam just on the blue side of the cavity resonance is cancelled by the cooling due to the other laser close to the red sideband of resonator 1. This leads to significantly higher classical efficiency (>99%) and faster state transfer (J = 18 kHz.)

In the quantum regime, calculations of the efficiency are more complicated. The

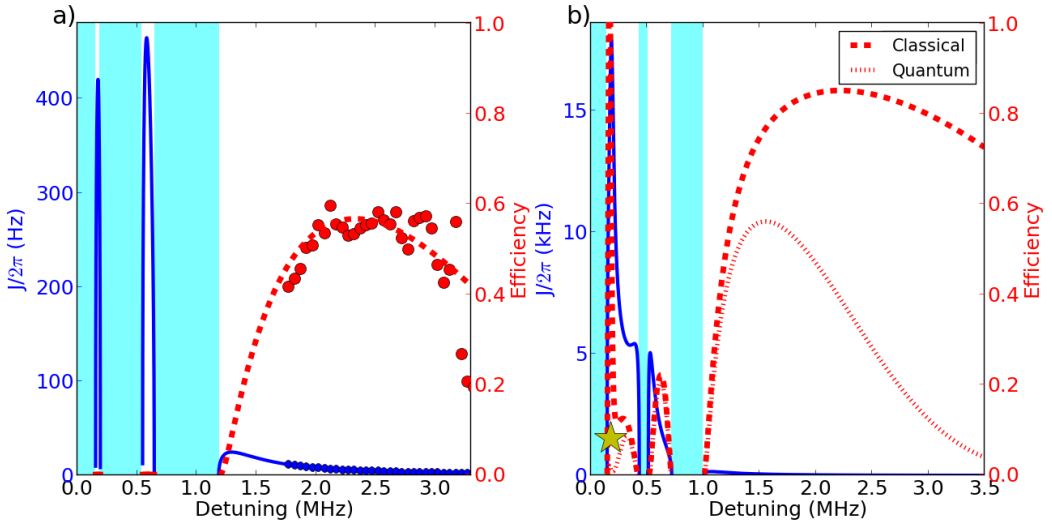

Figure 6.8: **Optomechanical swapping rate and efficiency.** Theoretical predictions for optomechanical swapping rate, J, and state transfer efficiency of a π-pulse are shown for $\kappa/2\pi = 200$ kHz and $P_{in} = 65$ μW in (**a**) and for $\kappa/2\pi = 50$ kHz and $P_{in} = 195$ μW in (**b**). The shaded regions indicate detunings for which the coupled system is overdamped and full coherent state transfer is impossible. We note that by improving the finesse by a factor of 4, a point appears (at the star) where the classical losses go to zero. The maximum swap rate can be increased to 18 kHz and the state transfer efficiency to greater than 99% at this point. The quantum case is more limited, but can still reach reasonable efficiencies at the central detuning.

parametric driving, which can allow for efficient classical transport, also introduces extra noise. Furthermore, quantum states with small phonon occupation have a large thermalization rate due to the high thermal occupation of the bath, even when the resonator is cooled down to millikelvin temperatures. In Figure 6.8b, we compare the classical and quantum efficiencies. At small detunings the quantum efficiency is limited by parametric driving and at large detunings by thermalization. Figure 6.8b also assumes a bath temperature of 10 mK and an improved linewidth of 10 mHz, which is in line with the improvements seen at cryogenic temperatures for many silicon nitride devices [121, 120]. These improvements should be enough to start using this protocol in the quantum regime. [2]

6.5 Conclusion

Exchange of mechanical energy between modes which are naturally uncoupled opens up many possibilities in quantum and classical physics. We have investigated the real time dynamics of such a system. We demonstrate that despite the many loss effects present, efficient coherent state transfer between two spatially and frequency separated mechanical resonators is possible. These results can be extended to the quantum regime to investigate quantum effects with many diverse mechanical oscillators. In the next Chapter we will investigate theoretically how this experimental setup and technique could be used to generate an entangled superposition state.

[2] The authors would like to acknowledge a related manuscript which appeared during the completion of this manuscript [152].

Chapter 7

Phonon Interferometry to Measure Decoherence

So far an optomechanical system which satisfies all of the constraints for the Marshall scheme [51] still remains out of reach, as discussed in Chapter 2. One particular challenge is the storage of the optical states, because optical loss rates are many orders of magnitude higher than mechanical loss rates. In this chapter we present a scheme for entangling two mechanical resonators in spatial superposition states such that all quantum information is stored in the mechanical resonators. The scheme is general and applies to any optomechanical system with multiple mechanical modes. By analytic and numeric modeling, we show that the scheme is resilient to experimental imperfections such as incomplete pre-cooling, faulty postselection and inefficient optomechanical coupling. [1]

[1] The contents of this chapter are based on the work by Weaver et al. [153], and are used with permission from the authors.

7.1 Introduction

In recent years macroscopic mechanical resonators have been developed with exceptionally high quality factors [154, 113, 120]. At the same time devices with a single photon strong cooperativity [112, 111, 52] are enabling manipulation of optomechanical systems at the single quantum level [7, 155, 38]. One promising technique for testing decoherence is to produce a spatial superposition state of one of these resonators, but this requires a controlling interaction with some other quantum system. We investigate a method for entangling two mechanical resonances and harnessing the advantageous capabilities of each resonator to study decoherence.

There are many proposed methods of producing a superposition state in an opto- or electromechanical system, all of which require the introduction of some nonlinearity. Examples of this include electromechanical systems coupled to a superconducting qubit [7, 155, 37] and optomechanical systems interacting with a single photon sent through a beam splitter [51]. However, the latter scheme is unfeasible with almost all current optomechanical systems, because it requires single photon strong coupling [51]. This requirement can be circumvented by postselection [53] or displacement [54], but these experiments are limited by the need for long storage of photons, which is lossy, and the requirement that cavity photons predominantly couple to a single mechanical mode. Here we propose a method to eliminate these constraints by entangling two mechanical modes optomechanically to avoid the losses and decoherence in optical and electrical systems.

Methods to generate optomechanical entanglement between multiple mechanical devices have been investigated extensively [156, 157, 158, 132, 133, 159, 160]. To generate a superposition, an interaction with two mechanical resonators is required [161, 162]. So far demonstrations of entanglement in optomechanical systems have used el-

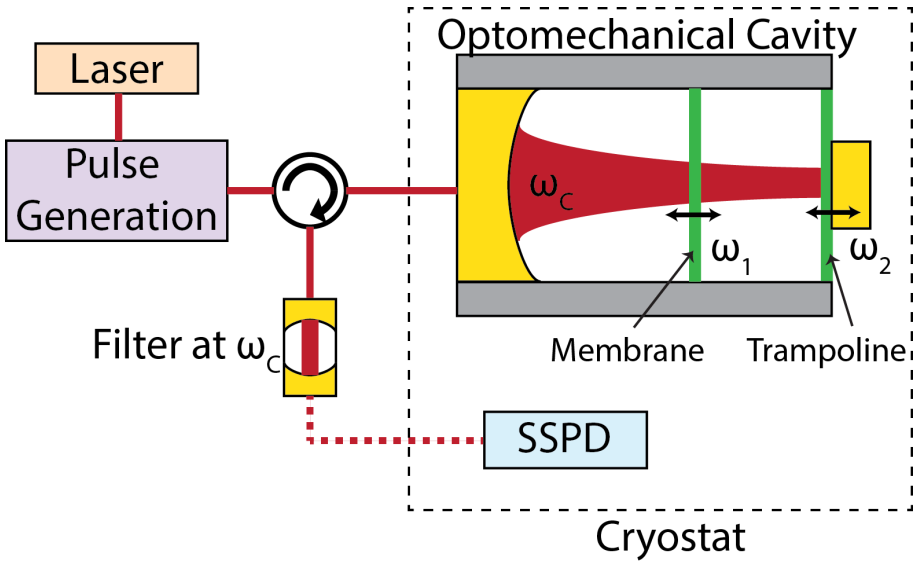

Figure 7.1: **Proposed experimental setup.** Two mechanical resonators are optomechanically coupled to an optical cavity. Here we show a membrane and a trampoline resonator with a mirror, but the procedure could be used for any two mechanical resonators coupled via an optical cavity field. A continuous wave laser is sent to an optical pulse generation setup, which produces pulses of varying frequency, duration, and intensity. The light enters the optomechanical cavity, and subsequently the reflected light is filtered to remove the control pulses. The filtered signal contains the single photons used for heralding and readout, which are measured with a superconducting single photon detector (SSPD).

ements with similar structure and frequency [163, 164, 165]. Flayac and Savona suggested that single photon projection measurements could generate an entangled superposition state between two resonators of similar frequency [162]. We propose a scheme which entangles resonators of different frequencies, so that it is easy to manipulate one resonator and to use the other (possibly more massive) resonator for tests of quantum mechanics.

7.2 Experimental Scheme

We consider an optomechanical system with one optical cavity and two mechanical resonators: an interaction resonator (resonator 1) and a quantum test mass resonator (resonator 2). The Hamiltonian for the system is the standard optomechanics Hamiltonian for multiple resonators [8]:

$$\hat{H}_0 = \hbar\omega_c \hat{a}^\dagger \hat{a} + \sum_{j=1,2} \hbar\omega_j \hat{b}_j^\dagger \hat{b}_j + \hbar g_j \hat{a}^\dagger \hat{a}(\hat{b}_j^\dagger + \hat{b}_j) \tag{7.2.1}$$

ω_c, $\hat{a}$, ω_j, $\hat{b}_j$ are the frequencies and bosonic ladder operators of the cavity and resonator j respectively. g_j are the single photon optomechanical coupling rates. The system is sideband resolved, with $\omega_j \gg \kappa$, the optical cavity linewidth. In Figure 7.1 the optomechanical setup is shown. A laser is modulated to generate control pulses, for instance by a series of acousto-optic modulators (AOMs). The pulses are sent into the cavity, and are filtered out of the light exiting the cavity so that only the remaining resonant light is incident on a single photon detector.

Figure 7.2 illustrates the method we propose to study decoherence. First both mechanical modes must be cooled close to the ground state using standard sideband cooling with two long laser pulses red detuned from the cavity resonance by ω_1 and ω_2 [41, 34, 33]. Next, we excite resonator 1 to its first excited state using a weak pulse

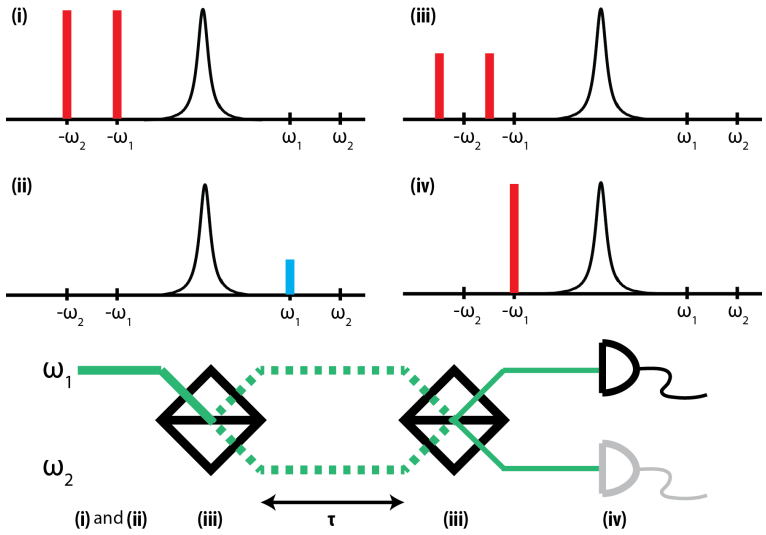

Figure 7.2: **Schematic control pulse overview.** This figure shows the four control pulses sent into the optomechanical cavity to execute the experiment. The pulses are: **(i)** Cooling to the ground state. **(ii)** Excitation to a coherent state, followed by postselection of the first excited state. **(iii)** A mechanical-mechanical interaction with $Jt = \pi/2$. **(iv)** Readout of a resonator. On the bottom, the equivalent optics experiment is shown with the corresponding steps. The greyed out detector is the optional addition of a readout pulse for resonator 2.

and projection measurement [86]. We perform a Mach-Zehnder type interference experiment on this initial state. To generate a beam splitter interaction between the mechanical resonators, we apply a two laser pulse, resulting in an entangled state: $|\psi\rangle = \frac{1}{\sqrt{2}}[|1\rangle_1|0\rangle_2 + i|0\rangle_1|1\rangle_2]$. The system now evolves freely for a time τ, possibly decohering during that interval. The frequency difference between the resonators causes the state $|\psi\rangle$ to pick up a phase difference of $(\omega_2 - \omega_1)\tau$. A second mechanical-mechanical interaction rotates the system to $\sin((\omega_2-\omega_1)\tau/2)|1\rangle_1|0\rangle_2 + \cos((\omega_2-\omega_1)\tau/2)|0\rangle_1|1\rangle_2$ if the system did not decohere. Finally, a laser pulse red detuned by ω_1 is used to swap the mechanical state of resonator 1 with that of the cavity and read it out with a photodetector.

We will now examine the steps in more detail, starting with the heralded generation of a single phonon mechanical Fock state [86], which has already been used to produce single phonon Fock states with reasonably high fidelity [38, 39]. Here we will review

the process briefly, including some of the imperfections in the generated state. A weak pulse of light, blue detuned in frequency by ω_1, is sent into the cavity, creating an effective interaction described by the Hamiltonian: $H_{\textbf{(ii)}} = \hbar\sqrt{n_{cav}}g_1(\hat{a}\hat{b}_1 + \hat{a}^\dagger\hat{b}_1^\dagger)$. n_{cav} is the number of photons in the cavity from the laser pulse. This generates an entangled state between the cavity and resonator 1: $|\psi\rangle = 1/\sqrt{2}(|0\rangle_c|0\rangle_1 + \sqrt{p}|1\rangle_c|1\rangle_1 + p|2\rangle_c|2\rangle_1)$, where $p \ll 1$ is the excitation probability. The light leaks out of the cavity and passes through a filter to isolate the resonant light from the blue-detuned pulse. By detecting a single photon, the mechanical resonator is projected onto $|1\rangle_1$, a single phonon Fock state. Because of the limited detection efficiency of cavity photons η, and the dead time of the detector, higher number states will be mistaken as single photons, so the probability p must be kept small to avoid inclusion of these states. Control pulse photons which leak through the filter and detector dark counts will incoherently add in $|0\rangle_1$ to the single phonon Fock state. Using a good filter and superconducting single photon detectors avoids the inclusion of the ground state [38]. Taken together these steps produce, with probability ηp, a heralded single phonon Fock state, and we can proceed to the interference experiment.

Exchange of quantum states is the essence of the interference experiment. In recent years there have been many demonstrations of opto- and electro-mechanically controlled coherent coupling between mechanical resonators [130, 146, 143, 73, 149, 136, 147]. All of these could be used to create an effective beam splitter interaction between two mechanical resonators. We will use the swapping method proposed by Stamper-Kurn et al. [148](and experimentally demonstrated in [129]), because it is quite general and couples resonators with a large frequency separation, which is important for the individual readout of each resonator. Two pulses of light, red-detuned and separated by $\omega_2 - \omega_1$ are sent into the cavity. These pulses each exchange excitations between one mechanical resonator and the cavity mode, resulting in a net swapping interaction with

rate J between the two resonators: $H_{\textbf{(iii)}} = \hbar J(\hat{b}_1^\dagger \hat{b}_2 + \hat{b}_1 \hat{b}_2^\dagger)$. This interaction can be used for both beam splitter interactions in the proposed experiment.

Finally, the readout for the system consists of a pulse of light, red detuned in frequency by ω_1. The readout interaction, $H_{\textbf{(iv)}} = \hbar\sqrt{n_{cav}} g_1(\hat{a}^\dagger \hat{b}_1 + \hat{a}\hat{b}_1^\dagger)$, exchanges excitations of resonator 1 with photons on resonance in the cavity. The anti-Stokes photons from the cavity are filtered and sent to a superconducting single photon detector to determine the phonon occupation of resonator 1 with a collection efficiency of η. Because of the difference in frequency of the two resonators, the measured phonon occupation of resonator 1 after the second mechanical-mechanical interaction oscillates as a function of the delay time τ at the frequency $\omega_2 - \omega_1$. However, if decoherence occurs during free evolution, the visibility of the oscillations will decrease. These features in the readout enable a simultaneous comparison of the coherent evolution, decoherence and thermalization of the system.

7.3 Expected Results

First we model the experiment analytically. We assume that in step **(ii)** of Figure 7.2 a perfect entangled state is generated, but that the off-diagonal elements of the density matrix decay exponentially with a decoherence time τ_d. The environment heats resonator 2, adding incoherently to the mechanical state. As an approximation, we assume that the state thermalizes from its average initial value of 1/2 to the thermal occupation of the environment, n_{env}. The average readout, R on the SSPD in step **(iv)** after many trials is the sum of the two effects:

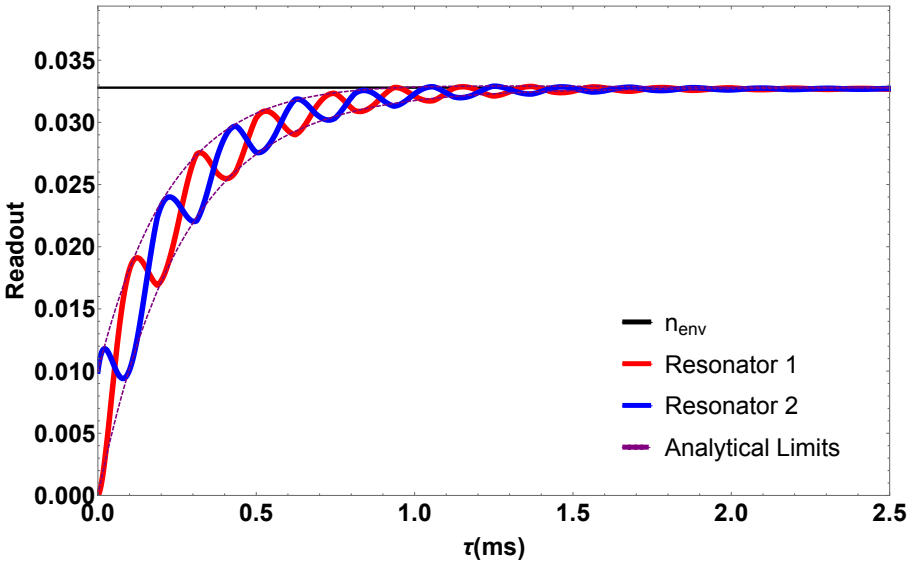

Figure 7.3: **Simulated decoherence results.** Expected results of a decoherence measurement with two entangled resonators in which one interacts with a thermal environment. The red (blue) indicates the readout of resonator 1 (2). Dotted lines are the limits set by the analytical model. Three effects are visible: coherent oscillations due to the frequency difference between the resonators, a decay of that coherence due to environmentally induced decoherence, and thermalization with the environment. The parameters for this plot are: ω_1 = 2 GHz, $\Delta\omega$ = 30 kHz, γ = 2 kHz, T_{env} = 0.1K, and η = 0.01.

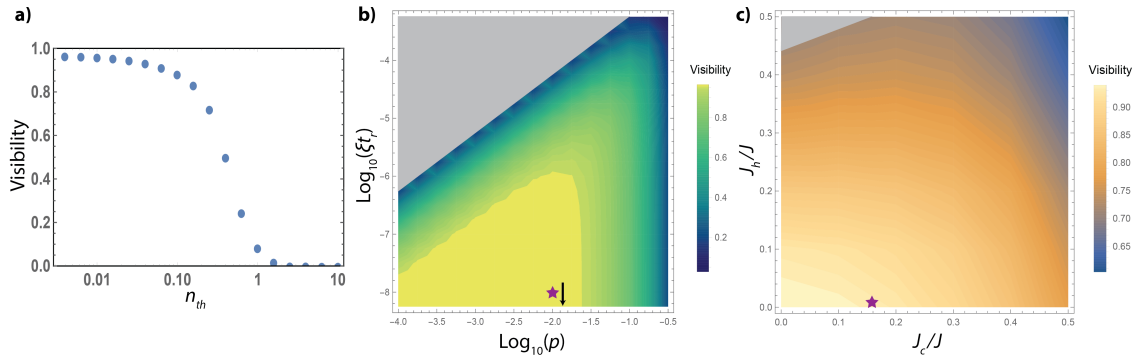

Figure 7.4: **Degradation of visibility from experimental imperfections.** The effects of several experimental imperfections on the resulting interference experiment, using the initial visibility as a metric. **a)** The two resonators are only cooled to a phonon occupancy of n_{th} in step **(i)**. **b)** The detector has a dark count probability of ξt_r for different probabilities of excitation, p in step **(ii)**. **c)** Step **(iii)** also induces an optical cooling rate J_c and an optical heating rate J_h in addition to the mechanical-mechanical coupling J. The greyed out regions indicate regimes in which the dominant behavior is not the desired entangled state. The purple stars indicate parameters already achieved in experiments: **b)**[39] and **c)** [129]. The unvaried parameters for these plot are: n_{th}=0.01, p=0.01, ξt_r=10^{-6}, η=0.01, and J_c=J_h=0.

$$\langle n_{dec}\rangle_2 = \frac{1}{2} - \frac{\cos\left[(\omega_2-\omega_1)\tau\right] e^{-\tau/\tau_d}}{2} \tag{7.3.1a}$$

$$\langle n_{th}\rangle_2 = \left(n_{env} - \frac{1}{2}\right)\left(1 - e^{-\tau/\tau_{th}}\right) \tag{7.3.1b}$$

$$R = \eta\left(\langle n_{dec}\rangle_2 + \langle n_{th}\rangle_2\right) \tag{7.3.1c}$$

n_{env}=$k_B T_{env}/\hbar\omega_2$ is the thermal occupation of the environment at temperature T_{env} and τ_{th} is the thermalization time constant. Three key features are visible in the readout signal: an oscillation at ω_2 -ω_1 which is evidence of coherence, an exponential decay of the coherent signal and an exponential increase in the phonon number as the system thermalizes.

We verify Equation 7.3.1 by performing a numerical simulation of the interaction between a mechanical resonator and its environment in the quantum master equation formalism. We assume that one resonator, the test mass resonator, has a much greater interaction rate γ with the environment, dominating the decoherence effects. Environ-

mentally induced decoherence can be modeled as an interaction with a bath of harmonic oscillators, leading to the following master equation [10, 9]:

$$\dot{\rho} = \frac{i}{\hbar}\left[\rho, \hat{H}_0\right] - \frac{D}{\hbar^2}\left[\hat{x}, \left[\hat{x}, \rho\right]\right] - \frac{i\gamma}{\hbar}\left[\hat{x}, \{\hat{p}, \rho\}\right] \tag{7.3.2}$$

$\hat{x}$ and $\hat{p}$ are the position and momentum operators for resonator 2, and D=$2m\gamma k_B T_{env}$ is the phonon diffusion constant. The numerical results are shown in Figure 7.3, and have excellent agreement with Equation 7.3.1.

We now discuss the experimental feasibility of this scheme with currently available technologies. We numerically simulate density matrices with the phonon states of each resonator as basis states. (Details in Appendix 7.6.) The initial visibility of the oscillations between the two resonators is a direct measure of the entanglement generation, and the decay of the visibility is the essential result of the experiment. Although the limit would depend on the exact experimental implementation, we estimate that the experiment would likely require an initial visibility greater than 10%. First we consider imperfections in step **(i)**, cooling to the ground state. Figure 7.4a shows the visibility achieved with a nonzero thermal phonon occupation. This occupation must be below about 0.7 for the experiment to be feasible.

Next we consider step **(ii)**, the postselection of a single phonon state. By changing the pulse strength, the probability p of an excitation can be adjusted. Dark counts on the single photon counter during the postselection will skew the produced state. Figure 7.4b shows the visibility as a function of p and dark count rate. There is a large region of parameter space with good visibility, and experiments are already well within this region (purple star) [39].

Finally, in step **(iii)**, the optomechanical beam splitter nominally only causes an interaction between the two mechanical resonators. However, the beams used to produce

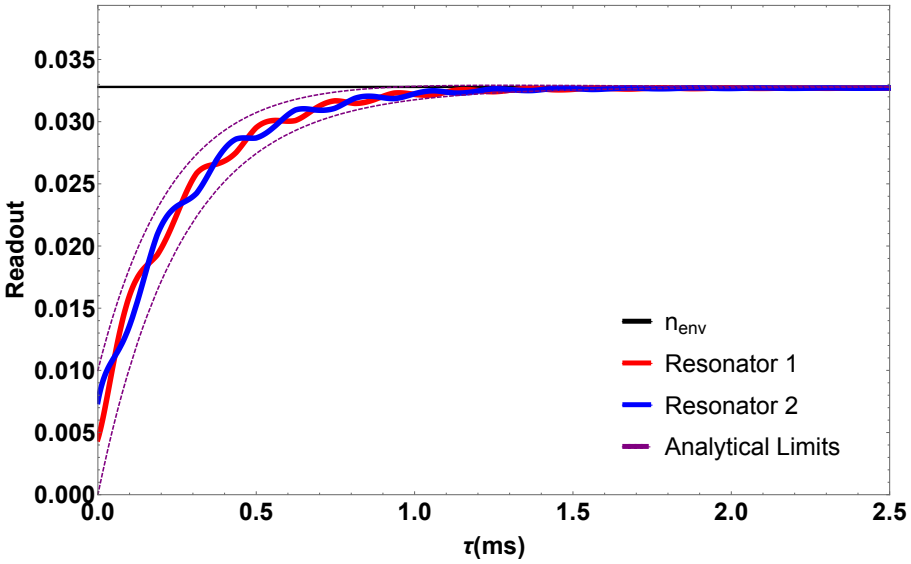

Figure 7.5: **Simulated results with imperfections.** Expected results of a decoherence measurement with imperfections present and an initial visibility of 30%. The parameters for this plot are the same as for Figure 7.3 with additional imperfections: $n_{th} = 0.4$, $p = 0.1$, $J_c = J_h = 0$. Despite the limited initial visibility all three effects are still visible: coherent oscillations due to the frequency difference between the resonators, a decay of that coherence due to environmentally induced decoherence, and thermalization with the environment. We estimate that the experimental limit on the initial visibility is around 10%.

the interaction also have heating and cooling effects. In Figure 7.4c the visibility as a function of cooling rate, J_c and heating rate J_h are shown. Again, experimental demonstrations of this type of beam splitter interaction are already sufficient to produce an interference experiment [129]. In Figure 7.5 we show numerical simulations of decoherence and thermalization that include experimental imperfections and an initial visibility of 30%. All of the qualitative features of Figure 7.3 are still easily discernable, indicating that the experiment should be feasible with these or even slightly worse parameters. There is a large area of experimentally achievable parameter space in all dimensions with visibility greater than 10%.

7.4 Timing Considerations

A number of experimental factors such as timing also play a critical role in the feasibility of the experiment. The probability of a successful postselection is ηp, and given this successful postselection the probability of measuring the result on the detector is η. Therefore, the experiment must be run $1/\eta^2 p \sim 10^6$ times to expect a single detection event. For many experimental implementations this is impossible, because it would take years to build up enough detection events. However, if there is no heralding of a single photon in step **(ii)**, there is no reason to continue the experiment. If we only continue to step **(iii)** after a successful postselection the time T required is:

$$T = n_a n_p \left(\frac{t_{12}(1-\eta p)}{\eta^2 p} + \frac{t_{tot}\eta p}{\eta} \right) \approx n_a n_p \frac{t_{12}}{\eta^2 p} \tag{7.4.1}$$

t_{12} and t_{tot} are the time required for step **(i)** and **(ii)** and for the total experiment respectively, and n_a and n_p are the number of averages and the number of points. In general, step **(iii)** and τ should dominate the experiment time, so this would drastically reduce the total experiment time. For a high frequency resonator with ~GHz frequency, reasonable parameters might be: $n_a = 1000$, $n_p = 30$, $\eta = 0.01$, $p = 0.01$ and $t_{12} = 1\mu s$, leading to an experiment time of about 8 hours. For lower frequency resonators, t_{12} might be closer to 100 μs, leading to an experiment time of about 35 days. The number of averages needed depends inversely on η, so $T \sim 1/\eta^3$, and the experiment can be drastically sped up by increasing η.

Many experiments which are proposed for testing novel decoherence mechanisms are in the lower frequency range. These experiments have the difficulty that their thermal environment contains more thermal quanta. In order to measure the full thermalization in addition to the decoherence, we must be able to count ηn_{env} photons. If an SSPD has a relatively short dead time (~100 ns) compared to the leakage time from the

cavity and filter (~50 μs) it may be possible to observe more than one photon. In general, however, the experiment should be constrained to $\eta \ll 1/n_{env}$. For low frequency resonators η may need to be artificially lowered. If this is the case, we suggest different detectors for step **(ii)** and step **(iv)** with different optical paths. If step **(ii)** has high efficiency η_1 and step **(iv)** has low efficiency η_2 the experiment time only slows down to $T \approx n_a n_p t_{12}/\eta_1\eta_2 p$ and it is possible to count higher phonon numbers with a reasonable increase in experiment time.

7.5 Experimental Implementations

This scheme can be performed with any two mechanical resonators coupled to an optical cavity. Here we will discuss three potential experimental setups, with an emphasis on using the technique to access decoherence information in large mass systems. One possible system is a Fabry-Pérot cavity with two trampoline resonators: one with a distributed bragg reflector (DBR) and one without. This system has already been constructed [129]. The two resonators have frequencies in the hundreds of kHz range, a mass of 40 ng and 150 ng and a single photon cooperativity 0.0002 and 0.0001 respectively. The authors suggest methods for lowering optical and mechanical damping, which would improve the single photon cooperativity to 0.2 and 0.01. The scheme presented here enables single phonon control of the massive DBR device despite its relatively small single photon cooperativity.

Another possible system would be a membrane in the middle at one end of a Fabry-Pérot cavity and a cloud of atoms trapped in the harmonic potential of the standing wave in the cavity at the other end. The optomechanical coupling enables the direct coupling between the ~zg cloud of atoms and the ~100 ng membrane. Clouds of atoms and membranes have already been coupled between different cavities [166, 167], and this scheme

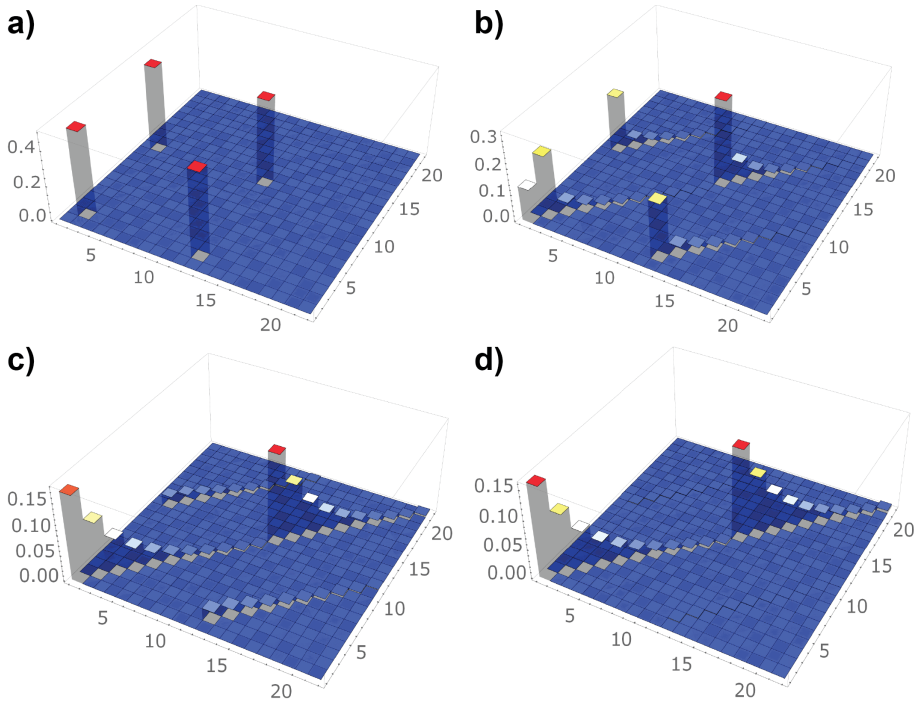

Figure 7.6: **Density matrix representation of decoherence and thermalization.** Each matrix is plotted during step **(iii)** after a delay time τ of **a)** 0 ms **b)** 190 ms **c)** 950 ms **d)** 3.8 s. The states labeled 1 to 22 in the figure correspond to the basis states $\{00,01,...,09,010,10,11,...,19,110\}$. The relevant parameters are ω_2 = 10 GHz, γ = 1 Hz and T_{env} = 0.2 K.

could be modified to use that interaction for step **(iii)**. One could also imagine making a cavity with a bulk acoustic wave resonator coupled to a small high frequency membrane. These modes can have exceptionally high Q-factors and large mode mass [154].

7.6 Numerical Methods

In the main text we investigate two main problems. The first is the interaction of a mechanical entangled state with the bath of one resonator. We use a numerical differential equation solver to solve the Master Equation (Equation 7.3.2) with density matrices. After some algebraic manipulation, this can be rewritten as a set of differential equations:

$$\rho = \sum_{p,q,r,s=0}^{\infty} a_{pqrs}(t)\,|pr\rangle\langle qs| \tag{7.6.1}$$

$$[\hat{x},[\hat{x},|r\rangle_2\langle s|_2]] = \sum_{k,l}\Gamma_{klrs}\,|k\rangle_2\langle l|_2 \tag{7.6.2}$$

$$\left[\hat{x},\left\{\hat{p},|r\rangle_2\langle s|_2\right\}\right] = \sum_{k,l}\Phi_{klrs}\,|k\rangle_2\langle l|_2 \tag{7.6.3}$$

$$\begin{aligned}\dot{a}_{pqrs}(t) &= -i\left(\omega_1(p-q)+\omega_2(r-s)\right)a_{pqrs}(t)\\ &- \frac{D}{\hbar^2}\sum_{k,l=0}^{\infty}\Gamma_{rskl}a_{pqkl}(t)\\ &- \frac{i\gamma}{\hbar}\sum_{k,l=0}^{\infty}\Phi_{rskl}a_{pqkl}(t)\end{aligned} \tag{7.6.4}$$

The commutation relationships in the equations lead to a number of overlap integrals between number states, which can be evaluated and plugged in to create numerically solvable equations. To solve for the dynamics of this system we use a density matrix with basis states {00,01,...0n,10,11,...1n} where n is a number much larger than n_{env}. Figure 7.6 shows the results of the simulations for n=10 at four different times before the second swapping pulse. Two main effects are observable in the evolution of the density matrix. First, the population of the density matrix spreads out along the diagonal of each of the four quadrants. Second, the non-diagonal matrix elements decay away. These effects match with the expected behavior for thermalization and decoherence.

We also need to simulate a mechanical-mechanical $\pi/2$ pulse. Because it is equivalent to a beam splitter the effect on the two modes is the same. Here we expand the density matrix to have basis states {00,01,...0n,10,11,...1n,n0,n1,...nn}. The beam splitter interaction conserves energy, so it can represented as a n^2xn^2 transformation matrix, which recombines the elements of common phonon number. The transformation matrix S_{BS} for the three lowest energy levels with basis states {00,01,10,02,11,20} is:

$$S_{BS} = \begin{pmatrix} 1 & 0 & 0 & 0 & 0 & 0 \\ 0 & 1/\sqrt{2} & -1/\sqrt{2} & 0 & 0 & 0 \\ 0 & 1/\sqrt{2} & 1/\sqrt{2} & 0 & 0 & 0 \\ 0 & 0 & 0 & 1/2 & -1/\sqrt{2} & 1/2 \\ 0 & 0 & 0 & -1/2 & 0 & 1/2 \\ 0 & 0 & 0 & 1/2 & 1/\sqrt{2} & 1/2 \end{pmatrix} \tag{7.6.5}$$

After the beam splitter interaction the density matrix ρ' is $S_{BS}^T \rho S_{BS}$. The combination of these two techniques lets us fully model how the ideal state interacts with its thermal environment.

The other problem we investigate is how various experimental imperfections can impact the initial visibility of the experiment. For this we use density matrices with basis states going up to n=3. To model imperfect cooling in step **(i)** we start with a thermal state of both resonators. The modeling of step **(ii)** is a little more complex. A successful postselection means that 1 phonon has been added to resonator 1. However, with probability p, the phonon occupation should be incremented by 2, and with probability p^2 by 3, and so on. Conversely, if there is a dark count or leaked pulse photon (probability ξt_r) the phonon occupation should remain the same. Finally, we implement the beam splitter, step (iii), in the same way as above. We add in an additional cooling pulse with a probability J_c/J of removing a phonon from one of the resonators and a heating pulse with a probability J_h/J of adding a phonon to a resonator. The cooling matrix transformation S_c with basis states {00,01,02,10,11,12,20,21,22} is:

$$S_c = \left(1 - \frac{J_c}{J}\right) I + \frac{J_c}{J} \begin{pmatrix} 0 & 1 & 0 & 1 & 0 & 0 & 0 & 0 & 0 \\ 0 & 0 & \sqrt{2} & 0 & 1 & 0 & 0 & 0 & 0 \\ 0 & 0 & 0 & 0 & 0 & 1 & 0 & 0 & 0 \\ 0 & 0 & 0 & 0 & 1 & 0 & \sqrt{2} & 0 & 0 \\ 0 & 0 & 0 & 0 & 0 & \sqrt{2} & 0 & \sqrt{2} & 0 \\ 0 & 0 & 0 & 0 & 0 & 0 & 0 & 0 & \sqrt{2} \\ 0 & 0 & 0 & 0 & 0 & 0 & 0 & 1 & 0 \\ 0 & 0 & 0 & 0 & 0 & 0 & 0 & 0 & \sqrt{2} \\ 0 & 0 & 0 & 0 & 0 & 0 & 0 & 0 & 0 \end{pmatrix} \tag{7.6.6}$$

The heating matrix transformation is S_c^T. All of these imperfections are combined to determine their impact on the proposed experiment.

7.7 Additional Experimental Considerations

The first additional consideration relates to the pulses used in the experiment. It is possible to perform the experiment with simple square-shaped pulses. However, it is more efficient to use an exponentially shaped pulse, resulting in a more even interaction time [168]. We suggest using pulses of that shape, as is performed in [39]. In particular, it is crucial that the area under the readout pulse: $\int_0^\infty n_{cav}(t) g_1 dt$ is $\pi/2$ to fully readout the phonon occupation of resonator 1.

We also consider the most effective detuning of the two laser beams for performing a $\pi/2$ pulse. The two laser tone exchange method relies on exchanging the state of each mechanical resonator with that of the cavity. This is fastest if the two laser beams are red detuned to ω_1 and ω_2. However, at this detuning quantum information leaks out of the cavity, leading to large values of J_c and J_h. In Figure 7.7 we examine the effects

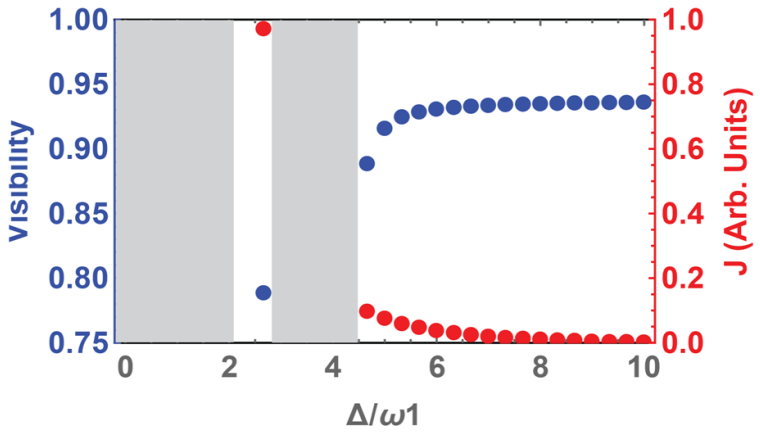

Figure 7.7: **Visibility as a function of detuning.** Greyed out regions have too high J_c or J_h to run the experiment. The value of J depends on the exact experimental parameters, so it is normalized to the highest value. Parameters are $\omega_2/\omega_1 = 2$, $\omega_1/\kappa = 10$, n_{th}=0.01, p=0.01, ξt_r=10^{-6} and η=0.01.

of the average detuning Δ of these two laser beams. Ideally the two beams should be quite far detuned from the cavity, but there is a tradeoff between efficient exchange and the exchange rate, J, shown in red [129]. The best detuning depends on experimental parameters such as sideband resolution and frequency of the resonators.

7.8 Discussion

There are a number of distinct advantages of the method proposed here. First, the readout of phonon occupation naturally lends itself to studying thermalization and decoherence together in the same system and on the same time scale. This has never been observed before in mechanical resonators. A thorough understanding of the mechanics of thermalization and decoherence is necessary in order to verify that unknown faster decoherence processes can be attributed to new physics. Second, this experiment can easily be compartmentalized into the four constituent steps, and each one tested indi-

vidually. This would make it easier to build up to the final experiment with confidence in the results. In particular, one could obtain interference results from two resonators in a classical state, so it is essential to demonstrate that the procedure is performed with a single phonon. Finally, this scheme can use mechanical resonators with different frequencies and masses, so that large systems with relatively small optomechanical coupling rates can be studied.

7.9 Conclusion

We have proposed a scheme to entangle two mechanical resonators with a shared single phonon. Using interferometry and phonon counting we could simultaneously measure decoherence and thermalization of a macroscopic mechanical mode. The methods proposed are quite general, and can be applied to any sideband resolved two mode opto- or electro-mechanical system. Furthermore, the scheme is resilient to experimental imperfections in its constituent steps. This technique could greatly expand our understanding of the quantum to classical transition in mechanical systems.

Chapter 8

Towards the Quantum Regime

There is still work that needs to be done before nanogram scale objects can be placed into spatial superposition states. In this chapter we discuss some of the efforts that are ongoing or starting up with the goal of performing quantum optomechanics experiments. We start off with efforts to cool trampoline resonators close to their ground state of motion. We then discuss some basic experiments with silicon nitride membranes, and finally some theoretical work on displacement of quantum states with a coherent light beam.

8.1 Cooling Trampoline Resonators

We will use two methods of cooling to lower the phonon occupation of our resonator: regular cryocooling and laser sideband cooling. In order to have more than a 50% probability of occupying the ground state, a 300 kHz resonator must be cooled to below 10 μK. We can cool to approximately 15 mK with a dillution refrigerator, but to reach the ground state we must laser cool the rest of the way down.

We first investigate the effectiveness of optical sideband cooling a nested trampoline

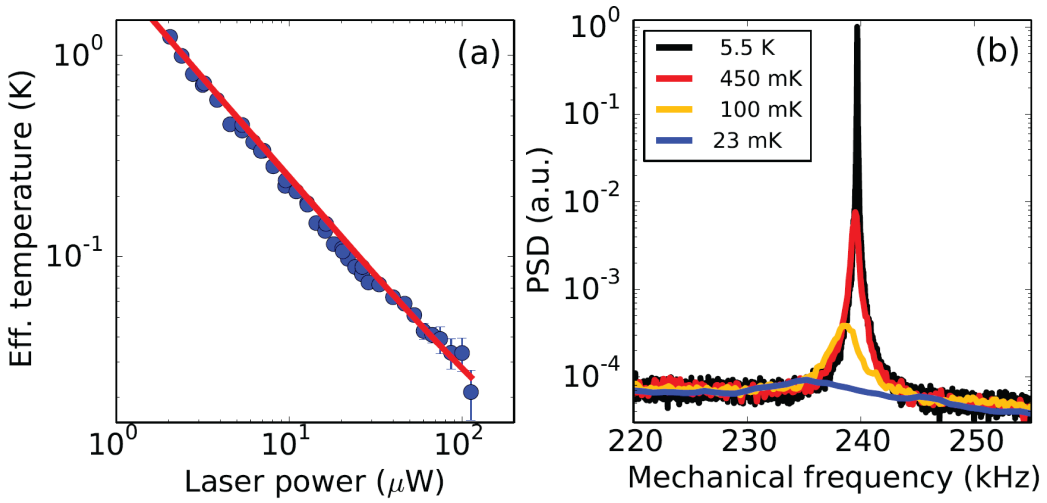

Figure 8.1: **Optical sideband cooling of a nested trampoline resonator. a)** As the pump laser power is increased the effective temperature of the resonator decreases linearly, reaching a minimum temperature of 23 ± 5 mK. **b** The power spectral density of the mechanical motion is used to extract the effective temperature. Figure courtesy of Hedwig Eerkens.

resonator from room temperature. One laser, the probe beam, is locked to the cavity resonance to measure the mechanical motion. A second laser, the pump beam, is locked to the first with a phase lock loop one FSR away, red detuned by the mechanical frequency (See [87] and Chapter 6.) We measure the dependence of optical cooling on laser power by varying the strength of the pump beam. The results are shown in Figure 8.1. We can cool to an effective temperature of 23 ± 5 mK from room temperature. Note that the spectrum of the nested trampoline resonator remains free of other mechanical peaks, a result of the vibration isolation (Chapter 4.) The amount of cooling is limited by the linewidth of the resonator and by an instability due to the optical spring effect on the outer resonator at large pump powers [50]. The instability can be ameliorated by electrical feedback on the outer resonator. Nevertheless, a cooling fraction of 1.3 x 10^4 is achieved, which would be sufficient for ground state cooling from 100 mK.

We place the optomechanical cavity in a dilution refrigerator with a base temperature of around 15 mK. The cavity shrinks significantly, so the system must be actively

aligned during the cooldown. Due to scattering and absorption in the system, the optical bench heats up to around 200 mK when the lasers are sent into the cavity. Unfortunately, this means that we have a starting temperature of the resonator between 100 mK and 1 K, depending on the laser power in the cavity. So far efforts to reach the ground state have been unsuccessful because of classical laser noise [169] and absorptive heating in the device [49]. Classical laser noise can be eliminated with a filter cavity [169]. Eliminating absorptive heating is more difficult, but it could possibly be achieved with off-resonant readout of the mechanical motion [170]. A more likely route forward is to reduce mechanical losses, so that the same optical laser power achieves greater cooling, and to reduce the optical losses directly through different materials or geometries.

8.2 Membrane in the Middle

The membrane in the middle geometry has a number of advantages over DBR trampoline resonators for optical cooling. First, the membrane in the middle can have a thickness of 20 to 80 nm. This means that there is a much smaller volume of the caviy optical modes within the nitride compared to DBR mirrors where the optical mode penetrates microns into the material. As discussed in Chapter 5, membrane only devices have also acheived a much higher Q due in part to the lack of material junctions in the device [113, 111, 171]. With these advantages membrane in the middle systems have been cooled to near the ground state [35, 36, 73]. As we showed in Chapter 6, a membrane in the middle is fully compatable with the optical setup and measurement techniques we used in this thesis. We therefore build up a membrane in the middle system as another alternative for macroscopic quantum optomechanics.

We construct a 10 cm long cavity out of invar with fixed end mirrors, and place a Norcada Si_3N_4 membrane with a thickness of 50 nm [104] in the middle. Because of the

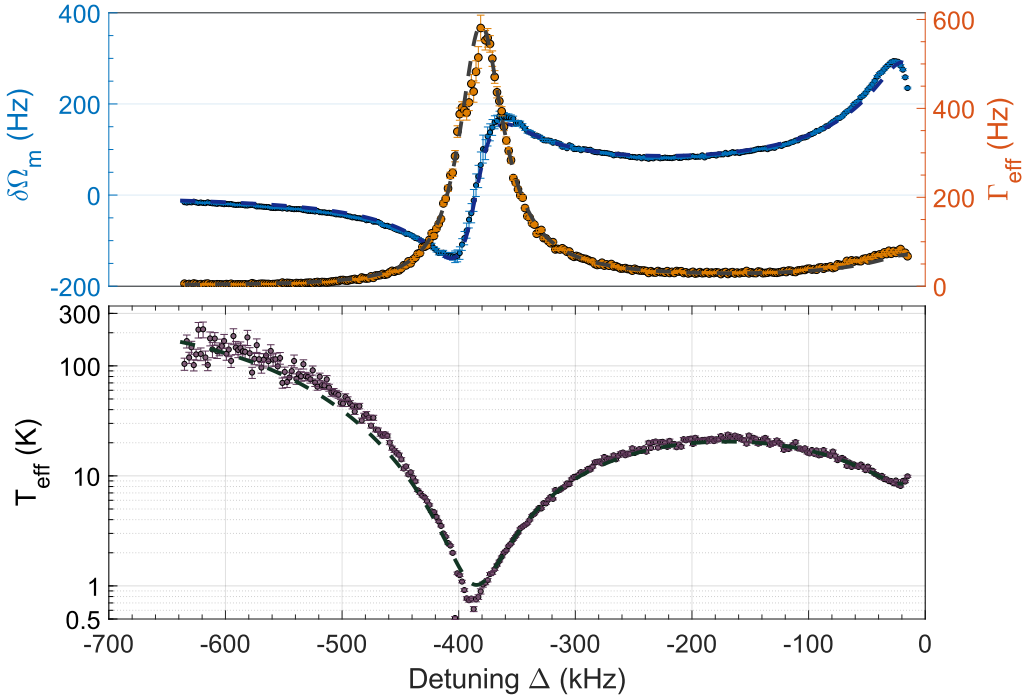

Figure 8.2: **Optical spring effect, damping and effective temperature as a function of detuning.** As we vary detuning the optical spring effect (blue), the optomechanical damping (orange) and the effective temperature (purple) vary with excellent agreement to theory. Figure courtesy of Sameer Sonar.

asymmetry induced by the presence of a membrane in the middle, it is preferable to lock two lasers with a separation of two FSRs, so that both cavity modes adressed have the same optomechanical coupling (see Figure 2.3.) The cavity length is twice the original 5 cm used in earlier chapters, so the FSR is 1.5 GHz, and we can lock two lasers at a spacing of 3 GHz with the same optical setup used in Chapter 6.

To show that this system has similar capabilities to the DBR trampoline system, we perform a detuning sweep of a pump laser with respect to the cavity resonance. When the detuning matches the mechanical frequency, the damping is maximal and the optical spring effect switches sign. Even in this first exploratory experiment with intermediate power we cool the mechanical resonator to an effective temperature below 1 K. The results are shown in Figure 8.2 and show excellent agreement to theory indicating excellent control over the laser detuning and a good cavity lock over the long periods of time necessary to take such a sweep. These large square membranes have many mechanical modes available for performing swapping experiments. The successful detuning sweep makes this a promising system for experiments which extend the results of Chapter 6. In particular, it could be interesting to investigate STIRAP-like protocols for an optomechanical system [142, 172]. These might make the swapping procedure quicker, a helpful addition for attempting the scheme of Chapter 7.

8.3 Conclusion

We have continued to push macroscopic optomechanical resonators towards the quantum regime and spatial superposition states. The phonon occupation of DBR trampoline resonators has been reduced significantly, and we have also demonstrated preliminary optomechanical capabilities in a membrane in the middle system. The investigations we have performed in the classical regime will play an important part in setting

up quantum experiments and many of the techniques from this thesis will inform future quantum superposition generation experiments.

Appendix A

Fabrication

In this Appendix, we give details about the fabrication of the devices contained in this dissertation, including materials, complete fabrication steps, and mask design layouts. As a fun way to keep track of different designs, each design is named after a chimera.

A.1 Overview of Fabrication Runs and Materials

We start out with three tables. Tables A.1 and A.2 detail all of the different processes we ran, the materials used and the experimental purpose of each run. These tables connect results from the main text with mask designs and specific fabrication steps. Table A.3 gives information about the starting materials we used for fabrication, which were procured from academic and industrial clean rooms.

Abbreviation	Mask	Material	Device Purpose	Chapter, Section or Publication	Notes	Year
CHS1,CHS2	Cama	M1 500nm	Determine the effect of mirror size on finesse and mechanical Q	Chapter 3 [87, 88, 80]	-Coloring effects around the mirror are caused by trenching	2013 2014
LHS1-LHS5	Liger	M1 300 nm 500 nm	-Testing designs for creating an outer resonator around the inner resonator	Chapter 4	-Significant breaking of the outer resonator due to curvature of the mirror layers and sharp corners in silicon	2014
LIG6-LIG8	Liger2	M2 500 nm	Finalize the design for the outer resonator	Chapter 4 [89]	-APL cover photo -Low stress LPCVD nitride	2014 2015
WOL1	Wolphin	M2 500 nm	-Test a single resonator per chip -Materials Testing	Chapter 3	-Low stress LPCVD nitride	2015
WHO2	Wolphin	M1 300 nm	-Test a single resonator per chip -Materials Testing	Chapter 3	-Mounting with In reduces external mechanical modes	2015
ZOR1-ZOR4	Zorse	M2 500 nm M1 300 nm	-Test if one device per chip is better -Add capacitive control to back	Section 4.5 [107]	-Zor1 is M2, others are M1 -ZOR3 and ZOR4 added a protective SiO_2 and SiN ring to the back -back of some chips coated with Al at an angle	2015
ZBC1,ZBC2	Zorse(BC)	M4	-Make a second chip to attach to the back for capacative control	Section 4.5	-Al layer recessed by 20 μm	2015

Table A.1: **An overview of the fabrication runs (Part I)**. This table is a reference for the fabricated chips used in this dissertation and other referenced works.

Abbreviation	Mask	Material	Device Purpose	Chapter, Section or Publication	Notes	Year
JAC1,JAC2	Jackalope	M1 500 nm	-Test inner resonator geometries with different clamping	Chapter 5		2015 2016
GBU1-GBU5	Golar Bear	M2 500 nm M3 450 nm	-Undercut the DBR mirror to make a pedestal	Chapter 5 [108]	-GBU1-3 are M2, GBU4,5 are M3 -Only GBU4 and GBU5 were succesful at protecting the DBR mirror -GBU3_1 was used as a materials test and also for [108]	2016
GBD1,GBD2	Golar Bear	M2 500nm	-Test out idea for double sided resonator	Chapter 5 Chapter 6 [129]	-Low stress LPCVD nitride	2016
DSNR1-DSNR4	Golar Bear	M3 450 nm 300nm	-Produce Double Sided Devices	Chapter 5 Chapter 6 [129]	-DSNR1 and DSNR2 fabricated by Fernando	2016 2017

Table A.2: **An overview of the fabrication runs (Part II)**. This table is a reference for the fabricated chips used in this dissertation and other referenced works.

Coating Set	**Year**	**Si Thickness**	**Si_3N_4 Thicknesses**	**Si_3N_4 Deposition Location**	**DBR Composition**	**DBR Deposition Company**	**Notes**
M1	2013	500 μm	500 nm 300 nm 0 nm	UCLA	HWL SiO_2 33 QWL SiO_2/Ta_2O_5 287.6 nm SiO_2 140.9 Ta_2O_5 HWL SiO_2	ATF	-procured by Brian Pepper
M2	2014	500 μm	500 nm	UCLA	39 QWL SiO_2/Ta_2O_5 10 nm SiO_2	ATF	-accidentally low stress Si_3N_4 -I deposited a HWL of SiO_2 on top of the wafers used in later runs
M3	2016	500 μm	450 nm 300 nm	Rogue Valley	HWL SiO_2 39 QWL SiO_2/Ta_2O_5 HWL SiO_2	Laser Optik	-started in summer 2015
M4	2015	400 μm	-	-	20 μm Si 2 μm SiO_2	-	-SOI wafer from

Table A.3: **An overview of the coating runs.** The coating runs in this table provided the starting materials for the fabrication process. HWL and QWL are half and quarter wave layers respectively. The DBR composition goes from top to bottom.

A.2 Detailed Fabrication Steps

A.2.1 Fabrication for Nested Resonators

1. DBR Layer

   (a) Cleave chips out of starting material.

   - 15 x 15 mm squares
   - Carefully blow off all dust from surface.

   (b) Solvent Clean

   - Acetone 3 min., Isopropanol 3 min., DI Water 1 min, blow dry

   (c) Contact Lithography with SPR 220-7 resist.

   - Spin on resist 3500 rpm for 45s. Edge bead removal with a razor. 120s bake at 115°C
   - Contact aligner, using best corner for angular reference, 60s exposure.
   - Wait 20 min.
   - Develop 75s in AZ300MIF.

   (d) Inductively Coupled Plasma Etch (ICP)

   i. O_2 clean 10 min, CHF_3 coat 1 min

   ii. Etch 10 min with CHF_3, then take and fit a reflectance spectra from the filmetrics to determine etch depth and rate

   iii. 15 min O_2 clean, necessary because this is a dirty process.

   iv. Repeat and etch down through the DBR, leaving only the Si_3N_4 layer and 50-100 nm of the bottom SiO_2 layer.

   (e) Solvent Clean

2. Top Nitride Layer

   (a) Stepper Lithography with SPR 220-3 resist.

      - Spin on resist 2500 rpm for 30s. 90s bake at 115°C
      - Stepper Aligner (GCA 6300), 2.4s exposure, focus offset 10.
      - Develop 65s in AZ300MIF.

   (b) CF_4 etch in asher

      - Keep chips away from center and make sure to avoid dirt and excessive scratches to avoid etching the back nitride.
      - Check rate with nanometrics and etch all the way down to the Si.

   (c) Do *not* remove resist.

3. Si Removal

   (a) IR Contact Lithography with SPR 220-7 resist on back of chip.

      - Spin on resist 3500 rpm for 45s. *No* edge bead removal. 120s bake at 115°C
      - IR Contact aligner, 60s exposure. Suggestion: use an IR setting of about 5.5 and align to the outer resonator arms.
      - Wait 20 min
      - Develop 75s in AZ300MIF.

   (b) CF_4 etch in asher

      - Check rate with nanometrics and etch all the way down to the Si.

   (c) Deep Reactive Ion Etch (Bosch) to remove 400 μm of Si.

      - Check etch rate with optical microscope.

4. Device Release

   (a) Solvent Clean

   (b) Piranha Clean

      - 5:1 H_2SO_4:H_2O_2 at 90-100°C for 10 min

   (c) Solvent Clean

   (d) 10 % TMAH etch for approximately 2 hours until device is released

      - Use condenser with chiller at 10°C to maintain concentration.

   (e) Dilution under water

   (f) 60s Buffered HF dip

      - This must again be followed by dilution.

   (g) Transfer to Ethanol, remove, then place on a hot plate.

A.2.2 Fabrication for Double Sided Nested Resonators

1. Deposition
    (a) Cleave chips out of starting material.
    (b) Deposite approximately 1 μm of SiO_2 using PECVD1
    (c) Deposite approximately 300 nm of SiN using PECVD1
2. DBR Layer
    - same as above
3. Top Nitride Layer
    - same as above
4. Back Protective Layer
    (a) IR Contact Lithography with SPR 220-3 resist on back of chip.
    (b) CHF_3 etch in ICP
        - Approximately 10 min.
    (c) Solvent Clean
    (d) Spin SPR 220-3 resist on front of chip and bake for 5 min.
5. Si Removal
    - same as above
6. Device Release
    - same as above

A.2.3 Fabrication for Undercut DBR mirrors

1. DBR Layer

   (a) Cleave chips out of starting material.

   (b) Contact Lithography with SPR 220-7 resist.

   (c) Inductively Coupled Plasma Etch (ICP)

   - Etch down to the top of the bottom SiO_2 layer, etching approximately 50 nm into the layer. It is crucial that this layer not be removed, and that the trenching next to the DBR mirror does not go into the Si_3N_4 layer. It is also crucial that there is no Ta_2O_5 left. This is a somewhat difficult “Goldilocks" condition to meet.

   (d) Solvent Clean

2. Top Nitride Layer

   (a) Stepper Lithography with SPR 220-3 resist.

   (b) CHF_3 etch in ICP

   - Should take about 10 min.

3. Si Removal

   - same as above

4. DBR Undercut

   (a) Solvent Clean

   (b) Deposit Cr

- Using E-beam 1, deposite 2000 Å of Cr on the device while rotating the chip at an angle of 80° to the vertical. This is so that the Cr will coat the edges of the DBR mirror.

(c) Stepper Lithography with SPR 220-3 resist.

- Bake for 5 min at 115°C

(d) Cr removal

- Use Cr etchant for 2 min.

(e) HF Undercut

- Etch for approximately 90 min in BHF.

(f) Solvent Clean and Cr removal

- Use Cr etchant for 3 min.

5. Device Release

- same as above

A.2.4 Fabrication of an SOI metal back chip

1. Deposition
    - Deposite 250 nm of SiO_2 with PECVD 1 on front.
2. Front Side
    (a) Contact Lithography with SPR200-3
    (b) 90 s HF dip
    (c) XeF_2 etch
        - Continue etch until the bottom of the channel appears completely smooth.
    (d) Deposit 1000 Å of Al with the thermal evaporator
    (e) Liftoff the top layer of Al
        - Use 1165 stripper overnight to remove top layer of resist and Al
    (f) Solvent Clean
3. Back Side
    (a) IR Contact Lithography with SPR200-7
    (b) DRIE Bosch etch all the way through the chip

A.3 Masks

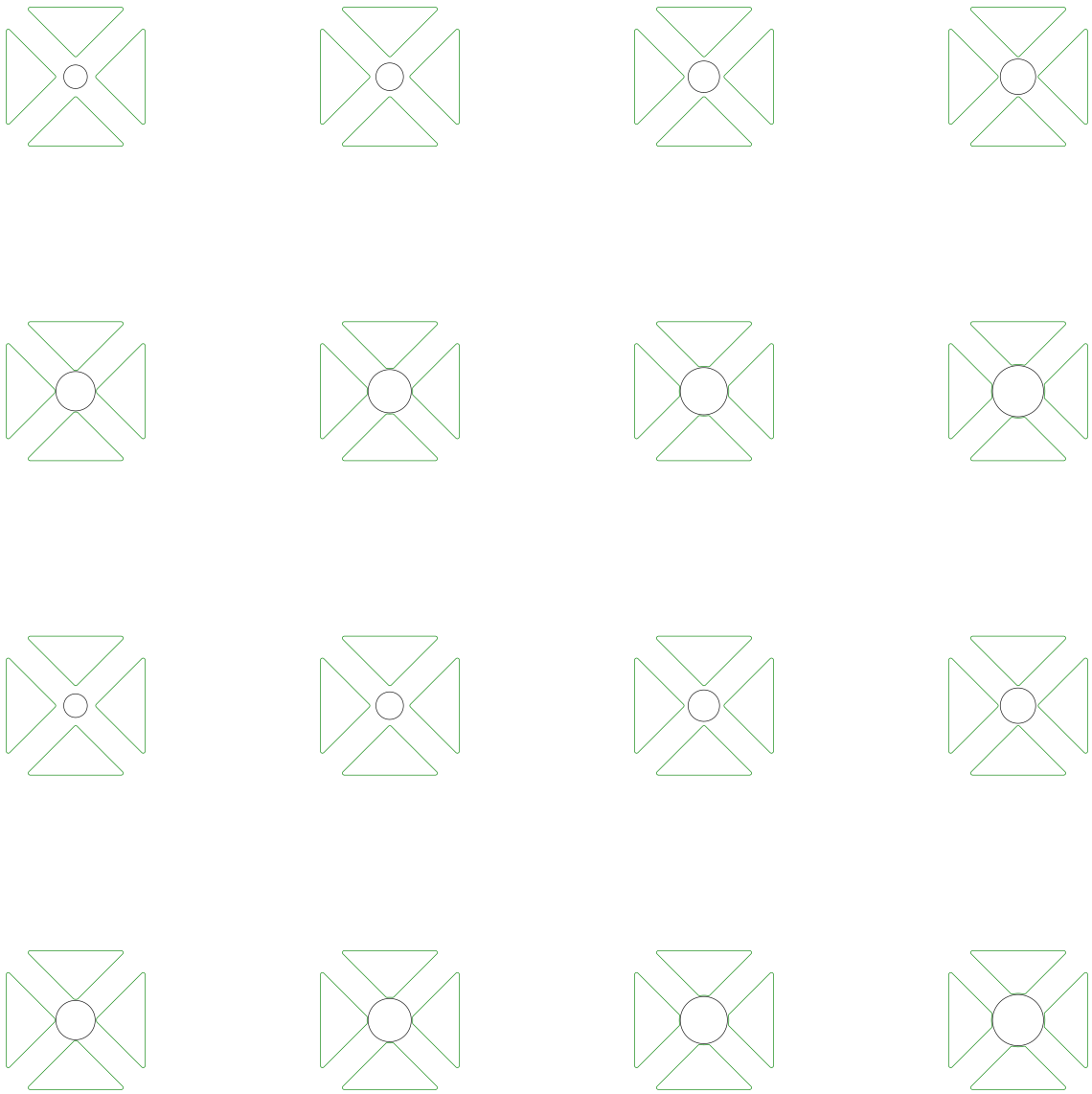

Figure A.1: **The Cama mask design.** This mask set tests out different mirror sizes. The device diagonal is 500 μm. Black is the mirror layer and green is the nitride layer.

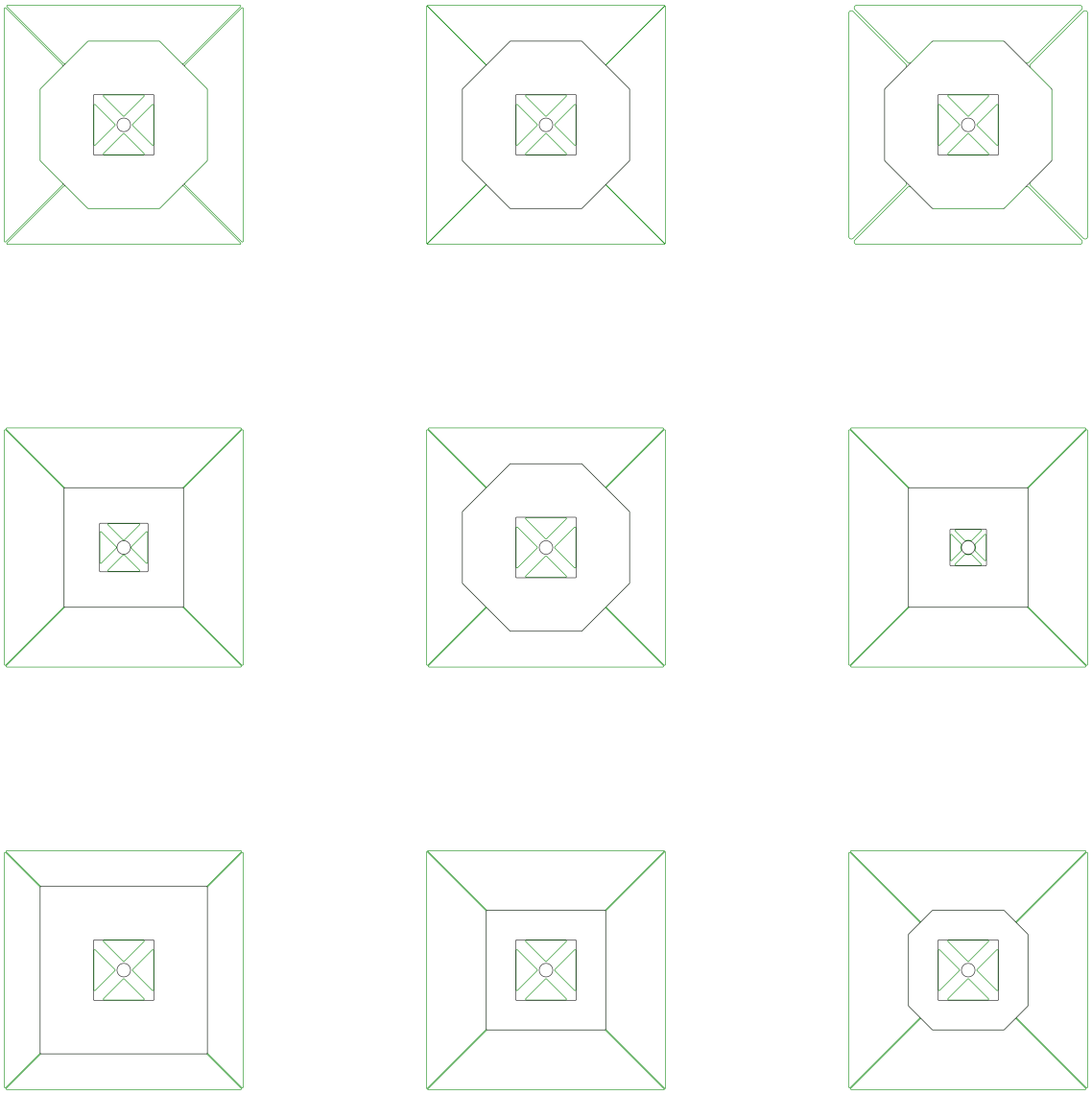

Figure A.2: **The first Liger mask design.** This mask set surrounds the inner resonator with an outer resonator with various designs. The device diagonal is 2 mm. Black is the mirror layer and green is the nitride layer.

Figure A.3: **The second Liger mask design.** This mask set surrounds the inner resonator with an outer resonator with various designs. The device diagonal is 2 mm. Black is the mirror layer, green is the nitride layer and magenta is the back nitride layer.

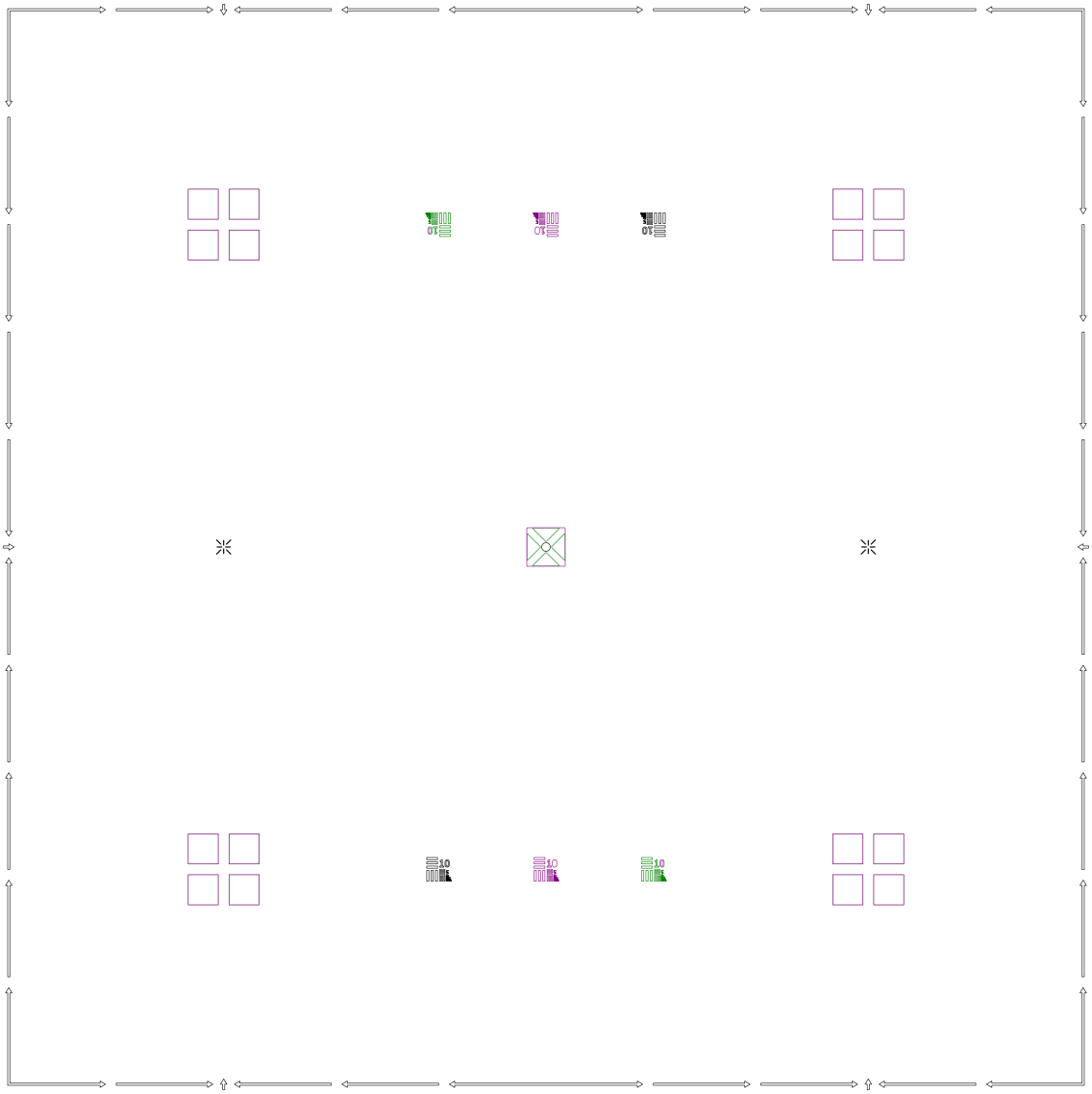

Figure A.4: **The Wolphin mask design.** This mask set tests out a single resonator on a chip. The device diagonal is 500 μm. Black is the mirror layer, green is the nitride layer and magenta is the back nitride layer. We include alignment markers in this mask to give a sense of what they look like in all of the designs.

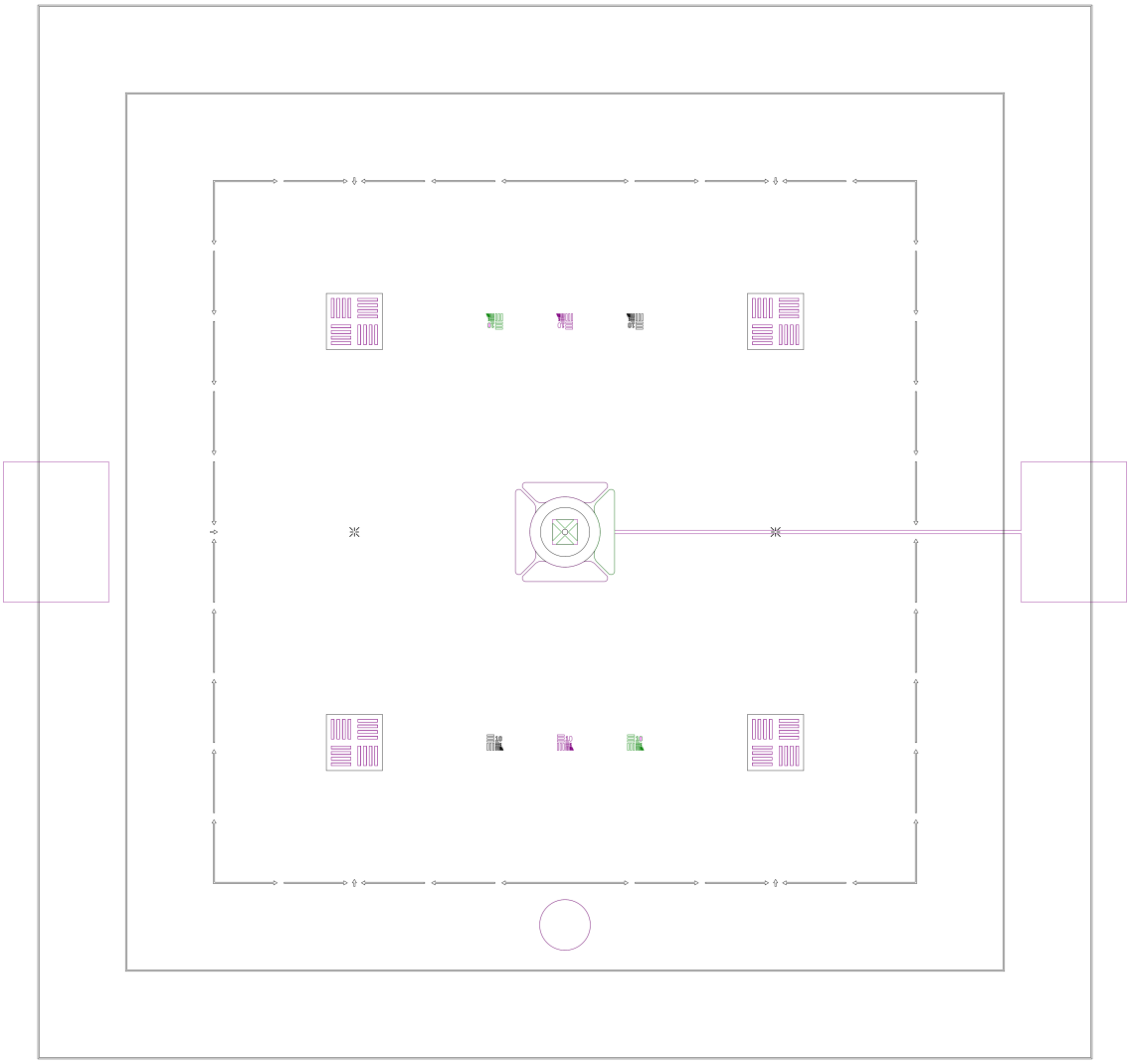

Figure A.5: **The Zorse front chip mask design.** This mask set tests a single nested resonator on a chip. The device diagonal is 2 mm. Black is the mirror layer, green is the nitride layer and magenta is the back nitride layer. In order to provide electrical control, the back side of the chip is coated with Al everywhere outside the purple.

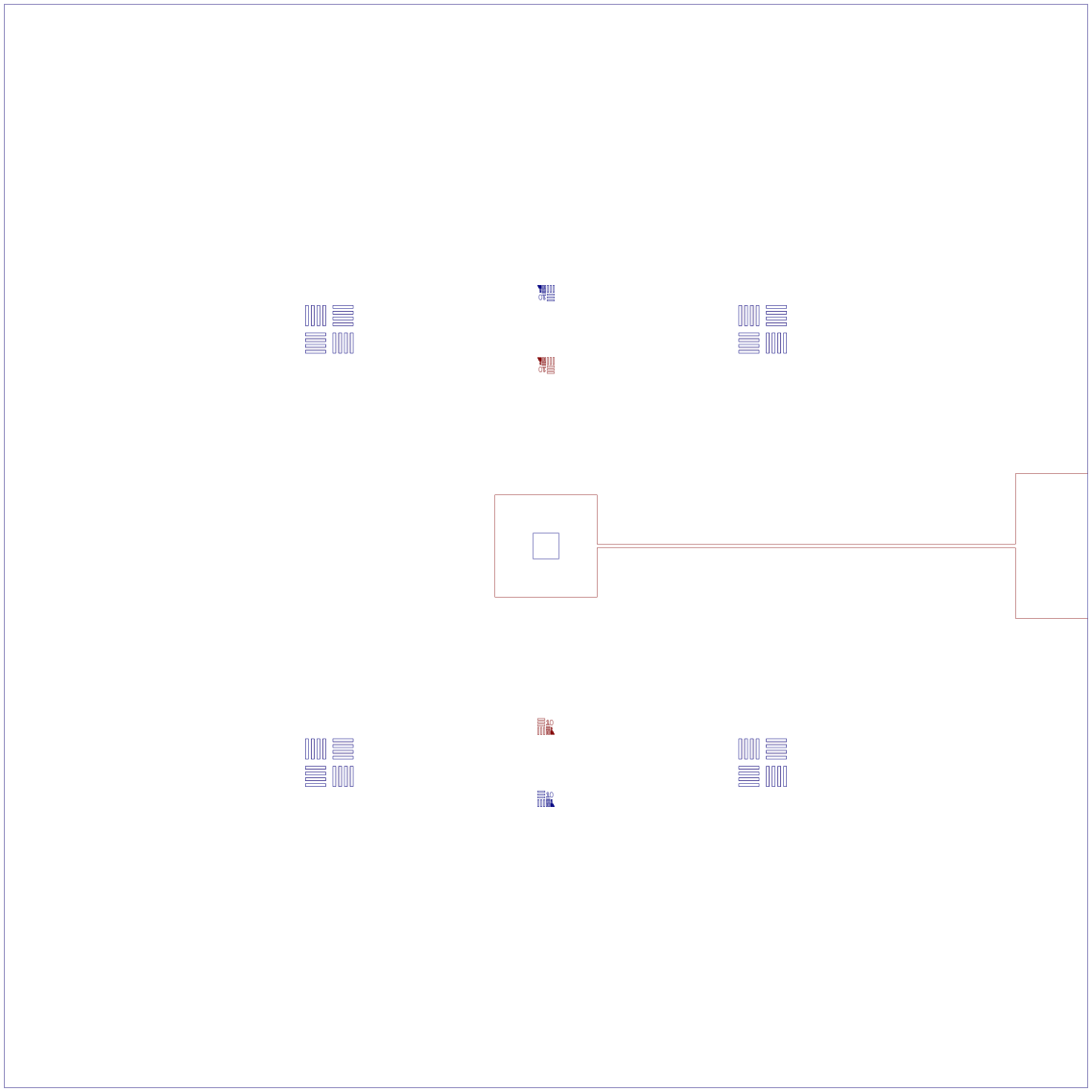

Figure A.6: **The Zorse back chip mask design.** This mask set is for a recessed capacitor pad. Red is the recessed Al layer, and blue is a hole through the chip for optical access from the back. Ideally the red region should be aligned with the purple region on the other chip to avoid excess stray capacitance. Note that the actual mask is flipped.

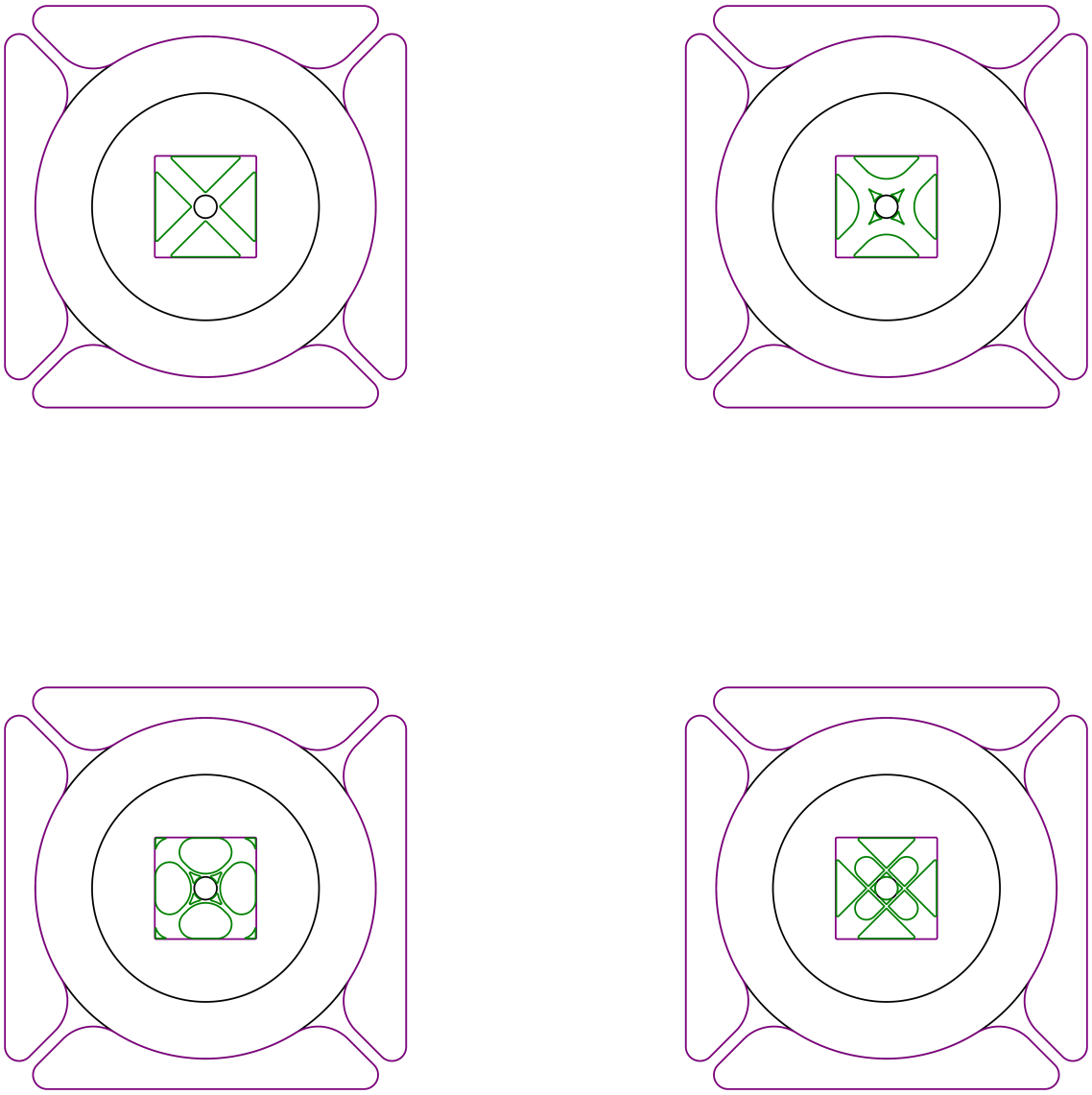

Figure A.7: **The Jackalope mask design.** This mask set tests clamping geometries in the inner resonator. The device diagonal is 2 mm. Black is the mirror layer, green is the nitride layer and magenta is the back nitride layer.

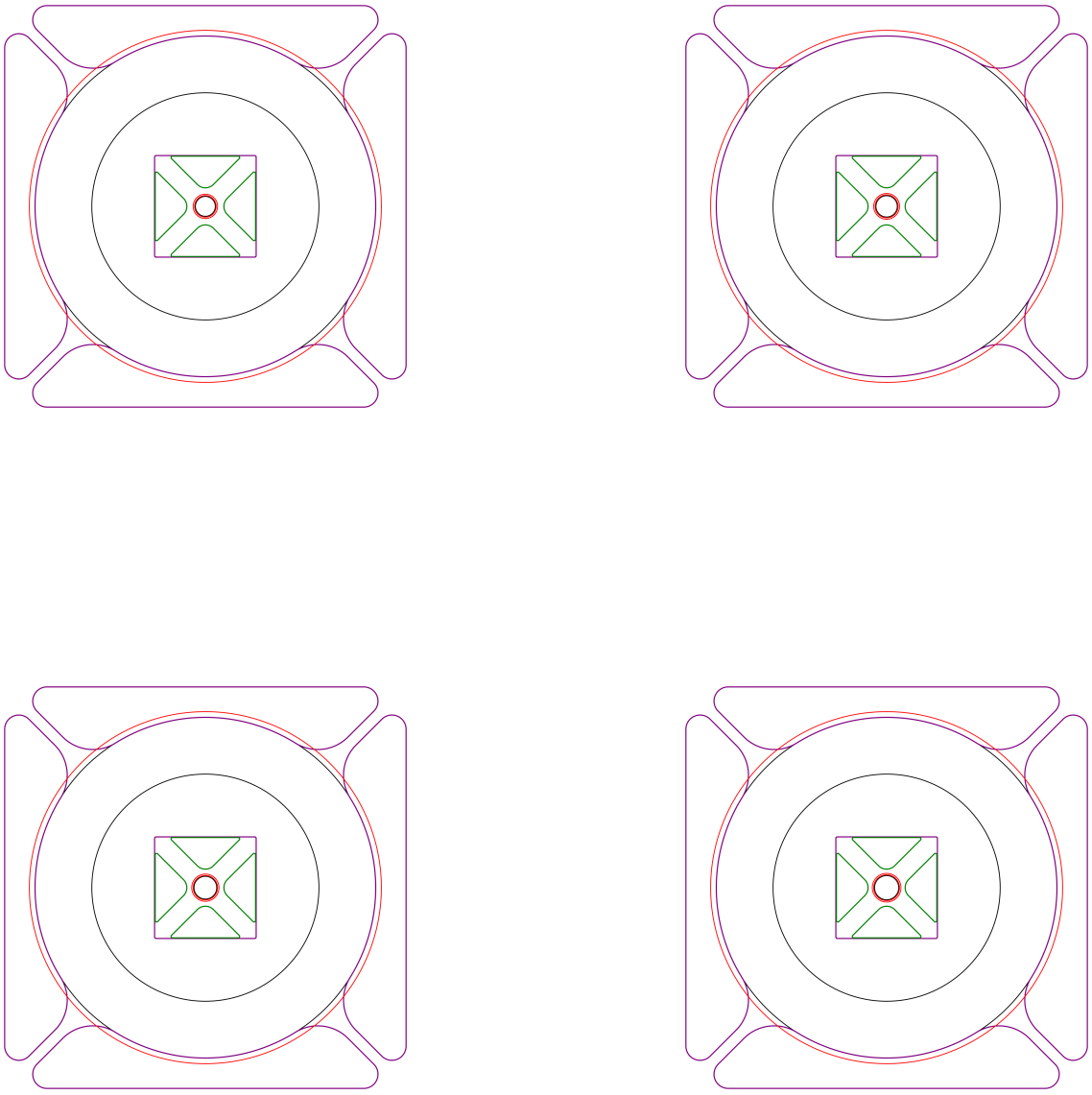

Figure A.8: **The Grolar Bear undercut mask design.** This mask set is used to make a series of trampoline resonators with DBR mirrors mounted on pedestals. The device diagonal is 2 mm. Black is the mirror layer, green is the nitride layer, red is the Cr and resist mirror protection layer and magenta is the back nitride layer. Note that the undercut etch starts from a narrow circle around the mirror.

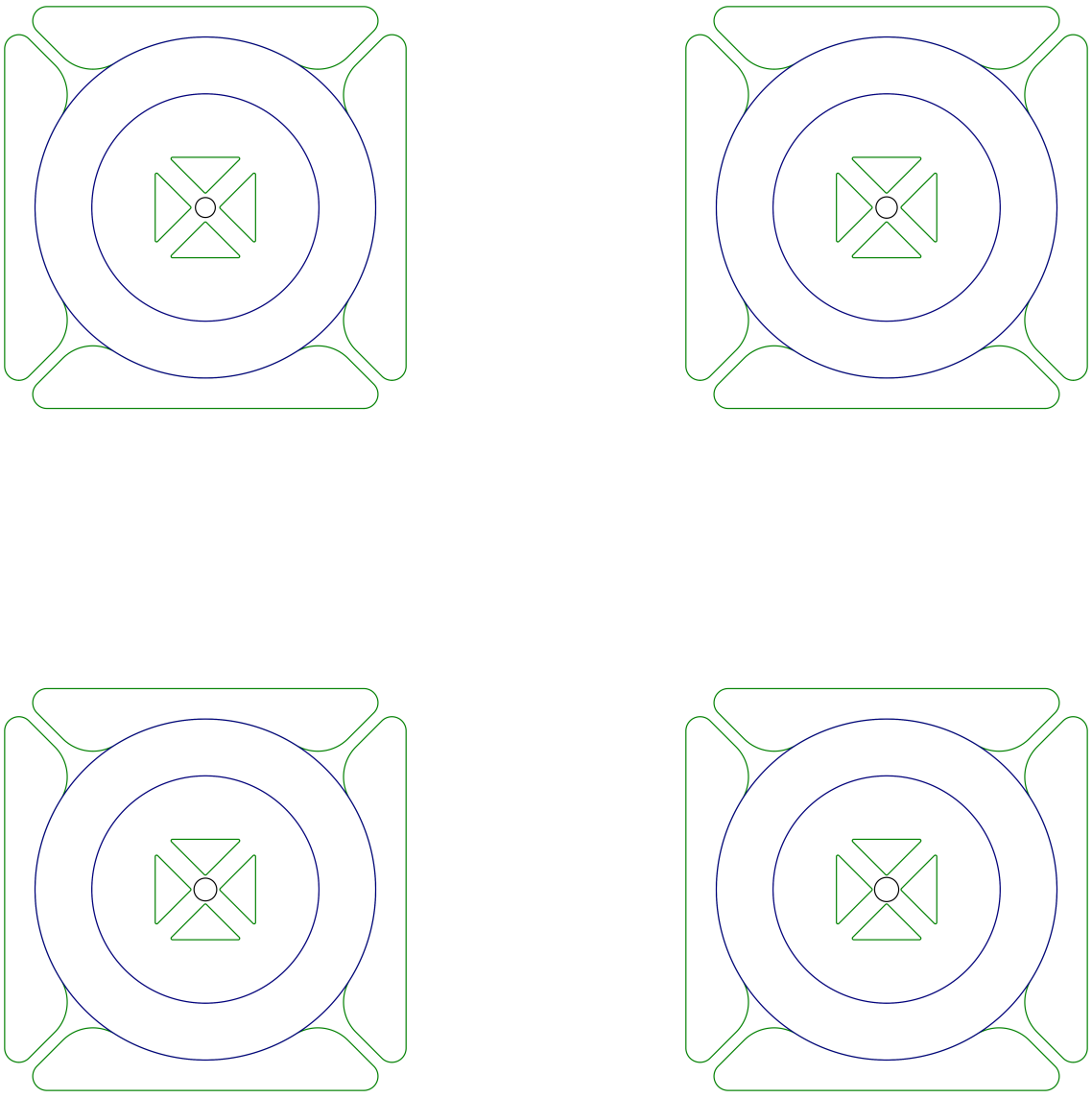

Figure A.9: **The double sided Grolar Bear mask design.** This mask set is used to make double sided trampoline resonators with bare trampolines on one side and DBR mirrors on the other. The device diagonal is 2 mm. Black is the mirror layer, green is the nitride layer on both sides, and blue is the nitride protection ring on the back. Note that the same design is used for the trampolines on both sides of the devices.

Bibliography

[1] E. Schrödinger, Die gegenwärtige Situation in der Quantenmechanik, *Die Naturwissenschaften* **23** 844 (1935).

[2] A. Aspect, P. Grangier and G. Roger, Experimental Realization of Einstein-Podolsky-Rosen-Bohm Gedankenexperiment : A New Violation of Bell's Inequalities, *Physical Review Letters* **49** 91 (1982).

[3] Z. Y. Ou and L. Mandel, Violation of Bell's Inequality and Classical Probability in a Two-Photon Correlation Experiment, *Physical Review Letters* **61** 50 (1988).

[4] M. H. Anderson, J. R. Ensher, M. R. Matthews, C. E. Wieman and E. A. Cornell, Observation of Bose-Einstein Condensation in a Dilute Atomic Vapor, *Science* **269** 198 (1995).

[5] M. R. Andrews, M.-O. Mewes, N. J. van Druten, D. S. Durfee, D. M. Kurn and W. Ketterle, Direct, Nondestructive Observation of a Bose Condensate, *Science* **273** 84 (1996).

[6] M. Arndt, O. Nairz, J. Vos-Andreae, C. Keller, G. Van Der Zouw and A. Zeilinger, Wave-particle duality of C60 molecules, *Nature* **401** 680 (1999).

[7] A. D. O'Connell, M. Hofheinz, M. Ansmann, R. C. Bialczak, M. Lenander, E. Lucero et al., Quantum ground state and single-phonon control of a mechanical resonator, *Nature* **464** 697 (2010).

[8] M. Aspelmeyer, T. J. Kippenberg and F. Marquardt, Cavity optomechanics, *Reviews of Modern Physics* **86** 1391 (2014) [1303.0733].

[9] W. H. Zurek, Decoherence, einselection, and the quantum origins of the classical, *Reviews of Modern Physics* **75** 715 (2003).

[10] A. O. Caldeira and A. J. Leggett, Path integral approach to quantum Brownian motion, *Physica A: Statistical Mechanics and its Applications* **121** 587 (1983).

[11] I. Pikovski, *On Quantum Superpositions in an Optomechanical System*, masters thesis, Freie Universitait Berlin, 2008.

[12] M. Schlosshauer, A. P. Hines and G. J. Milburn, Decoherence and dissipation of a quantum harmonic oscillator coupled to two-level systems, *Physical Review A* **77** 022111 (2008) [0712.2608].

[13] L. G. Remus, M. P. Blencowe and Y. Tanaka, Damping and decoherence of a nanomechanical resonator due to a few two-level systems, *Physical Review B - Condensed Matter and Materials Physics* **80** 174103 (2009) [0907.0431].

[14] L. G. Remus and M. P. Blencowe, Damping and decoherence of Fock states in a nanomechanical resonator due to two-level systems, *Physical Review B* **86** 205419 (2012) [1206.2200].

[15] E. Joos and H. D. Zeh, The emergence of classical properties through interaction with the environment, *Zeitschrift für Physik B Condensed Matter* **59** 223 (1985).

[16] M. R. Gallis and G. N. Fleming, Environmental and spontaneous localization, *Physical Review A* **42** 38 (1990).

[17] K. Hornberger and J. E. Sipe, Collisional decoherence reexamined, *Physical Review A - Atomic, Molecular, and Optical Physics* **68** 16 (2003).

[18] K. Hornberger, S. Uttenthaler, B. Brezger, L. Hackermüller, M. Arndt and A. Zeilinger, Collisional Decoherence Observed in Matter Wave Interferometry, *Physical Review Letters* **90** 4 (2003).

[19] L. Diosi, Models for universal reduction of macroscopic quantum fluctuations, *Physical Review A* **40** 1165 (1989).

[20] R. Penrose, On Gravity's role in Quantum State Reduction, *General Relativity and Gravitation* **28** 581 (1996).

[21] B. Pepper, E. Jeffrey, R. Ghobadi, C. Simon and D. Bouwmeester, Macroscopic superpositions via nested interferometry: Finite temperature and decoherence considerations, *New Journal of Physics* **14** 115025 (2012) [1207.1946].

[22] A. Bassi, K. Lochan, S. Satin, T. P. Singh and H. Ulbricht, Models of wave-function collapse, underlying theories, and experimental tests, *Reviews of Modern Physics* **85** 471 (2013) [1204.4325].

[23] P. Pearle, Combining stochastic dynamical state-vector reduction with spontaneous localization, *Physical Review A* **39** 2277 (1989).

[24] G. C. Ghirardi, P. Pearle and A. Rimini, Markov processes in Hilbert space and continuous spontaneous localization of systems of identical particles, *Physical Review A* **42** 78 (1990).

[25] G. C. Ghirardi, A. Rimini and T. Weber, Unified dynamics for microscopic and macroscopic systems, *Physical Review D* **34** 470 (1986).

[26] A. Bassi and G. Ghirardi, Dynamical Reduction Models, *Physics Reports* **379** 257 (2003).

[27] A. Bassi, Collapse models: analysis of the free particle dynamics, *Journal of Physics A: Mathematical and General* **38** 3173 (2004).

[28] J. Ellis, J. S. Hagelin, D. Nanopoulos and M. Srednicki, Search for violations of quantum mechanics, *Nuclear Physics B* **241** 381 (1984).

[29] J. Ellis, S. Mohanty and D. V. Nanopoulos, Quantum gravity and the collapse of the wavefunction, *Physics Letters B* **221** 113 (1989).

[30] J. Ellis, N. E. Mavromatos and D. V. Nanopoulos, String theory modifies quantum mechanics, *Physics Letters B* **293** 37 (1992).

[31] O. Romero-Isart, Quantum superposition of massive objects and collapse models, *Physical Review A - Atomic, Molecular, and Optical Physics* **84** 052121 (2011) [1110.4495].

[32] P. Meystre, A short walk through quantum optomechanics, *Annalen der Physik* **525** 215 (2013) [1210.3619].

[33] J. D. Teufel, T. Donner, D. Li, J. W. Harlow, M. S. Allman, K. Cicak et al., Sideband cooling of micromechanical motion to the quantum ground state, *Nature* **475** 359 (2011) [1103.2144].

[34] J. Chan, T. P. Alegre, A. H. Safavi-Naeini, J. T. Hill, A. Krause, S. Gröblacher et al., Laser cooling of a nanomechanical oscillator into its quantum ground state, *Nature* **478** 89 (2011) [1106.3614].

[35] M. Underwood, D. Mason, D. Lee, H. Xu, L. Jiang, A. B. Shkarin et al., Measurement of the motional sidebands of a nanogram-scale oscillator in the quantum regime, *Physical Review A - Atomic, Molecular, and Optical Physics* **92** 061801 (2015) [1406.7254].

[36] R. W. Peterson, T. P. Purdy, N. S. Kampel, R. W. Andrews, P. L. Yu, K. W. Lehnert et al., Laser Cooling of a Micromechanical Membrane to the Quantum Backaction Limit, *Physical Review Letters* **116** 063601 (2016) [1510.03911].

[37] Y. Chu, P. Kharel, W. H. Renninger, L. D. Burkhart, L. Frunzio, P. T. Rakich et al., Quantum acoustics with superconducting qubits, *Science* **358** 199 (2017) [1703.00342].

[38] R. Riedinger, S. Hong, R. A. Norte, J. A. Slater, J. Shang, A. G. Krause et al., Non-classical correlations between single photons and phonons from a mechanical oscillator, *Nature* **530** (2015) [1512.05360].

[39] S. Hong, R. Riedinger, I. Marinković, A. Wallucks, S. G. Hofer, R. A. Norte et al., Hanbury Brown and Twiss interferometry of single phonons from an optomechanical resonator, *Science* **358** 203 (2017) [1706.03777].

[40] S. Mancini, V. I. Man'ko and P. Tombesi, Ponderomotive control of quantum macroscopic coherence, *Physical Review A - Atomic, Molecular, and Optical Physics* **55** 3042 (1997).

[41] F. Marquardt, J. P. Chen, A. A. Clerk and S. M. Girvin, Quantum theory of cavity-assisted sideband cooling of mechanical motion, *Physical Review Letters* **99** 093902 (2007).

[42] I. Wilson-Rae, N. Nooshi, W. Zwerger and T. J. Kippenberg, Theory of ground state cooling of a mechanical oscillator using dynamical back-action, *Physical Review Letters* **99** 093901 (2007).

[43] S. Weis, R. Rivière, S. Deléglise, E. Gavartin, O. Arcizet, A. Schliesser et al., Optomechanically induced transparency, *Science* **330** 1520 (2010) [1007.0565].

[44] A. H. Safavi-Naeini, T. P. M. Alegre, J. Chan, M. Eichenfield, M. Winger, Q. Lin et al., Electromagnetically induced transparency and slow light with optomechanics, *Nature* **472** 69 (2011) [1012.1934].

[45] J. D. Teufel, D. Li, M. S. Allman, K. Cicak, A. J. Sirois, J. D. Whittaker et al., Circuit cavity electromechanics in the strong coupling regime, *Nature* **471** 204 (2010) [1011.3067].

[46] V. Fiore, Y. Yang, M. C. Kuzyk, R. Barbour, L. Tian and H. Wang, Storing optical information as a mechanical excitation in a silica optomechanical resonator, *Physical Review Letters* **107** 133601 (2011) [1106.4512].

[47] T. A. Palomaki, J. W. Harlow, J. D. Teufel, R. W. Simmonds and K. W. Lehnert, State Transfer Between a Mechanical Oscillator and Microwave Fields in the Quantum Regime, *Nature* **495** 210 (2012) [1206.5562].

[48] B. Pepper, *Bathed, Strained, Attenuated, Annihilated: Towards Quantum Optomechanics*, Ph.D. thesis, University of California, Santa Barbara, 2014.

[49] F. Buters, *Where photons meet phonons*, Ph.D. thesis, Universiteit Leiden, 2017.

[50] H. J. Eerkens, *Investigations of Radiation Pressure*, phd thesis, Universiteit Leiden, 2017.

[51] W. Marshall, C. Simon, R. Penrose and D. Bouwmeester, Towards quantum superpositions of a mirror, *Physical Review Letters* **91** 130401 (2003).

[52] R. Leijssen, G. R. La Gala, L. Freisem, J. T. Muhonen and E. Verhagen, Nonlinear cavity optomechanics with nanomechanical thermal fluctuations, *Nature Communications* **8** 16024 (2017) [1612.08072].

[53] B. Pepper, R. Ghobadi, E. Jeffrey, C. Simon and D. Bouwmeester, Optomechanical superpositions via nested interferometry, *Physical Review Letters* **109** 023601 (2011) [1111.5672].

[54] P. Sekatski, M. Aspelmeyer and N. Sangouard, Macroscopic Optomechanics from Displaced Single-Photon Entanglement, *Physical Review Letters* **112** 080502 (2014) [1401.2357].

[55] R. Ghobadi, S. Kumar, B. Pepper, D. Bouwmeester, A. I. Lvovsky and C. Simon, Optomechanical Micro-Macro Entanglement, *Physical Review Letters* **112** 080503 (2014) [1401.2356].

[56] D. Kleckner, I. Pikovski, E. Jeffrey, L. Ament, E. Eliel, J. Van Den Brink et al., Creating and verifying a quantum superposition in a micro-optomechanical system, *New Journal of Physics* **10** 095020 (2008) [0807.1834].

[57] A. Dorsel, J. D. McCullen, P. Meystre, E. Vignes and H. Walther, Optical bistability and mirror confinement induced by radiation pressure, *Physical Review Letters* **51** 1550 (1983).

[58] P. Meystre, J. D. McCullen, E. Vignes and E. M. Wright, Theory of radiation-pressure-driven interferometers, *Journal of the Optical Society of America B* **2** 1830 (1985).

[59] K. Jacobs, P. Tombesi, M. J. Collett and D. F. Walls, Quantum-nondemolition measurement of photon number using radiation pressure, *Physical Review A* **49** 1961 (1994).

[60] The LIGO Scientific Collaboration and The Virgo Collaboration, GW150914: The Advanced LIGO Detectors in the Era of First Discoveries, *Physical Review Letters* **116** 131103 (2016) [1602.03838].

[61] D. Kleckner, W. Marshall, M. J. De Dood, K. N. Dinyari, B. J. Pors, W. T. Irvine et al., High finesse opto-mechanical cavity with a movable thirty-micron-size mirror, *Physical Review Letters* **96** 173901 (2006).

[62] E. Serra, A. Borrielli, F. S. Cataliotti, F. Marin, F. Marino, A. Pontin et al., A low-deformation mirror micro-oscillator with ultra-low optical and mechanical losses, *Applied Physics Letters* **101** 071101 (2012).

[63] A. Kuhn, L. Neuhaus, E. Van Brackel, C. Chartier, O. Ducloux, O. Le Traon et al., A micropillar for cavity optomechanics, *AIP Conference Proceedings* **1633** 68 (2014) [1107.3828].

[64] S. Gröblacher, J. B. Hertzberg, M. R. Vanner, G. D. Cole, S. Gigan, K. C. Schwab et al., Demonstration of an ultracold micro-optomechanical oscillator in a cryogenic cavity, *Nature Physics* **5** 485 (2009) [0901.1801].

[65] D. Kleckner, B. Pepper, E. Jeffrey, P. Sonin, S. M. Thon and D. Bouwmeester, Optomechanical trampoline resonators., *Opt. Expr.* **19** 19708 (2011).

[66] J. D. Thompson, B. M. Zwickl, A. M. Jayich, F. Marquardt, S. M. Girvin and J. G. E. Harris, Strong dispersive coupling of a high finesse cavity to a micromechanical membrane, *Nature* **452** 72 (2007) [0707.1724].

[67] D. J. Wilson, C. A. Regal, S. B. Papp and H. J. Kimble, Cavity optomechanics with stoichiometric SiN films, *Physical Review Letters* **103** 207204 (2009) [0909.0970].

[68] J. C. Sankey, C. Yang, B. M. Zwickl, A. M. Jayich and J. G. Harris, Strong and tunable nonlinear optomechanical coupling in a low-loss system, *Nature Physics* **6** 707 (2010) [1002.4158].

[69] P. L. Yu, T. P. Purdy and C. A. Regal, Control of material damping in High-Q membrane microresonators, *Physical Review Letters* **108** 083603 (2012) [1111.1703].

[70] D. J. Wilson, *Cavity Optomechanics with High-Stress Silicon Nitride Films*, phd thesis, Caltech, 2012.

[71] E. Vlieg, *A membrane-in-the-middle device for optomechanics*, masters thesis, Leiden University, 2017.

[72] A. M. Jayich, J. C. Sankey, B. M. Zwickl, C. Yang, J. D. Thompson, S. M. Girvin et al., Dispersive optomechanics: A membrane inside a cavity, *New Journal of Physics* **10** 095008 (2008) [0805.3723].

[73] A. Noguchi, R. Yamazaki, M. Ataka, H. Fujita, Y. Tabuchi, T. Ishikawa et al., Ground state cooling of a quantum electromechanical system with a silicon nitride membrane in a 3D loop-gap cavity, *New Journal of Physics* **18** 103036 (2016).

[74] F. Beauville, D. Buskulic, R. Flaminio, F. Marion, F. Ricci, A. Masserot et al., Low-loss coatings for the VIRGO large mirrors, *Advances in Optical Thin Films* **5250** 483 (2004).

[75] G. M. Harry, M. R. Abernathy, A. E. Becerra-Toledo, H. Armandula, E. Black, K. Dooley et al., Titania-doped tantala/silica coatings for gravitational-wave detection, *Classical and Quantum Gravity* **24** 405 (2007).

[76] R. Flaminio, J. Franc, C. Michel, N. Morgado, L. Pinard and B. Sassolas, A study of coating mechanical and optical losses in view of reducing mirror thermal noise in gravitational wave detectors, *Classical and Quantum Gravity* **27** 084030 (2010).

[77] D. Kleckner, W. T. Irvine, S. S. Oemrawsingh and D. Bouwmeester, Diffraction-limited high-finesse optical cavities, *Physical Review A - Atomic, Molecular, and Optical Physics* **81** 043814 (2010).

[78] C. Dong, V. Fiore, M. C. Kuzyk and H. Wang, Optomechanical dark mode, *Science* **338** 1609 (2012).

[79] A. Metelmann and A. A. Clerk, Nonreciprocal photon transmission and amplification via reservoir engineering, *Physical Review X* **5** 021025 (2015) [1502.07274].

[80] F. M. Buters, M. J. Weaver, H. J. Eerkens, K. Heeck, S. De Man and D. Bouwmeester, Optomechanics with a polarization nondegenerate cavity, *Physical Review A* **94** 063813 (2016) [1606.06869].

[81] D. Hunger, T. Steinmetz, Y. Colombe, C. Deutsch, T. W. Hänsch and J. Reichel, A fiber Fabry-Perot cavity with high finesse, *New Journal of Physics* **12** 065038 (2010) [1005.0067].

[82] A. Muller, E. B. Flagg, J. R. Lawall and G. S. Solomon, Ultrahigh-finesse, low-mode-volume Fabry-Perot microcavity, *Optics Letters* **35** 2293 (2010).

[83] D. J. Wilson, V. Sudhir, N. Piro, R. Schilling, A. Ghadimi and T. J. Kippenberg, Measurement-based control of a mechanical oscillator at its thermal decoherence rate, *Nature* **524** 325 (2015) [1410.6191].

[84] M. Uphoff, M. Brekenfeld, G. Rempe and S. Ritter, Frequency splitting of polarization eigenmodes in microscopic Fabry-Perot cavities, *New Journal of Physics* **17** 013053 (2015) [1408.4367].

[85] M. R. Vanner, M. Aspelmeyer and M. S. Kim, Quantum State Orthogonalization and a Toolset for Quantum Optomechanical Phonon Control, *Physical Review Letters* **110** 010504 (2013) [1203.4525].

[86] C. Galland, N. Sangouard, N. Piro, N. Gisin and T. J. Kippenberg, Heralded single-phonon preparation, storage, and readout in cavity optomechanics, *Physical Review Letters* **112** 143602 (2014) [1312.4303].

[87] H. J. Eerkens, F. M. Buters, M. J. Weaver, B. Pepper, G. Welker, K. Heeck et al., Optical side-band cooling of a low frequency optomechanical system, *Optics Express* **23** 8014 (2015).

[88] F. M. Buters, H. J. Eerkens, K. Heeck, M. J. Weaver, B. Pepper, S. De Man et al., Experimental exploration of the optomechanical attractor diagram and its dynamics, *Physical Review A - Atomic, Molecular, and Optical Physics* **92** 013811 (2015) [1504.06119].

[89] M. J. Weaver, B. Pepper, F. Luna, F. M. Buters, H. J. Eerkens, G. Welker et al., Nested Trampoline Resonators for Optomechanics, *Appl. Phys. Lett* **108** 033501 (2015) [1510.00206].

[90] G. D. Cole, I. Wilson-Rae, K. Werbach, M. R. Vanner and M. Aspelmeyer, Minimization of phonon-tunneling dissipation in mechanical resonators, *Nature Communications* **2** 231 (2010) [1007.4948].

[91] I. Wilson-Rae, R. A. Barton, S. S. Verbridge, D. R. Southworth, B. Ilic, H. G. Craighead et al., High-Q nanomechanics via destructive interference of elastic waves, *Physical Review Letters* **106** 047205 (2011) [1010.2171].

[92] T. P. M. Alegre, A. Safavi-Naeini, M. Winger and O. Painter, Quasi-two-dimensional optomechanical crystals with a complete phononic bandgap, *Optics Express* **19** 5658 (2010) [1012.2556].

[93] P. L. Yu, K. Cicak, N. S. Kampel, Y. Tsaturyan, T. P. Purdy, R. W. Simmonds et al., A phononic bandgap shield for high-Q membrane microresonators, *Applied Physics Letters* **104** 023510 (2014) [1312.0962].

[94] R. Norte, *Nanofabrication for On-Chip Optical Levitation, Atom-Trapping, and Superconducting Quantum Circuits*, Ph.D. thesis, California Institute of Technology, 2014.

[95] J. Liu, F. A. Torres, Y. Ma, C. Zhao, L. Ju, D. G. Blair et al., Near-self-imaging cavity for three-mode optoacoustic parametric amplifiers using silicon microresonators, *Applied Optics* **53** 841 (2014).

[96] J. A. Haringx, No Title, *Philips Tech. Tijdschr.* **1** 16 (1947).

[97] G. M. Harry, Advanced LIGO: The next generation of gravitational wave detectors, *Classical and Quantum Gravity* **27** 084006 (2010).

[98] A. Borrielli, A. Pontin, F. S. Cataliotti, L. Marconi, F. Marin, F. Marino et al., Low-Loss Optomechanical Oscillator for Quantum-Optics Experiments, *Physical Review Applied* **3** 054009 (2015).

[99] S. Thornton and J. Marion, Chapter 3, in *Classical Dynamics of Particles and Systems*, ch. 3. Thomson Learning, 2004.

[100] Q. P. Unterreithmeier, T. Faust and J. P. Kotthaus, Damping of nanomechanical resonators, *Physical Review Letters* **105** 027205 (2010) [1003.1868].

[101] C. A. Zorman and M. Mehregany, Chapter 11, in *Springer Handbook of Nanothechnology*, ch. 11. Springer, 3 ed., 2010.

[102] I. Wilson-Rae, Intrinsic dissipation in nanomechanical resonators due to phonon tunneling, *Physical Review B - Condensed Matter and Materials Physics* **77** 245418 (2008) [0710.0200].

[103] A. A. Clerk, F. Marquardt and K. Jacobs, Back-action evasion and squeezing of a mechanical resonator using a cavity detector, *New Journal of Physics* **10** 095010 (2008) [0802.1842].

[104] B. M. Zwickl, W. E. Shanks, A. M. Jayich, C. Yang, A. C. Jayich, J. D. Thompson et al., High quality mechanical and optical properties of commercial silicon nitride membranes, *Applied Physics Letters* **92** 103125 (2008) [0711.2263].

[105] M. M. Leivo and J. P. Pekola, Thermal characteristics of silicon nitride membranes at sub-Kelvin temperatures, *Applied Physics Letters* **72** 1305 (1998).

[106] H. Ftouni, C. Blanc, D. Tainoff, A. D. Fefferman, M. Defoort, K. J. Lulla et al., Thermal conductivity of silicon nitride membranes is not sensitive to stress, *Physical Review B - Condensed Matter and Materials Physics* **92** 125439 (2015) [1506.01838].

[107] F. M. Buters, K. Heeck, H. J. Eerkens, M. J. Weaver, F. Luna, S. De Man et al., High-Q nested resonator in an actively stabilized optomechanical cavity, *Applied Physics Letters* **110** 104104 (2017) [1701.04212].

[108] F. M. Buters, F. Luna, M. J. Weaver, H. J. Eerkens, K. Heeck, S. de Man et al., Straightforward method to measure optomechanically induced transparency, *Optics Express* **25** 12935 (2017).

[109] S. S. Verbridge, J. M. Parpia, R. B. Reichenbach, L. M. Bellan and H. G. Craighead, High quality factor resonance at room temperature with nanostrings under high tensile stress, *Journal of Applied Physics* **99** 124304 (2006).

[110] S. Schmid, K. D. Jensen, K. H. Nielsen and A. Boisen, Damping mechanisms in high-Q micro and nanomechanical string resonators, *Physical Review B - Condensed Matter and Materials Physics* **84** 165307 (2011).

[111] R. A. Norte, J. P. Moura and S. Gröblacher, Mechanical Resonators for Quantum Optomechanics Experiments at Room Temperature, *Physical Review Letters* **116** 147202 (2016) [1511.06235].

[112] C. Reinhardt, T. Müller, A. Bourassa and J. C. Sankey, Ultralow-noise SiN trampoline resonators for sensing and optomechanics, *Physical Review X* **6** 021001 (2016) [1511.01769].

[113] Y. Tsaturyan, A. Barg, E. S. Polzik and A. Schliesser, Ultracoherent nanomechanical resonators via soft clamping and dissipation dilution, *Nature Nanotechnology* **12** 776 (2017) [1608.00937].

[114] T. Faust, J. Rieger, M. J. Seitner, J. P. Kotthaus and E. M. Weig, Signatures of two-level defects in the temperature-dependent damping of nanomechanical silicon nitride resonators, *Physical Review B - Condensed Matter and Materials Physics* **89** 100102 (2014) [1310.3671].

[115] J. Suh, A. J. Weinstein and K. C. Schwab, Optomechanical effects of two-level systems in a back-action evading measurement of micro-mechanical motion, *Applied Physics Letters* **103** 052604 (2013).

[116] D. Tielbürger, R. Merz, R. Ehrenfels and S. Hunklinger, Thermally activated relaxation processes in vitreous silica: An investigation by Brillouin scattering at high pressures, *Physical Review B* **45** 2750 (1992).

[117] R. Vacher, E. Courtens and M. Foret, Anharmonic versus relaxational sound damping in glasses. II. Vitreous silica, *Physical Review B - Condensed Matter and Materials Physics* **72** 214205 (2005).

[118] K. Y. Fong, W. H. P. Pernice and H. X. Tang, Frequency and phase noise of ultra-high Q silicon nitride nanomechanical resonators, *Physical Review B - Condensed Matter and Materials Physics* **85** 161410 (2012) [1204.1942].

[119] T. P. Purdy, R. W. Peterson, P. L. Yu and C. A. Regal, Cavity optomechanics with Si3N4 membranes at cryogenic temperatures, *New Journal of Physics* **14** 115021 (2012) [1208.6560].

[120] M. Yuan, M. A. Cohen and G. A. Steele, Silicon nitride membrane resonators at millikelvin temperatures with quality factors exceeding 108, *Applied Physics Letters* **107** 263501 (2015) [1510.07468].

[121] R. Fischer, N. S. Kampel, G. G. T. Assumpção, P. L. Yu, K. Cicak, R. W. Peterson et al., Optical probing of mechanical loss of a Si3N4 membrane below 100 mK, 1611.00878.

[122] K. Yamamoto, S. Miyoki, T. Uchiyama, H. Ishitsuka, M. Ohashi, K. Kuroda et al., Measurement of the mechanical loss of a cooled reflective coating for gravitational wave detection, *Physical Review D - Particles, Fields, Gravitation and Cosmology* **74** 022002 (2006).

[123] I. W. Martin, E. Chalkley, R. Nawrodt, H. Armandula, R. Bassiri, C. Comtet et al., Comparison of the temperature dependence of the mechanical dissipation in thin films of Ta2O5 and Ta2O5 doped with TiO2, *Classical and Quantum Gravity* **26** 155012 (2009).

[124] A. E. Villar, E. D. Black, R. DeSalvo, K. G. Libbrecht, C. Michel, N. Morgado et al., Measurement of Thermal Noise in Multilayer Coatings with Optimized Layer Thickness, *Physical Review D* **81** 122001 (2010) [1004.1223].

[125] M. Granata, K. Craig, G. Cagnoli, C. Carcy, W. Cunningham, J. Degallaix et al., Cryogenic measurements of mechanical loss of high-reflectivity coating and estimation of thermal noise., *Optics letters* **38** 5268 (2013).

[126] T. Li, F. A. Aguilar Sandoval, M. Geitner, L. Bellon, G. Cagnoli, J. Degallaix et al., Measurements of mechanical thermal noise and energy dissipation in optical dielectric coatings, *Physical Review D - Particles, Fields, Gravitation and Cosmology* **89** 092004 (2014) [1401.0184].

[127] L. G. Villanueva and S. Schmid, Evidence of surface loss as ubiquitous limiting damping mechanism in SiN micro- and nanomechanical resonators, *Physical Review Letters* **113** 227201 (2014) [1405.6115].

[128] G. D. Cole, W. Zhang, M. J. Martin, J. Ye and M. Aspelmeyer, Tenfold reduction of Brownian noise in high-reflectivity optical coatings, *Nature Photonics* **7** 644 (2013) [1302.6489].

[129] M. J. Weaver, F. Buters, F. Luna, H. Eerkens, K. Heeck, S. de Man et al., Coherent optomechanical state transfer between disparate mechanical resonators, *Nature Communications* **8** 824 (2017) [1704.02394].

[130] Q. Lin, J. Rosenberg, D. Chang, R. Camacho, M. Eichenfield, K. J. Vahala et al., Coherent mixing of mechanical excitations in nano-optomechanical structures, *Nature Photonics* **4** 236 (2010) [0908.1128].

[131] R. W. Andrews, R. W. Peterson, T. P. Purdy, K. Cicak, R. W. Simmonds, C. A. Regal et al., Bidirectional and efficient conversion between microwave and optical light, *Nature Physics* **10** 321 (2014) [1310.5276].

[132] M. J. Woolley and A. A. Clerk, Two-mode squeezed states in cavity optomechanics via engineering of a single reservoir, *Physical Review A - Atomic, Molecular, and Optical Physics* **89** 063805 (2014) [1404.2672].

[133] J. Li, I. M. Haghighi, N. Malossi, S. Zippilli and D. Vitali, Generation and detection of large and robust entanglement between two different mechanical resonators in cavity optomechanics, *New Journal of Physics* **17** 103037 (2015) [1506.03126].

[134] A. Pontin, M. Bonaldi, A. Borrielli, L. Marconi, F. Marino, G. Pandraud et al., Dynamical Two-Mode Squeezing of Thermal Fluctuations in a Cavity Optomechanical System, *Physical Review Letters* **116** 103601 (2016) [1509.02723].

[135] C. Dong, J. Zhang, V. Fiore and H. Wang, Optomechanically induced transparency and self-induced oscillations with Bogoliubov mechanical modes, *Optica* **1** 425 (2014).

[136] K. Fang, M. H. Matheny, X. Luan and O. Painter, Phonon routing in integrated optomechanical cavity-waveguide systems, *Nature Photonics* **10** 489 (2015) [1508.05138].

[137] J. B. Hertzberg, T. Rocheleau, T. Ndukum, M. Savva, A. A. Clerk and K. C. Schwab, Back-action-evading measurements of nanomechanical motion, *Nature Physics* **6** 213 (2010) [0906.0967].

[138] C. F. Ockeloen-Korppi, E. Damskägg, J. M. Pirkkalainen, A. A. Clerk, M. J. Woolley and M. A. Sillanpää, Quantum Backaction Evading Measurement of Collective Mechanical Modes, *Physical Review Letters* **117** 140401 (2016) [1608.06152].

[139] M. Frimmer, J. Gieseler and L. Novotny, Cooling Mechanical Oscillators by Coherent Control, *Physical Review Letters* **117** 163601 (2016) [1608.00998].

[140] X. Xu, T. Purdy and J. M. Taylor, Cooling a Harmonic Oscillator by Optomechanical Modification of Its Bath, *Physical Review Letters* **118** 223602 (2017) [1608.05717].

[141] L. D. Tóth, N. R. Bernier, A. Nunnenkamp, A. K. Feofanov and T. J. Kippenberg, A dissipative quantum reservoir for microwave light using a mechanical oscillator, *Nature Physics* **13** 787 (2017) [1602.05180].

[142] U. Gaubatz, P. Rudecki, S. Schiemann and K. Bergmann, Population transfer between molecular vibrational levels by stimulated Raman scattering with partially overlapping laser fields. A new concept and experimental results, *The Journal of Chemical Physics* **92** 5363 (1990).

[143] A. B. Shkarin, N. E. Flowers-Jacobs, S. W. Hoch, A. D. Kashkanova, C. Deutsch, J. Reichel et al., Optically mediated hybridization between two mechanical modes, *Physical Review Letters* **112** 013602 (2014) [1306.0613].

[144] N. Spethmann, J. Kohler, S. Schreppler, L. Buchmann and D. M. Stamper-Kurn, Cavity-mediated coupling of mechanical oscillators limited by quantum back-action, *Nature Physics* **12** 27 (2015) [1505.05850].

[145] T. Faust, J. Rieger, M. J. Seitner, J. P. Kotthaus and E. M. Weig, Coherent control of a nanomechanical two-level system, *Nature Physics* **9** 485 (2012) [1212.3172].

[146] H. Okamoto, A. Gourgout, C.-Y. Chang, K. Onomitsu, I. Mahboob, E. Y. Chang et al., Coherent phonon manipulation in coupled mechanical resonators, *Nature Physics* **9** 480 (2012) [1212.3097].

[147] M. Pernpeintner, P. Schmidt, D. Schwienbacher, R. Gross and H. Huebl, Frequency control and coherent excitation transfer in a nanostring resonator network, 1612.07511.

[148] L. F. Buchmann and D. M. Stamper-Kurn, Nondegenerate multimode optomechanics, *Physical Review A - Atomic, Molecular, and Optical Physics* **92** 013851 (2015) [1404.4855].

[149] E. Damskägg, J. M. Pirkkalainen and M. A. Sillanpää, Dynamically creating tripartite resonance and dark modes in a multimode optomechanical system, *Journal of Optics* **18** 104003 (2016) [1609.08809].

[150] J. Zhang, K. Peng and S. L. Braunstein, Quantum-state transfer from light to macroscopic oscillators, *Physical Review A - Atomic, Molecular, and Optical Physics* **68** 5 (2003).

[151] R. W. P. Drever, J. L. Hall, F. V. Kowalski, J. Hough, G. M. Ford, A. J. Munley et al., Laser phase and frequency stabilization using an optical resonator, *Applied Physics B* **31** 97 (1983).

[152] H. Xu, D. Mason, L. Jiang and J. G. E. Harris, Topological dynamics in an optomechanical system with highly non-degenerate modes, 1703.07374.

[153] M. J. Weaver, D. Newsom, F. Luna, W. Löffler and D. Bouwmeester, Phonon Interferometry for Measuring Quantum Decoherence, 1802.08399.

[154] M. Goryachev, D. L. Creedon, E. N. Ivanov, S. Galliou, R. Bourquin and M. E. Tobar, Extremely low-loss acoustic phonons in a quartz bulk acoustic wave resonator at millikelvin temperature, *Applied Physics Letters* **100** 243504 (2012) [1202.4556].

[155] F. Lecocq, J. D. Teufel, J. Aumentado and R. W. Simmonds, Resolving the vacuum fluctuations of an optomechanical system using an artificial atom, *Nature Physics* **11** 635 (2015) [1409.0872].

[156] D. Vitali, S. Mancini and P. Tombesi, Stationary entanglement between two movable mirrors in a classically driven Fabry-Perot cavity, *Journal of Physics A: Mathematical and Theoretical* **40** 8055 (2006).

[157] M. J. Hartmann and M. B. Plenio, Steady state entanglement in the mechanical vibrations of two dielectric membranes, *Physical Review Letters* **101** 200503 (2008) [0806.1616].

[158] K. Børkje, A. Nunnenkamp and S. M. Girvin, Proposal for Entangling Remote Micromechanical Oscillators via Optical Measurements, *Physical Review Letters* **107** 123601 (2011) [1103.2368].

[159] J. Li, G. Li, S. Zippilli, D. Vitali and T. Zhang, Enhanced entanglement of two different mechanical resonators via coherent feedback, *Physical Review A* **95** 043819 (2017) [1610.07261].

[160] J. Zhang, T. Zhang and J. Li, Probing spontaneous wave-function collapse with entangled levitating nanospheres, *Physical Review A* **95** 012141 (2017) [1611.09989].

[161] U. Akram, W. P. Bowen and G. J. Milburn, Entangled mechanical cat states via conditional single photon optomechanics, *New Journal of Physics* **15** 093007 (2013) [1305.3781].

[162] H. Flayac and V. Savona, Heralded Preparation and Readout of Entangled Phonons in a Photonic Crystal Cavity, *Physical Review Letters* **113** 143603 (2014) [1407.5275].

[163] R. Blatt and D. Wineland, Entangled states of trapped atomic ions, *Nature* **453** 1008 (2008).

[164] K. C. Lee, M. R. Sprague, B. J. Sussman, J. Nunn, N. K. Langford, X.-M. Jin et al., Entangling macroscopic diamonds at room temperature, *Science* **334** 1253 (2011).

[165] R. Riedinger, A. Wallucks, I. Marinkovic, C. Löschnauer, M. Aspelmeyer, S. Hong et al., Remote quantum entanglement between two micromechanical oscillators, *Nature* **556** 473 (2017) [1710.11147].

[166] A. Jöckel, A. Faber, T. Kampschulte, M. Korppi, M. T. Rakher and P. Treutlein, Sympathetic cooling of a membrane oscillator in a hybrid mechanical-atomic system, *Nature Nanotechnology* **10** 55 (2015) [1407.6820].

[167] H. Zhong, G. Fläschner, A. Schwarz, R. Wiesendanger, P. Christoph, T. Wagner et al., A millikelvin all-fiber cavity optomechanical apparatus for merging with ultra-cold atoms in a hybrid quantum system, *Review of Scientific Instruments* **88** 023115 (2017) [1611.03406].

[168] S. G. Hofer, W. Wieczorek, M. Aspelmeyer and K. Hammerer, Quantum entanglement and teleportation in pulsed cavity optomechanics, *Physical Review A - Atomic, Molecular, and Optical Physics* **84** 052327 (2011) [1108.2586].

[169] A. M. Jayich, J. C. Sankey, K. Borkje, D. Lee, C. Yang, M. Underwood et al., Cryogenic optomechanics with a Si3N4 membrane and classical laser noise, *New Journal of Physics* **14** 115018 (2012) [1209.2730].

[170] Y. Sflenda, *Cavity optomechanics in a millikelvin environment*, master's thesis, KU Leuven, 2017.

[171] A. H. Ghadimi, S. A. Fedorov, N. J. Engelsen, M. J. Bereyhi, R. Schilling, D. J. Wilson et al., Elastic strain engineering for ultralow mechanical dissipation, *Science* **360** 764 (2018).

[172] N. V. Vitanov, A. A. Rangelov, B. W. Shore and K. Bergmann, Stimulated Raman adiabatic passage in physics, chemistry, and beyond, *Reviews of Modern Physics* **89** 015006 (2017) [1605.00224].